Atmospheric Traces Monitoring
Using
Cavity Ringdown Spectroscopy

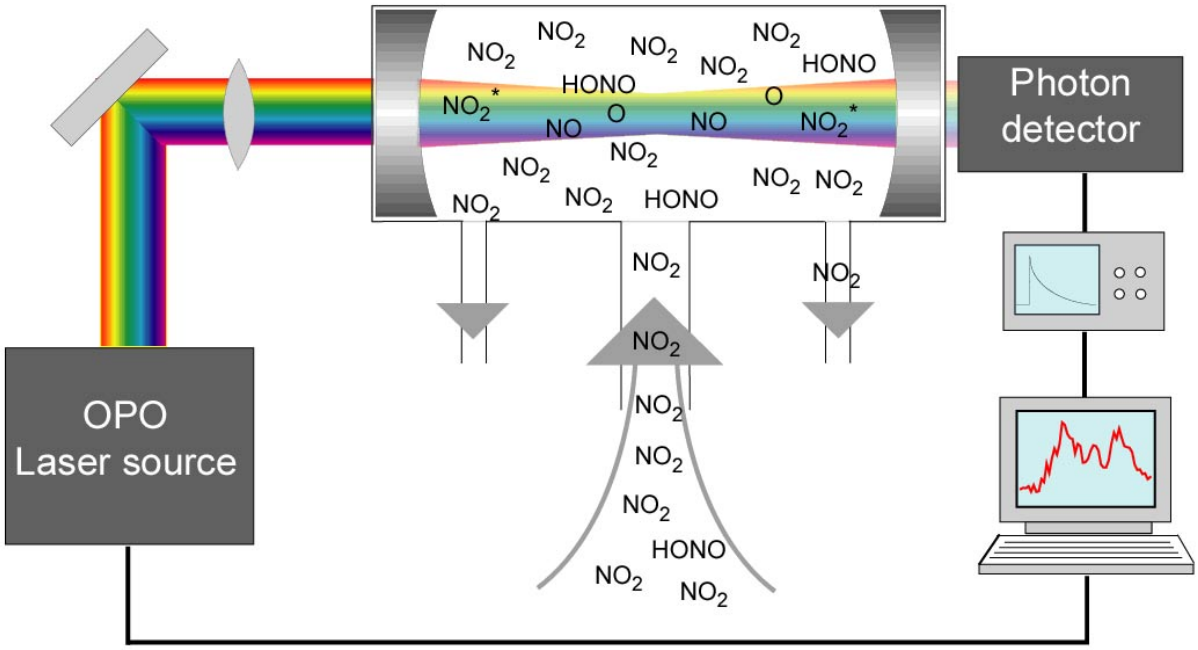

Dissertation

von

Bernhard Koch

Atmospheric Traces Monitoring
Using
Cavity Ringdown Spectroscopy

Von der Fakultät für Umweltwissenschaften und Verfahrenstechnik der Brandenburgischen Technischen Universität zur Erlangung des akademischen Grades eines Doktors der Naturwissenschaften genehmigte Dissertation

von

Diplomchemiker

Bernhard Koch

aus Ulm

Gutachter:	Prof. Dr. Detlev Möller
	Prof. Dr. Ludger Wöste
	Prof. Dr. Patrick Rairoux

Tag der mündlichen Prüfung: 18.06.2003

Für K.H.

Abstract

Cavity Ringdown laser Spectroscopy has been applied to develop a novel in-situ monitoring device for atmospheric trace gases. The study has been dedicated to the detection of NO_2 and HONO compounds which play an important role in atmospheric chemistry. The system, based on a Nd-YAG pumped UV-VIS OPO laser, has performed field experiments under harsh conditions showing high reliability and a detection limit in the 500 ppt range. Longer term measurements performed from the laboratory of the institute for air chemistry (BTU Cottbus) in Berlin-Adlershof in autumn and winter 2001/2002 showed very good coincidence with the results of the Berliner Luftgüte Meßnetz (BLUME). Present limitations in the performance have been elucidated putting in to evidence the effect of the aerosol content of the atmosphere. On the other hand, the possibility of quantitative aerosol analysis could be demonstrated.

Kurzzusammenfassung

Unter Anwendung der Cavity Ringdown Laserspektroskopie wurde ein neuartiges Verfahren zur in-situ Messung atmosphärischer Spurengase entwickelt. Hierbei konzentrierte sich die Arbeit auf den Nachweis von NO_2 und HONO, Verbindungen die in der Chemie der Atmosphäre eine entscheidende Rolle spielen. Das System, dessen Kernstück ein mittels eines Nd-YAG gepumpter UV-VIS OPO-Laser bildet, zeigte selbst auf Feldmesskampagnen unter widrigen Verhältnissen eine hohe Zuverlässigkeit und lieferte Nachweisgrenzen im 500 ppt Bereich. Darüber hinaus wurden vom Institutsgebäude der AG Luftchemie (BTU Cottbus) in Berlin-Adlershof aus im Herbst und Winter 2001/2002 Langzeitmessungen durchgeführt die eine sehr gute Übereinstimmung mit den Werten des Berliner Luftgüte Meßnetzes (BLUME) zeigten. Es konnten die derzeitigen Grenzen der Möglichkeiten des Versuchsaufbaus aufgezeigt und teilweise auf den Aerosolgehalt der Atmosphäre zurückgeführt werden. Auf der anderen Seite bietet das Experiment die Möglichkeit zur Analyse und Quantifizierung von Aerosolen.

Table of Contents

Atmospheric Traces Monitoring
Using Cavity Ringdown Spectroscopy

1. General Introduction

1.1. Motivation

Ever since the formation of our planet its atmosphere was subject to changes concerning composition, temperature, and self-purification power. However, during the last two centuries especially the atmospheric composition is shifting faster than ever before in the history of mankind. The effects of these changes are getting more and more distinct as can be seen in acid rain, corrosion processes, smog, and depletion of the ozone layer. Another well-known effect is the global warming by greenhouse gases, which is at least partially counterbalanced by the emission of particulate matter and the formation of aerosols. Remarkably, these aggravating effects are not based on a shift of the major atmospheric components: except for the strongly variable content of water vapour, the concentration of the gases which amount to more than 99.9% of the terrestrial atmosphere, that is nitrogen, oxygen, and the noble gases, remained almost constant for a much longer time than mankind exists on the planet. Responsible for the outlined effects are the mostly increasing contents of the so-called trace gases. For example, sulphur dioxide SO_2 (maximum volume mixing ratio $50 \cdot 10^{-9}$ which corresponds to < 0.000005%) causes acid rain and corrosion of stone and metal, nitrogen oxides NO_x (mixing ratio $1 \cdot 10^{-7}$-$1 \cdot 10^{-12}$) are responsible for photochemical smog, and the chlorofluorocarbons CFC (mixing ratio $1 \cdot 10^{-9}$) deplete the stratospheric ozone layer. Furthermore, together with methane CH_4, dinitrogen monoxide N_2O, and carbon dioxide CO_2 (with a mixing ratio of $350 \cdot 10^{-6}$ the predominant trace gas in the atmosphere), CFCs enhance the greenhouse effect. The hydroxyl-radical OH, which plays a main role as atmospheric detergent, even shows mixing ratios of less than $0.01 \cdot 10^{-12}$ (Graedel and Crutzen, 1989).

Thus, the understanding and survey of chemical and physical processes taking place in the atmosphere leads to the necessity of monitoring the traces compounds in concentration ranges laying below the part per billion volume mixing ratio (sub-ppbv). This is especially true for example for tropospheric photochemical ozone precursors like NO_x, nitrous acid (HONO), OH, and Volatile Organic Compounds (VOCs) (National Res. Council, 1991). Focusing in more detail on the specific chemical processes, it can be seen that trace species play an important role in the case of the oxidation capacity of the atmosphere. The OH-radical represents a famous example which contributes considerably to this oxidation capacity in spite of its extremely low occurrence. It can be detected by few instruments only. Aromatic hydrocarbons, formaldehyde (HCHO), and hydrogen peroxide (H_2O_2) represent further trace compounds which can be regarded as key species for atmospheric chemistry (Crutzen and Graedel, 1995). Furthermore, the primary pollutants like NO_x and SO_2 should be detectable in the ppt to ppb range, which is the concentration range of the unstressed clean atmosphere. Some more examples for measurements demanding this high sensitivity are examinations on heterogeneous chemical processes in tropospheric clouds and fog (Möller and Mauersberger, 1992) or the assessment of the influence of air masses on the local pollution during long-distance transport processes.

The thesis is dedicated to the development of new atmospheric traces monitoring device based on the cavity ring-down laser spectroscopy (CRDS) method. CRDS is a very sensitive optical method, which can perform point measurements of an optical extinction based on a long path absorption, whereby the path length is achieved within a short (meter range) high reflecting optical cavity. Generally, optical spectroscopic techniques offer the big advantages of being direct, inherent calibrating, non-contacting, and non-intrusive. (A short review of ground based spectroscopic measurements of atmospheric gases is given by Schiff (1992)). However, in contrast to remote sensing optical methods like DOAS and LIDAR, CRDS represents an in-situ technique. The method is especially attractive because the optical absorption is evaluated by the measurement of a time constant rather than an intensity ratio regarding Lambert- Beer’s law. Hence, it is insensitive against variation in the laser energy. The CRDS-technique will be able to perform in-situ multi-compounds analysis which makes it very outstanding in this respect. For analytes absorbing in the same wavelength range even simultaneous measurements will be possible. Advances in laser technology enable scanning ranges of 0.2 – 2 µm, making the set-up applicable to a wide range of species. The whole system should be highly reliable, robust, compact, and easy to handle and, thus, it should be well suited for installation and integration in mobile platforms.

This thesis is focused on the detection of NO_2 and HONO. Because NO_2 can be well monitored by standard in-situ monitoring devices based on photoluminescence, the analysis of this compound is well suited for performing devices comparison. Both HONO and NO_2 play an important role in atmospheric chemistry (National Res. Council, 1991) and contribute to the atmospheric oxidation (rethinking the ozone) process.

To summarise, novel aspects of the technique introduced in this thesis are:

- first CRDS analysis of ambient outer air (choosing NO_2 and HONO as exemplary analytes)
- first application of CRDS on field campaigns
- in-situ air measurements applying an optical absorption method
- CRDS analysis in the UV/Vis spectral range

Finally it should be mentioned that CRDS is not restricted on atmospheric traces monitoring, in fact this technique can be applied in a multitude of different fields like, for example, the spectroscopy of metal clusters, the study of free radicals in combustion systems (flame and plasma diagnostics), for chemical kinetics analysis, and for measurement of high overtones of molecular vibrations (Paul and Saykally, 1997).

The **first chapter** of this thesis comprehends the atmospheric chemistry and analytics of the selected trace compounds NO_2 and HONO followed by an introduction to the CRDS-technique and its evaluation procedures. It closes with a unifying section giving a survey of the application of CRDS on atmospheric analysis. The experimental set-up including data acquisition and parameter optimisation is described in the **second chapter**. A presentation of the results obtained with the CRDS set-up developed in the course of this work is given in the **third chapter**. It starts with laboratory measurements followed by analysis of the ambient Berlin air and a demonstration of results acquired during a field campaign in the Taunus region near Frankfurt. It closes with a discussion and preview on aerosol analysis.

1.2. Atmospheric Chemistry of Nitrogen Oxides and Related Compounds

1.2.1. Survey of the Oxidation Scheme

Oxides of nitrogen play a central role in atmospheric chemistry (National Res. Council, 1991) and contribute to the atmospheric oxidation process. The global emission of NO_x amounts to 15-25 Tg N yr^{-1} by natural and to 22-30 Tg N yr^{-1} by anthropogenic processes (Möller, 1996). Mixing ratios of NO_x in the troposphere vary by more than 5 orders of magnitude from 100 ppb levels in urban environments to a few ppt levels in remote areas (Crawford et al., 1997). NO_2 is key to the formation of tropospheric ozone, contributing to acid deposition, and forming other atmospheric oxidants such as the nitrate radical. In addition, in the stratosphere nitrogen oxide chemistry and that of halogens interact closely to control the chain length of ozone-destroying reactions. The overall oxidation sequence is conversion of NO to NO_2, which is ultimately converted to HNO_3 and oxidised forms such as PAN. Nitric acid undergoes both wet and dry deposition rapidly and can be neutralised by ammonia, the major gaseous base found in the atmosphere. Thus, as NO is converted ultimately to HNO_3, important nitrogenous intermediates are formed along the way (Finlayson-Pitts and Pitts, 2000). An overview of the reactions of nitrogen oxide and related compounds is given in **Fig. 1.1.**. Photochemical reactions are especially indicated in the scheme.

In the next two sections the look is focused on the compounds analysed in the course of this thesis, nitrogen dioxide (Finlayson-Pitts and Pitts, 2000) and nitrous acid (Schiller et al., 2001).

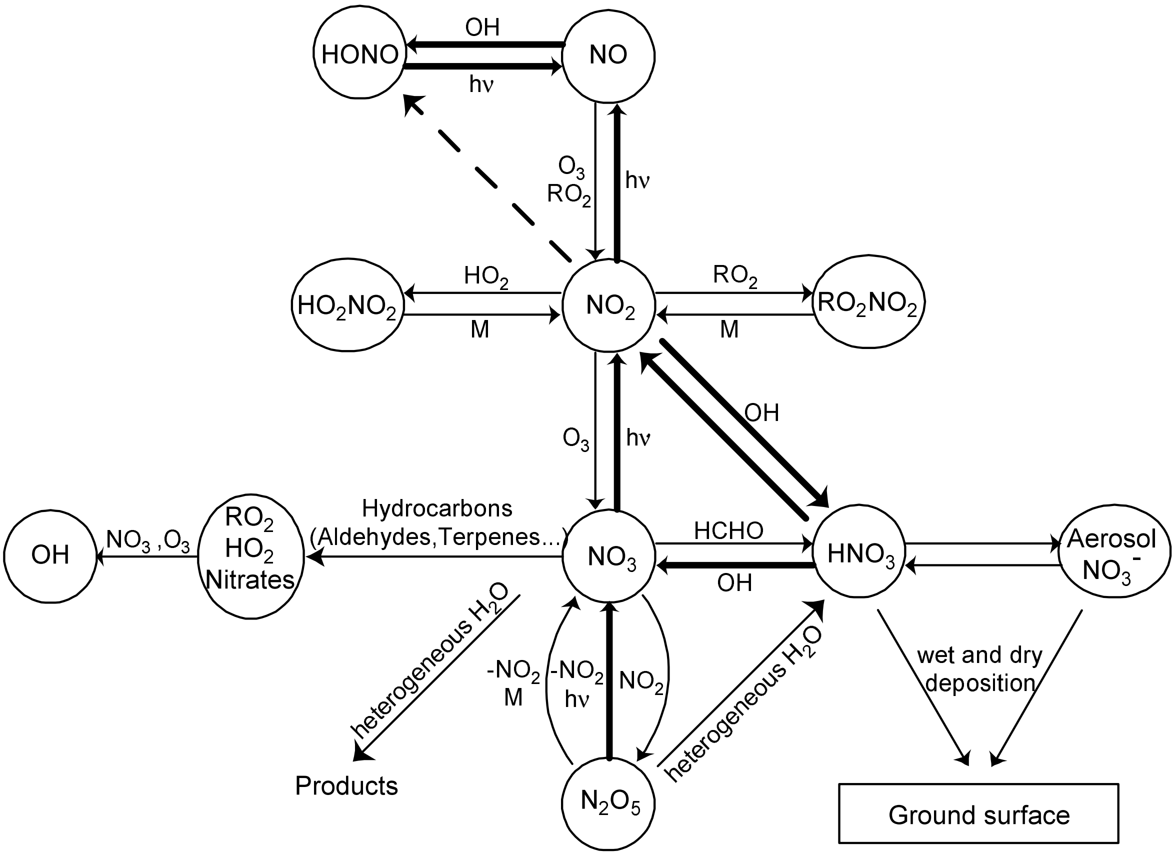

Fig. 1.1. Oxidation scheme for nitrogen oxides and related compounds. Photochemical processes are indicated by bold arrows. Adapted from Plane (1994), Möller (1996), Warneck (2000).

1.2.2. Nitrogen Dioxide

Oxidation of NO to NO_2

Most of the primary emissions of NO_x are in the form of nitric oxide NO, which outweighs NO_2 by a factor of 5 - 10. In an atmosphere containing only NO, NO_2, and air, that is, no organics, the reactions controlling the concentrations of NO and NO_2 are:

$$NO_2 + h\nu\ (\lambda \leq 420\ \text{nm}) \rightarrow NO + O(^3P) \tag{1}$$

$$O(^3P) + O_2 \xrightarrow{M} O_3 \tag{2}$$

$$O_3 + NO \rightarrow NO_2 + O_3 \tag{3}$$

In this “photostationary state” the ratio of concentrations of O_3, NO, and NO_2 should be a constant which is expected to change during the day as $k_p(NO_2)$ changes with the solar zenith angle. Deviations occur when the conversion of NO to NO_2 occurs by reactions other than that with O_3:

$$HO_2 + NO \rightarrow OH + NO_2 \tag{4}$$

$$RO_2 + NO \rightarrow RO + NO_2 \tag{5}$$

Further deviations can be related for ozone loss processes other than reaction (3) like photolysis of O_3, reactions with NO_2, alkenes, and the radicals HO_2 and OH.

Oxidation of NO_2

1. Daytime gas-phase reaction with OH

NO_2 reacts readily with OH, forming nitric acid:

$$NO_2 + OH \xrightarrow{M} HONO_2 \tag{6}$$

The lifetime of NO_2 with respect to this reaction (6) is 16h. This reaction is primarily a daytime reaction because most OH sources are photolytic in nature. The reaction of NO_2 with OH competes with NO_2 photolysis according to reaction (1). It is usually not a dominant loss process for NO_2, but it is still sufficiently fast to form significant amounts of HNO_3 particularly in polluted regions.

2. Nighttime reactions to form NO_3 and N_2O_5

NO_2 also reacts with O_3, forming the nitrate radical NO_3:

$$NO_2 + O_3 \rightarrow NO_3 + O_2 \tag{7}$$

Despite of the relatively small rate constant of this reaction the lifetime of NO_2 is only 3.5 h at an O_3-concentration of 100 ppb. NO_3 is recognized to be a major contributor to the chemistry of organics in the troposphere at night. Because it absorbs in the red region of the spectrum, it photolyses rapidly during the day so that its chemistry other than photolysis is essentially restricted to the dark hours. Brown et al. (2001) observed a clear rise in the NO_3 signal after sunset and a sudden disappearance at sunrise. The rise takes place over a course of 1-2 hours, while the sunrise disappearance of NO_3 is essentially instantaneous.

In a reversible, equilibrum reaction NO_3 reacts with NO_2 forming dinitrogen pentoxide:

$$NO_3 + NO_2 \xleftrightarrow{M} N_2O_5 \tag{8}$$

3. Reactions of NO and NO_2 with water and alcohols

Uptake into and reaction with liquid water

NO and NO_2 are not highly soluble and, in addition, the reactions are kinetically rather slow due to the dependence of the rates on the square of the reactant concentration. The Henry's law constant, which is in effect the equilibrium constant for the gas-solution equilibrium X(g) ↔ X(l), shows a low value of $\approx 10^{-2}$ mol l^{-1} atm^{-1} (for NO_2). For comparison, highly soluble gases have Henry's law constants in the order of 10^5. It must be concluded, that the uptake of NO and NO_2 into clouds and fog, followed by their oxidation in the liquid phase, will not contribute significantly to the formation of nitrate and acidity in fogs and clouds under most conditions. The major source of HNO_3 therein should be the oxidation of NO_x to gaseous HNO_3, followed by its facile uptake into the condensed phase.

"Heterogeneous" reaction of NO_2 with water vapour

The mechanism of this "dark" reaction to form HONO is still not understood. Potential formation processes and reactions of HONO in the atmosphere have been reviewed by Lammel and Cape (1996). It occurs on a variety of surfaces, including water and acid surfaces (Kleffmann et al., 1998), and on soot as well.

$$2NO_2 + H_2O \xrightarrow{surface} HONO + HNO_3 \tag{9}$$

The observed kinetics depend on the surface-to-volume ratio of the reaction vessel, clearly indicating a heterogeneous reaction on the surface. While HONO is always produced, equivalent amounts of HNO_3 could not be observed. This is explained by the “sticky” nature of HNO_3 which makes it adsorb strongly on the walls of the reactor.

While the bulk reaction discussed in the previous section is second order in NO_2, the heterogeneous reaction is first order in NO_2 and water vapor (e.g., Kleffmann et al., 1998). In addition, this type of reaction is enhanced by light in the actinic region.

Fast reduction of NO_2 was observed on soot with subsequent formation of HONO. The yields were higher as the expected 50% according to reaction (9).

Reaction with alcohols

A similar reaction according to reaction (9) takes place:

$$NO_2 + ROH \xrightarrow{surface} RONO + HNO_3 \qquad (10)$$

While the homogeneous gas-phase reaction is slow, the reaction on surfaces is much faster. These heterogeneous reactions may play an important role in laboratory apparatus, in sampling systems, and perhaps in ambient air, however, they are not yet well understood (Finlayson-Pitts and Pitts, 2000).

1.2.3. Nitrous Acid

Nitrous acid (HONO) plays an important role in the production of photochemical smog due to its accumulation at night (Platt et al., 1980) followed by subsequent photolysis at sunrise. This photolysis of HONO is a direct source of the hydroxyl radical OH:

$$HONO + h\nu\ (\lambda < 400\ nm) \rightarrow OH + NO \qquad (11)$$

The liberated OH radicals initiate and drive the oxidation of hydrocarbons in the atmosphere, as well as other species such as CO and SO_2. Nitrous acid thus directly affects the oxidative capacity of the atmosphere and indirectly contributes to secondary pollutants which are products of that oxidation (Schiller et al., 2001).

HONO exhibits a strong diurnal variation with a nocturnal maximum and daytime minimum typically below current detection limits. Peak night-time concentrations have been measured in the range of 8 to 14 ppb (Harris et al., 1982; Appel et al., 1990; Lammel et al., 1996) for Los Angeles, while at a rural site in the UK mixing ratios as high as 2 ppb have been recorded (Kitto and Harrison, 1992). Photolysis results in a rapid decrease in concentrations shortly after sunrise and HONO may thus play an important role as a source of OH when other photochemical activity is low (Harris et al., 1982). This early morning pulse of OH may be characterised indirectly by measuring the HONO decline during this period.

Atmospheric sources are, at present, not well characterised. Platt (1986) proposed three groups of possible source mechanisms: (1) Homogeneous gas-phase reactions, (2) Direct emission and (3) Heterogeneous production on surfaces of aerosols. Although homogeneous gas-phase production is likely to have little impact on the night-time production rate, direct emission and heterogeneous production on surfaces of aerosols are probably both important sources of the HONO accumulating during the night. Measurement of night-time HONO with good spatial and temporal resolution (as given by CRDS) should aid in understanding the production of nitrous acid as well as possible loss mechanisms. Schiller et al. (2001).

Furthermore, HONO is an important indoor air pollutant, and its reactions with amines can lead to carcinogeneous nitrosamines under atmospheric conditions (see Wang and Zhang, 2000).

1.3. Photochemistry of NO_2

1.3.1. General Spectral Features

The absorption spectrum of NO_2 displays two broad continua centred at ca. 400 and 210 nm with underlying fine structure. In the troposphere the filtering effect of O_3 means that only light of wavelengths longer than about 300 nm is intense enough to initiate photochemistry. The thermodynamic threshold for dissociation of NO_2 into $O(^3P)$ atoms and NO is 398 nm (Okabe, 1979; Crowley and Carl, 1997). However, the experimental observations indicate that O atom production takes place out to 424 nm, where excess energy is provided by a combination of rovibrational excitation and energy transfer from bath-gas molecules (Roehl et al., 1994). The complexity of the NO_2 spectrum is due to strong coupling between the $^2A_1$ ground state and the $^2B_1$ and $^2B_2$ excited states, yielding optically excited states that have considerable ground electronic state character. The high density of states results in an excited-state radiative lifetime of between 30 and 200 μs, depending upon excitation wavelength. In contrast, the lifetime of the dissociative state is close to $1 \cdot 10^{-13}$ s (Crowley and Carl, 1997). **Fig. 1.2.** shows the absorption spectrum of NO_2 between 250 and 650 nm, multiplied by the wavelength-dependent quantum yields. The dotted line thus represents dissociation to NO and $O(^3P)$ and the solid line excitation to longer lived excited states which are designated as NO_2^*.

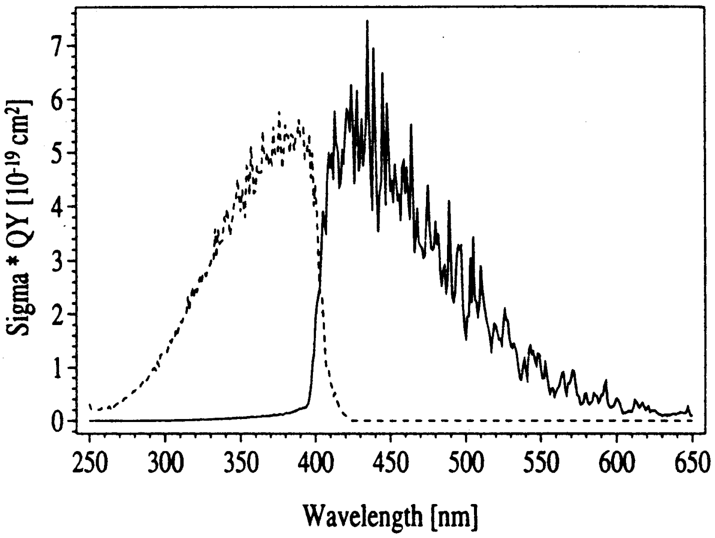

Fig. 1.2. Uv/vis absorption spectrum (Sigma = absorption cross section) of NO_2 multiplied by the quantum yield (QY) for dissociation $O(^3P) + NO(^2\Pi)$ (dotted line) and by the quantum yield for photoexcitation to NO_2^* (solid line). Crowley and Carl (1997).

1.3.2. Nondissociative Reactions of NO_2

$$NO_2 + h\nu \rightarrow NO_2^* \qquad (12)$$

The fate of the excited NO_2^* will be determined by its fluorescence lifetime or quenching according to (Crowley and Carl, 1997)

$$NO_2^* + O_2 \rightarrow NO_2 + O_2(^1\Delta_g) \qquad (13)$$

The quenching rate constants differ for the major bath gases and have been measured as $2.7\cdot10^{-11}$ cm^3 molecule^{-1} s^{-1} for N_2, $3.0\cdot10^{-11}$ cm^3 molecule^{-1} s^{-1} for O_2, and $1.7\cdot10^{-10}$ cm^3 molecule^{-1} s^{-1} for H_2O (Okabe, 1978).

At ground level the total quenching rate is $7.1\cdot10^8$ s^{-1}, resulting in a NO_2^* lifetime of about 1.4 ns which is thus controlled almost exclusively by collisional quenching

$$NO_2^* + M \rightarrow NO_2 \qquad (14)$$

As the quenching rate constants show, H_2O is a particular efficient quencher of NO_2^* and, despite its low concentration when compared to N_2 and O_2 in the troposphere, contributes remarkably to the total quenching rate. Assuming 0.2 bar of O_2, 0.8 bar of N_2, and 0.013 bar of H_2O the latter will contribute about 8% to the total quenching rate. Furthermore, it can be shown that the generation of OH radicals and HONO becomes a thermodynamically feasible reactive quenching mechanism (Crowley and Carl, 1997).

$$NO_2^* + H_2O \rightarrow OH(^2\Pi) + HONO(^1A) \qquad (15)$$

$$(\Delta H_r = -25\ \text{kcal/mol})$$

This reaction (15) is exothermic even for wavelengths greater than 600 nm. By contrast, the reaction of ground-state NO_2 with H_2O to yield HONO and OH is 40 kcal/mol endothermic.

The influence of H_2O onto the quenching rate and the production of HONO from NO_2^* according to reaction (15) will cause problems concerning the compatibility of laboratory measurements on standard gases and clean air compared to measurements on ambient outside air.

Electronically excited NO_2^* is able to react with ground-state NO_2 according to the following reactions, which both would be endothermic for interaction between two ground-state NO_2 molecules (Nizkorodov et al. 1994):

$$NO_2^* + NO_2 \rightarrow 2NO + O_2 \qquad (16)$$

$$NO_2^* + NO_2 \rightarrow NO_3 + NO \qquad (17)$$

In addition, small yields of N_2O have been observed by Zellner et al. (1992) in the reactive collisional quenching of NO_2^* by N_2. All these reactions can influence the NO_2-concentrations in the ambient air AND in the measurement cell, a fact which should be kept in mind for further discussions.

The laser excitation experiment by Crowley and Carl (1997) shows that two-photon absorption of NO_2 at wavelengths between 430 and 450 nm is facile and leads to $O(^1D)$ production. They suggest that a transition from the initially populated mixed NO2* $(^2B_1/^2B_2/^2A_1)$ state to the dissociative NO_2^{**} (2^2B_2) state is possible at wavelengths close to 440 nm. This transition is allowed due to the partial ground-state nature of NO_2^* and corresponds to absorption of a single photon of wavelength close to 220 nm to the 2^2B_2 state. The 2^2B_2 state dissociates to give $O(^1D)$ and $NO(^2\Pi)$ with substantial $O(^3P)$ yields.

An estimation of the cross section of NO_2^* gives values similar to those of ground-state NO_2. A comparison with the $O(^1D)$ production rate via O_3 photolysis renders this two-photon-absorption process uninteresting for the atmosphere, however it plays an important role under laboratory conditions with strong photon fluxes. In addition, $O(^1D)$ might react with NO_2 instead of O_2 in O_2-free atmosphere and is able to reduce the NO_2-concentration by producing NO and O_2.

1.3.3. Dissociation of NO_2

In the wavelength range of interest, NO_2 photolysis occurs as follows (Roehl et al., 1994):

$$NO_2 + h\nu \rightarrow NO(X^2\Pi) + O(^3P) \tag{18}$$

In the absence of O_2 subsequent reaction of O with NO_2 produces a second NO molecule

$$NO_2 + O \rightarrow NO + O_2 \tag{19}$$

lowering the NO_2-concentration. By using O_2 (or air) as buffer gas rather than N_2, the O-atom will react with O_2 instead of NO_2 forming ozone ($O + O_2 \rightarrow O_3$). At higher pressures (>0.1 bar) and lower temperatures, the third body reaction

$$O + NO_2 + M \rightarrow NO_3 + M \tag{20}$$

becomes significant to several percent of reaction (19). The NO_3 produced in this reaction can react with the photolysis product NO

$$NO_3 + NO \rightarrow 2NO_2 \tag{21}$$

In addition, Roehl et al. (1994) state that the reaction of excited NO_2^* with O_2, as postulated by Zellner et al. (1992), is not occurring under the conditions of their study and is unlikely to be of atmospheric relevance:

$$NO_2{}^* + O_2 \xrightarrow{not} NO + O_3 \tag{22}$$

However, Zellner et. al (1992) observed the reaction:

$$NO_2{}^* + N_2 \rightarrow NO + N_2O \tag{23}$$

Although this reaction is energetically possible and both spin and orbital symmetry allowed, the yield was extremely small.

Fluorescence lifetimes of NO_2 molecules just below the dissociation limit are anomalously long (Patten et al., 1990), in the neighbourhood of 50 – 100 μs, owing to the coupling between ground and excited electronic states. Therefore, such molecules will be subject to collisions at pressures of a few mbar or greater. Collisional up-pumping with bath gas molecules additional to rovibrational energy can explain photodissociation beyond the thermodynamic threshold (Roehl, et a., 1994). Quantum yields for NO_2 recommended by Roehl et al. (1994) are displayed in **Fig 1.3.**:

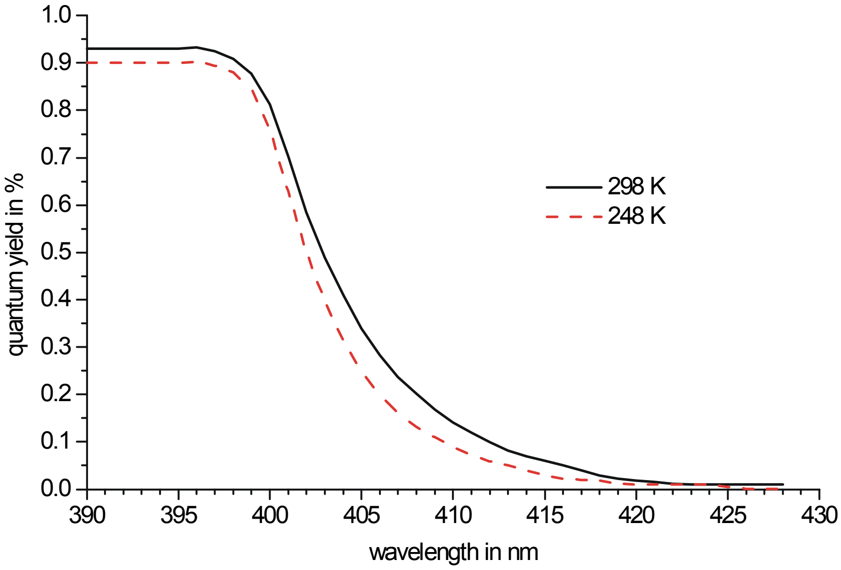

Fig. 1.3. Recommended NO_2 quantum yields vs wavelength at 298 and 248 K (adapted from Roehl et al., 1994).

1.4. Analytics of NO_2 and HONO

1.4.1. NO_2-Analysis

The most common technique used to measure atmospheric NO_2 is Photo-Fragmentation Chemi-Luminiscence (PF-CL), in which photolytic conversion of NO_2 to NO is followed by chemiluminiscence detection of NO_2 (Thornton et al., 2000). Photolysis is accomplished using UV light from a filtered xenon arc lamp ($\lambda \approx 375$ nm) in a flowing sample. O_3 is added to the sample flow in the photolysis cell where it reacts with NO to produce electronically excited NO_2. The excited NO_2^* emits a broad continuum of radiation peaking at 1.3 μm. The visible portion of this emission between 500 nm and 900 nm is detected using a red-sensitive PMT This standard technique was introduced by Clough and Thrush (1967). Such instruments are commercially available with detection limits of 155 ppt (Dias-Lalcaca et al., 1998), and custom-built versions have reached still lower detection limits.

Bradshaw et al. (1999) used two-photon laser-induced fluorescence in place of the O_3-chemiluminiscence reaction to measure NO derived from the photolysis of NO_2. This Photo-Fragmentation Two-Photon Laser-Induced Fluorescence (PF-TP-LIF) instrument uses the third harmonic of a Nd^{3+}:YAG laser for the photolysis of NO_2 and two-photon excitation of the C state of NO followed by fluorescence as a means of NO detection. A detection limit of 8 ppt is reported, however, in several studies the accuracy of this instrument is questioned because of possible interferences which might be attributed to surface decomposition of other NO_2 containing species. The shortcomings of the PF-CL and PF-TP-LIF detection methods are (Thornton et al., 2000):

- the indirect nature of the photolysis step and consequent uncertainty about the response to other NO_2 containing compounds
- the requirement for a simultaneous NO measurement and the associated need to determine NO_2 as the difference between NO_x and NO
- the large size, weight, and electrical power consumption of these instruments

Another commonly used technique for NO_2 detection is the luminol-chemiluminiscence method, first developed by Wendel et al. (1983). Instruments based on this method are commercially available. The technique employs reaction between NO_2 and a solution of luminol resulting in fluorescence peaking near 425 nm. The technique is direct and sensitive, but it is non-specific. Gaffney et al. (1998) and Marley et al. (2002) reported a gas chromatographic separation of NO_2 and C_2-C_4 peroxy nitrates, followed by detection using luminol with ppt sensitivity. Furthermore, losses of NO_2 on a variety of common materials (e.g., Al and Cu) were shown, suggesting an advantage for techniques with rapid flow rates and a minimum of surface contact between the instrument and the sample.

Thornton et al. (2000) describe a portable laser-induced fluorescence (LIF) instrument for continuous, autonomous, in situ observations of NO_2 with a detection limit of 15 ppt. The technique is spectroscopically specific and does not require conversion of NO_2 into another species like NO prior to detection. A frequency doubled Nd^{3+}:YAG laser at 532 nm pumps a dye laser, the output (585 nm) is sent to a multipass White Cell. The NO_2 fluorescence is collected and sent to a PMT. However, in the presence of other trace gases interference effects will cause a decisive deterioration of the detection limit. Fong and Brune (1997) developed a FAGE system (fluorescence assay by gas expansion) and excited the NO_2 sample at two wavelength alternately around 564 nm. These measurements at a peak and bottom wavelength can avoid the interference of fluoresecent species other than NO_2, however, a very high spectral resolution of the laser system is required (0.003 nm). The detection limit was 280 ppt. Originally, FAGE was developed by George and O’Brien (1991) in order to reduce collisional quenching and lengthen fluorescence lifetimes due to low-pressure conditions. LIF-measurements in the favourable 440 nm band were performed by Matsumi et al. (2001) with reported detection limits of 30 ppt.

Tunable diode laser absorption spectroscopy (TDLAS) has demonstrated a capability for in situ detection at 400-700 ppt with approximately 100 m path lengths (e.g. Schiff et al., 1990). Garnica et al. (2000) developed a detection system for atmospheric NO and

NO_2 using an atmospheric pressure laser ionisation (APLI) technique, which was based on time-of-flight mass spectrometry with resonance enhanced multiphoton ionisation (REMPI). The detection limit was 7 ppt, however, the laser system is still bulky and does not allow the use for mobile operation.

In photoacoustic spectroscopy some of the energy gained by a molecule when it absorbs light is lost by collisional relaxation which then appears as heat. If the light source is pulsed the local heat generation gives rise to pressure waves which can be detected by a microphone (Schiff, 1992). As the signal does not depend on the absorption path length, small and simple apparatus integrated in mobile systems can be introduced as can be seen in the review by Meyer and Sigrist (1990). A method for high-precision pulsed photoacoustic spectroscopy in NO_2-N_2 was recently presented by Slezak (2001).

Long-path differential absorption (DOAS) has been used to detect atmospheric NO_2 (Platt et al., 1980; Plane, 1994) with a sensitivity of 250 ppt using a 20.6 km folded path length (Harder et al., 1997). Laser imaging detecting and ranging (LIDAR) has detection limits near 200 ppb for NO_2, limiting its current use to studies near the combustion sources of NO_x (Plane, 1994; Strong and Jones, 1995; Wolf, 1998). All these techniques are spectroscopically specific to NO_2.

Merienne et al. (1995) presented detailed absorption cross sections in 0.01 nm – steps which are fundamental for any absorption measurement. The analysis performed in this thesis are based on these values depicted in **Fig. 1.4.**.

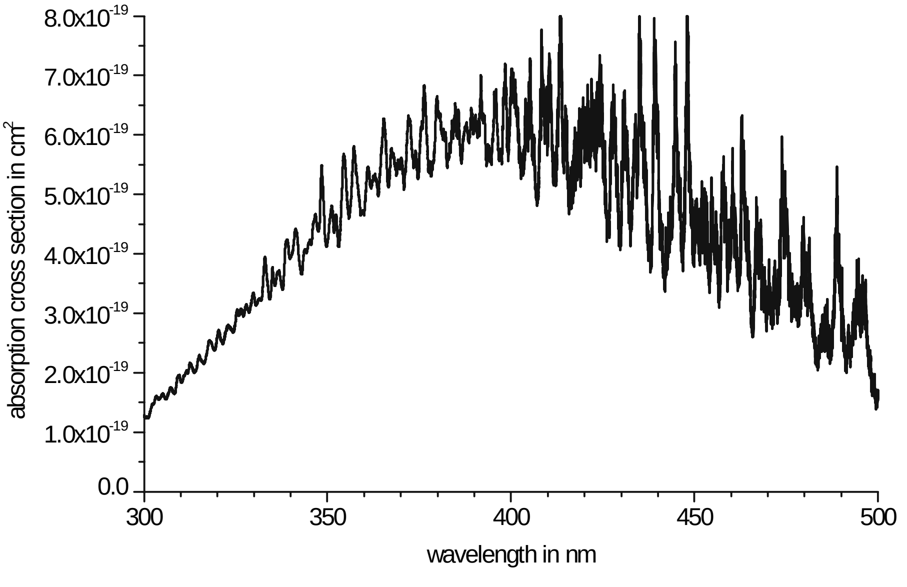

Fig. 1.4. Absorption cross sections of NO_2 in the wavelength range 300 – 500 nm. Merienne et al. (1995).

1.4.2. HONO-Analysis

Although several laboratory studies of nitrous acid have been recorded, relatively few field measurements of HONO in the gas phase have been carried out (Schiller et al., 2001). Atmospheric gas phase concentrations were first measured using long path differential optical absorption spectroscopy (DOAS) in the near UV region (Perner and Platt, 1979) and have since been measured by a number of groups (Platt et al., 1980, Harris et al., 1982, Andres-Hernandez et al., 1996, Febo et al., 1996). This technique requires pathlengths generally greater than 1 km, and so the spatial distribution cannot be well resolved. Ambient nitrous acid has also been measured by collection on an alkali-coated denuder followed by analysis of NO_2^- by ion chromatography (e.g., Sjödin and Ferm, 1985, Febo et al. 1993, Acker et al., 2001, Huang et al., 2002). The loss of NO_2^- due to oxidation to NO_3^- by O_3 can lead to an underestimate of the HONO present, while the formation of HONO as an artefact on the denuder can lead to an overestimate. Since it is the nitrite ion that is measured, any gas phase species that yields NO_2^- in solution, (e.g., NO_2) acts as a potential interference. Wingen et al (2000) have developed a laboratory technique for measuring HONO that uses an excess of HCl to convert all the HONO to ClNO and measures the ClNO with FTIR spectroscopy.

Like FTIR and DOAS, tunable diode laser absorption spectroscopy (TDLAS) and CRDS directly sample HONO in the gas phase, minimising the possibility of artefacts, but at a higher sensitivity than FTIR and with greater spatial resolution than DOAS due to point sampling. Applying TDLAS, Schiller et al (2001) obtained detection limits in the sub-ppb-level using a 1.5 m white cell with a folded pathlength of 126 m in the mid-infrared. However, the restricted tuning range necessitates different laser moduls for the detection of different species, a disadvantage which is overcome by CRDS.

Stutz et al. (2000) published detailed measurements of the absorption cross sections of HONO which are presented in **Fig. 1.5.**. They applied a high-purity HONO-generation-system developed by Febo et al. (1995) which is suitable for the production of HONO-standards. Any analysis in this thesis refers to the values of Stutz et al. (2000).

As HONO absorption measurements have to be regarded as a multicomponent analysis together with NO_2, a sum spectrum of NO_2 (**Fig. 1.4.**) and HONO (**Fig. 1.5.**) is presented in **Fig. 1.6.**. This combined spectrum was calculated for 10 ppb NO_2 and various concentrations of HONO around one of the main peaks of HONO at 368 nm. Obviously, a comparison of the peak height at 368 nm with the peak height at 372 nm gives a rough idea of the relation NO_2/HONO.

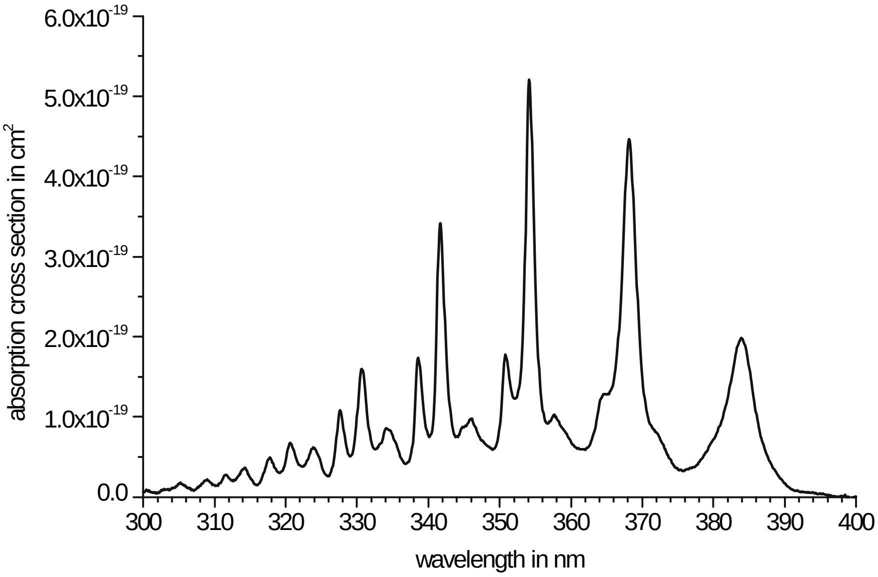

Fig. 1.5. Absorption cross sections of HONO in the wavelength range 300 – 400 nm. Stutz et al. (2000).

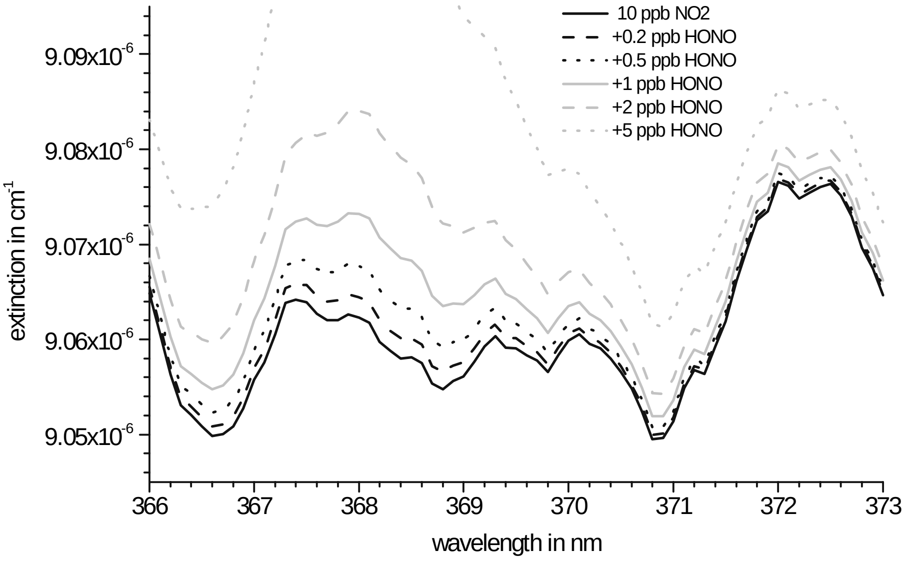

Fig. 1.6. Combined spectrum for 10 ppb NO_2 and various concentrations of HONO around the second main peak of HONO at 368 nm (see fig. 1.5.).

1.5. Cavity Ringdown Spectroscopy (CRDS)

1.5.1. Basic Principle of CRDS

The Cavity Ring-Down Spectroscopy (CRDS) is a sensitive laser absorption spectroscopy method developed by O'Keefe (1988) and has been applied for several years in laboratory condition to perform measurements of very low light absorption values (10^{-8}-10^{-10} cm^{-1}) of gaseous compounds (He et al., 1998). At the same time huge progresses in laser technology have been achieved, which allow to apply this spectroscopy technique for atmospheric traces monitoring. Complete overviews of CRDS research in the various experimental fields can be found in the review papers by Scherer et al. (1997), Wheeler et al. (1998), and Berden et al. (2000) as well as in the book by Busch and Busch (1999).

The basic principle of the cavity ringdown spectroscopy is depicted in **Fig.1.7.**. A short laser pulse is injected into an optical cavity composed of two highly reflective mirrors separated by a distance of less than one meter. In the absence of any absorbing substance in the volume between the two mirrors, the primary losses of the cavity will result from the small transmittance of the mirrors. Hence, the optical pulse is reflected back and forth within the cavity, but its intensity will gradually decrease with time as energy leaks out of the cavity. It is obvious that the intensity of the light in the cavity will take longer to decrease with mirrors of high reflectivity than for low reflectivity. The travelling time of the optical pulse within the cavity can reach some ten microseconds which represents an optical path length of several kilometres ($10\mu s \equiv 3$ km). The exponential decay of the signal with time resembles to a ringing pattern (recall the gradual decay of sound from a resonant bell). The measured parameter is the exponential decay time of the radiation in the cavity, which can be retrieved from the signal measured by a photon-detector placed on the back side of the cavity mirror.

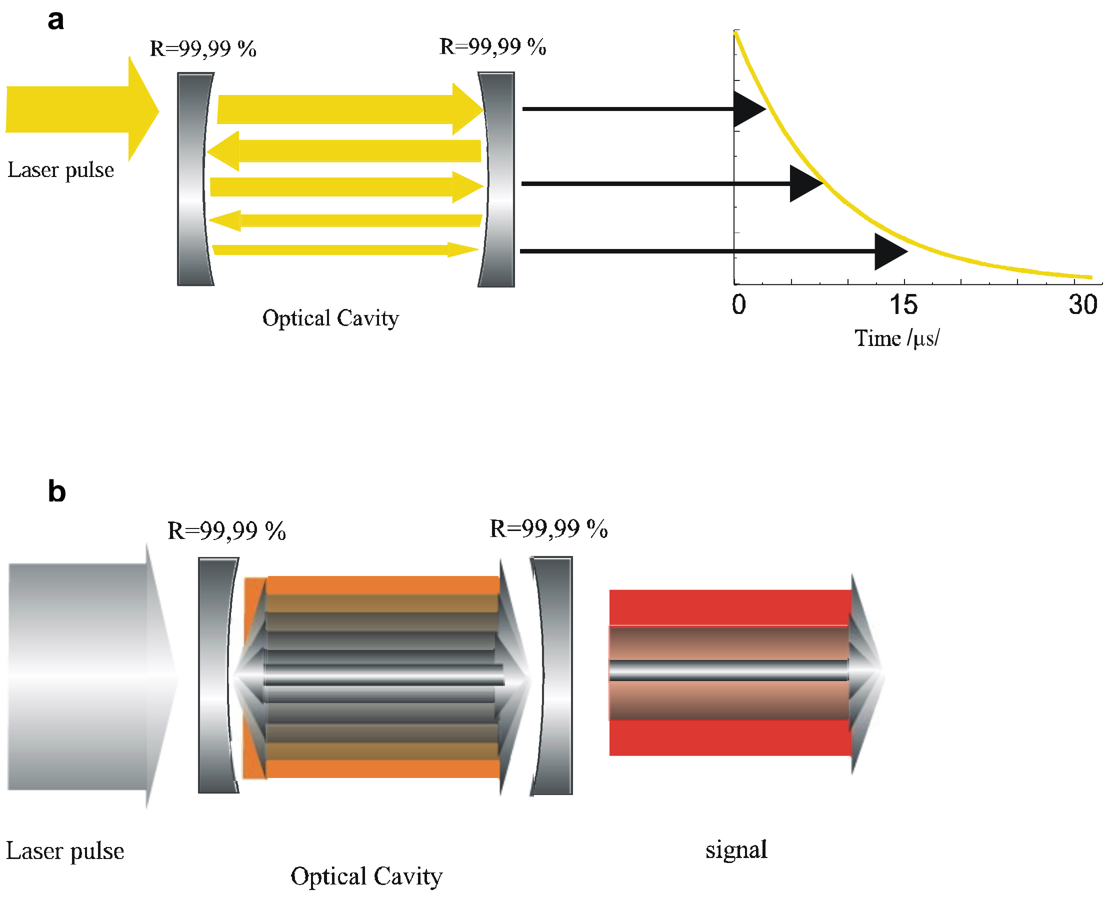

Fig.1.7. Basic principle of the cavity ringdown spectroscopy method. One should remember that the CRDS cavity is not a white cell as it might be indicated in fig. **a** in which the arrows representing the laser pulses had to be shifted for more clarity. A more realistic approach is made in fig. **b**, however, in this presentation it is harder to deduce the exponential decay curve.

If an absorbing species that obeys Lambert-Beer's law is introduced into the cavity, its presence will increase the losses with time of the laser radiation energy inside the cavity. As result, the exponential decay with time will be more pronounced. The mathematical expression of the detected signal $I(t, \lambda)$ is given by (a detailed derivation of this equation is presented in a separate section **1.5.2.**):

$$I(t, \lambda) = I_0 \cdot \exp \{ [-(1-R) + \Sigma\, \sigma_i(\lambda) \cdot N_i \cdot L)] \cdot c \cdot t \,/ L \} = I_0 \cdot \exp (-t / \tau) \qquad [1]$$

Where t is the time, λ the wavelength of the laser radiation, I_0 is the initial laser pulse intensity, R the mirror reflectivity, generally R>99,99 %, $\sigma_i(\lambda)$, the absorption cross-section of the ith species at the wavelength λ, N_i its concentration, c the speed of light, L the optical cavity length, τ the time constant of exponential signal time decay.

The question which has to be answered is: how long does it take the energy to leak out? This exclusively depends on the

- mirror transmission / reflectivity
- absorbing species within the cavity

and not on the intensity of the laser beam.
It also should be mentioned that for too high reflectivities (100%) the laser pulse is not able to enter the cavity.

It can be stated that the CRDS-method is based on the determination of a **time constant** of the exponential decay of the laser light leaking out of a high Q optical cavity. This is the main difference of this technique in regards to the conventional long path absorption spectroscopy where the determination of an absorption coefficient is related to the measurement of an intensity ratio. Evaluation of the time constants of the cavity filled with absorbing species $\tau(\lambda)$ and of the empty cavity $\tau_o(\lambda)$, respectively, allows the determination of the species' optical extinction $\alpha(\lambda)$ at the laser wavelength λ.

$$\alpha(\lambda) = \sum_i N_i \cdot \sigma_i(\lambda) = \frac{L}{c} \cdot \left(\frac{1}{\tau(\lambda)} - \frac{1}{\tau_0(\lambda)} \right) \qquad [2]$$

N_i is the concentration of the ith compound and $\sigma_i(\lambda)$ is its absorption cross section, c is the speed of light and L the cavity length. The concentration of the species can be deduced by scanning the laser wavelength in the absorption spectra of the species.

The determination of the concentration of several compounds generally needs a numerical approach based on a variable convolution of the differential absorption spectra (Pfeilsticker et al., 1999; Chapter 1.8. in this thesis).

1.5.2. Derivation of the Formula Describing the Decay Curve

The derivation is based on Lambert-Beer's law

$$I(t) = I_0 \cdot e^{-\sigma \bullet N \bullet L} \qquad [3]$$

which describes the reduction in light intensity for a path length L by an absorbing substance with an absorption cross section σ [cm^2] and a concentration of N molecules per cm^3 [cm^{-3}].

In the case of an empty cavity the intensity within the cavity will decrease exponentially according to

$$I(t) = I_0 \cdot e^{\left[-\left(\frac{\text{number of reflections}}{\text{round trip}}\right)\bullet\left(\frac{\text{loss}}{\text{reflection}}\right)\bullet(\text{number of round trips})\right]}$$

$$I(t) = I_0 \cdot e^{\left[-\quad (2) \quad \bullet \quad (1-R) \quad \bullet \quad \left(\frac{t \bullet c}{2 \bullet L}\right)\right]}$$

$$I(t) = I_0 \cdot e^{\left[-(1-R)\bullet\left(\frac{t \bullet c}{L}\right)\right]} \qquad [4]$$

Considering a cavity that contains a species that absorbs at the wavelength of the radiation injected into the cavity the loss due to absorption will be

$$I(t) = I_0 \cdot e^{\left[-(1-R)\bullet\left(\frac{t \bullet c}{L}\right)+\left(\frac{\text{absorption loss}}{\text{round trip}}\right)\bullet(\text{number of round trips})\right]}$$

$$I(t) = I_0 \cdot e^{\left[-(1-R)\bullet\left(\frac{t \bullet c}{L}\right)+(2 \bullet \sigma_i(\lambda) \bullet N_i \bullet L)\bullet\left(\frac{t \bullet c}{2 \bullet L}\right)\right]} \qquad [5]$$

The total loss in the cavity containing n absorbing species is given by

$$I(t,\lambda) = I_0 \cdot e^{\left\{\left[-(1-R)+\sum_{i=1}^{n}\sigma_i(\lambda) \bullet N_i \bullet L\right]\bullet\frac{c \bullet t}{L}\right\}} \qquad [6]$$

$$I(t) = I_0 \cdot e^{\frac{-t}{\tau}} \qquad [7]$$

One should notice that the determination of the time constant τ from the measurements leads to the determination of the extinction coefficient $\alpha = \sigma_i(\lambda) \cdot N_i$ of the absorbing species. Hence the concentration N_i of the species could be retrieved giving the absorption cross-section of the absorbing species. Busch and Busch (1999).

1.5.3. Errors and Shortcomings in CRDS

In theory, the only limiting noise source is the statistical fluctuation, commonly referred to as the shot noise of the photon stream exiting the cavity and, indeed, the detection limit easily reaches the ppt range if only the intrinsic variables of the method are considered. However, the effective detection limit lies higher due to the inherent factors of monitoring devices. The main sources of deviation are: the laser beam quality, the optical alignment, the thermal and mechanical stabilities, unknown absorbing species, aerosol and Rayleigh scattering, and mirror contamination. Reference values for the absorption cross sections in the case of intrinsic calibration might be inaccurate *or* errors in the gas mixing procedure occur when a calibration procedure is applied. In the latter case, additional matrix effects by bath gas molecules can be evident. Furthermore, photochemical and photophysical processes can cause complications for some analytes and/or wavelength ranges (NO_2!). Considering these perturbations, the CRDS method is still sensitive, especially if the monitoring method includes a calibration procedure. In this way, errors introduced by the evaluation procedure can be minimised, especially when ambient air is used in order to dilute reference gas to proper mixing ratios.

A common noise source particularly in systems employing pulsed lasers is caused by excitation of multiple cavity modes (Spence et al., 2000). The broad linewidth of pulsed lasers typically overlaps with many longitudinal and transverse modes of the ringdown cavity and an excitation of multiple cavity modes leads to mode beating within the ringdown cavity imposing noise on the detected ringdown waveform (Hodges et al., 1996). Very short cavities can eliminate this mode beating as their free spectral range exceeds the laser linewidth (see chapter **1.7.**), however, this happens to the debit of sensitivity. Another option to suppress multimode excitation is the introduction of a spatial filter in form of a telescope.

A technique in order to avoid noise imposed on ringdown decay signals by analogue-to-digital converter was introduced by Spence et al. (2000) employing an analogue detection scheme. Furthermore, the system allows full realisation of very fast repetition rates especially afforded by CRDS instruments using cw lasers. However, shot noise is the limiting factor only in the case of very low laser fluence (Scherer et al., 1997).

The precision of the 12-bit-A/D converter applied in the set-up of this thesis is 1/4096 (or 0.02%) and, hence, completely sufficient regarding other sources of noise. On the other hand, for short ringdown times or intensities reaching the detector too low to follow for more than 1 τ, the sampling rate of the transient recorder (20 MHz) might not be large enough (Busch and Busch, 1999).

1.5.4. Sensitivity of CRDS

Sensitivity in cavity ringdown experiments is best reported in terms of the minimum detectable fractional absorption per pass $\delta I = (I_0 - I)/I_0$ through the cavity. For a single pass, Lambert-Beer's law gives the absorption as

$$I \;=\; I_0 \cdot \exp\{\alpha \cdot L\} \qquad [8]$$

with I = intensity, I_0 = initial intensity, α = absorption coefficient, L = cavity length

For very small absorbances in a single pass ($\alpha \cdot L << 1$), we can approximate

$$\delta I = \frac{I_0 - I}{I_0} \approx \alpha \cdot L \qquad [9]$$

In terms of the change in decay time τ of the ringdown signal this equation can be written as

$$\delta I = \left(\frac{1}{\tau_1} - \frac{1}{\tau_2}\right) \cdot \frac{L}{c} \qquad [10]$$

Zalicki and Zare (1995) showed that for a change in the ringdown time $\Delta\tau = \tau_2 - \tau_1$ upon tuning to an absorption feature, the corresponding absorbance per pass is

$$\alpha \cdot L = (1 - R) \cdot \frac{\Delta\tau}{\tau_1} \qquad [11]$$

Hence, the minimum detectable fractional absorption per pass (or absorbance per pass) can be written as

$$\delta I_{\min} \approx (1 - R) \cdot \frac{\Delta\tau_{\min}}{\tau} = (1 - R) \cdot \frac{\Delta N_{\min}}{N} \qquad [12]$$

where $\Delta\tau_{min}$ is the minimum detectable change in ringdown time on absorption (i.e. the precision of $\Delta\tau$). The equation is also written in terms of the number of round trips in the cavity, N, and the accuracy to which this number can be measured, ΔN_{min}. If we suppose a 0.5 m cavity bounded by mirrors of reflectivity R = 0.9995 and a ringdown time of 15 µs (this is about 3 times the 1/e ringdown time $L/c \cdot |\ln R|$ for empty cavities (derivated from eq. [7]), however, experiments according to **Fig. 2.14.** have revealed the evaluability of this fit range) we get a minimum detectable change in the ringdown time of 3.3 ns. This corresponds to measuring the number of round trips of the light pulse (which is ca. 4500. Calculation according to: pathlength = 15µs·*c* = 4500m, N = 2·L·4500m = 4500, $\Delta\tau_{\min}$= 15µs/4500 = 3.3ns) to an accuracy of within one round trip (i.e. $\Delta\tau_{\min}$= 3.3ns, or $\Delta N_{\min}$= 1). Then, the minimum fractional absorption per pass is $\delta I_{\min}$= 1.1·10^{-7}, or 0.1 ppm. In terms of a minimum absorption coefficient this corresponds to $\alpha_{\min}$= 2.2·10^{-9} cm^{-1} for L = 0.5 m. This calculation is based on Wheeler et al. (1998) with values adapted for the set-up under consideration, however, it should be mentioned that Busch and Busch (1999) obtained a minimum detectable absorption which was worse by more than one order of magnitude using a more statistical approach.

Regarding this approach which neglects effects stated in the last section **1.5.3.**, the major limitation of sensitivity in CRDS is determined by the mirror reflectivity. The cavity length has an additional significant influence on sensitivity preferring long mirror distances. Hence, Wheeler et al. (1998) calculated $\delta I_{\min}$= 20 ppb and $\alpha_{\min}$= 2·10^{-10}cm^{-1}, respectively, for R = 0.9999 and L = 1 m assuming the 1/e ringdown time for empty cavities (≈30 µs).

1.6. Nonlinear Optics

1.6.1. Introduction

Applying laser absorption spectroscopy for traces monitoring, a tunable laser source is an efficient tool. Moreover, the measurement of the absorption spectrum of several species and this on a broad spectral range is necessary in order to overcome the possible spectral interference. Several lasers can be applied for this purpose, however, solid state based laser sources seem to be the more appropriate system in regard to field measurements.

Optical parametric oscillators (OPOs) are powerful sources of widely tuneable coherent radiation, which can be pumped by harmonics of solid state lasers. Beta-bariumborate (BBO, β-BaB_2O_4) has been established as an excellent choice for parametric conversion in the UV, visible, and near-infrared due to its ability to phase match in the UV, in addition to having a broad transmission range, a high damage threshold, and a high nonlinearity. The introduction of BBO-OPOs and the optimisation of their properties can be comprehended in the publications by Cheng et al. (1988), Bosenberg et al. (1989, 1990), Haub et al. (1991), and Borsutzky (1997). Further nonlinear crystals used for parametric oscillators are amongst others LBO (Lithium Triborate), KTP (Potassium Titanyl Phosphate), KTA (Potassium Titanyl Arsenate), $LiNbO_3$ (Lithium Niobate), and PPLN (periodically poled lithium niobate) (Koechner, 1999). A survey of new developments on the field of the different OPO-types and their spectroscopic applications is given by Baxter et al. (2000).

Both the functionality of an OPO and the production of the higher harmonics of a solid state laser can be described by means of nonlinear optics:

1.6.2. Second and Higher Harmonic Generation

The electromagnetic field of a light wave propagating through a medium exerts forces on the outer, loosely bound, valence electrons. In the case of traditional light sources (classical linear optics) and weak radiation or low electric fields E the resulting induced dielectric polarization P is parallel and linearly related to the applied electric field. This can be expressed by the following linear equation:

$$P = \varepsilon_0 \cdot \chi \cdot E \qquad [1]$$

where χ is the dielectric susceptibility (dimensionless) and ε_0 the dielectric constant.

With the very high electric fields involved in laser beams the electric polarization P reaches the domain of saturation resulting in a nonlinear relation in the equation [1] above. In an isotropic medium with coinciding directions of P and E the polarization can be represented as a power series:

$$P = \varepsilon_0 \cdot (\chi \cdot E + \chi_2 \cdot E^2 + \chi_3 \cdot E^3 + ...) \qquad [2]$$

As $\chi >> \chi_2 >> \chi_3 >> \dots$ the contribution of the nonlinear terms χ_2, χ_3, … can be observed for very strong electric fields only. For a light wave

$$E = E_0 \cdot \sin \omega t \qquad [3]$$

hitting the medium, the dielectric polarization is

$$P = \varepsilon_0 \chi E_0 \sin \omega t + \varepsilon_0 \chi_2 E_0{}^2 \sin^2 \omega t + \varepsilon_0 \chi_3 E_0{}^3 \sin^3 \omega t + ... \quad \text{or}$$

$$P = \varepsilon_0 \chi E_0 \sin \omega t + \underbrace{\frac{1}{2} \varepsilon_0 \chi_2 E_0{}^2 (1 - \cos 2\omega t)}_{\textbf{\textit{2}}^{\textbf{\textit{nd}}}\textbf{\textit{ harmonic}}} + \underbrace{\frac{1}{4} \varepsilon_0 \chi_3 E_0{}^3 (3 \sin \omega t - \sin 3\omega t)}_{\textbf{\textit{3}}^{\textbf{\textit{rd}}}\textbf{\textit{ harmonic}}} + ... \qquad [4]$$

The $\cos 2\omega t$ –term corresponds to an oscillation of the dielectric polarization with a frequency twice the frequency of the incident wave. Likewise the reemitted light of this enforced oscillation has an angular frequency 2ω, the process is called “Second Harmonic Generation” (SHG). Visualising the SHG process in terms of photons rather than fields, two identical photons of an energy ħω disappear and fuse to a single photon of an energy ħ2ω. As the differently directed field components of a crystal influence the dielectric polarisation in various directions, for a complete description the variables P and E actually should be related by a susceptibility tensor rather than by a scalar.

The immitted wave propagating through the crystal continuously generates contributions to the second harmonic which can only be constructively superimposed for proper phase matching conditions. The problem is that due to dispersion the phase velocity of the incoming wave differs from the phase velocity of the second harmonic. The phase matching condition is satisfied for $n_{\omega} = n_{2\omega}$. This can be managed by a definite angular adjustment of the crystal in reference to the optic axis. (Svelto, 1989; Davis, 1996; Hecht, 1999; Koechner, 1999; Eichler and Eichler, 2001).

1.6.3. General Functionality of an Optical Parametric Oscillator (OPO)

An Optical Parametric Oscillator (OPO) consists of a nonlinear crystal in which the strong incident wave of the frequency ω_p (pump frequency) is superimposed by the weak signal wave to be amplified and of lower frequency ω_s. Generally, for the superimposition of two light waves we can write:

$$E = E_{01} \cdot \sin \omega_1 t + E_{02} \cdot \sin \omega_2 t \qquad [5]$$

Inserted in the expression for P (eq. [4]) the contribution of the second order is:

$$\varepsilon_0 \chi_2 \cdot (E_{01}{}^2 \sin^2 \omega_1 t + E_{02}{}^2 \sin^2 \omega_2 t + 2 \cdot E_{01} E_{02} \sin \omega_1 t \cdot \sin \omega_2 t) \qquad [6]$$

The first two terms can be expressed as a function of $2\omega_1$ and $2\omega_2$, respectively, while the third term is caused by the sum and difference terms $\omega_1 + \omega_2$ and $\omega_1 - \omega_2$, respectively ($\sin \omega_1 t \sin \omega_2 t = ½ [\cos (\omega_1 t - \omega_2 t) - \cos (\omega_1 t + \omega_2 t)]$). While in the case of the sum term energy and momentum are transported away by a newly produced photon, in the case of the difference term the conservation of energy and momentum necessitates that in the course of the interaction only the higher frequency ω_1-photon disappears and two new photons are generated, a ω_2-photon as well as an additional "difference-photon". Hence, in the case of the OPO the pump wave is transformed into a signal wave as well as into a difference wave of the frequency $\omega_i = \omega_p - \omega_s$, the so-called idler wave. From the superposition of idler and pump wave additional contributions to idler and signal will result. In this way signal and idler wave are amplified. By changing the refractive index of the crystal the oscillator will become tunable (Hecht, 1999; Koechner 1999). A schematic illustration of the production of a signal and an idler wave by a pump wave is shown in **Fig. 1.8.**. Furthermore, the phase matching condition is depicted in this figure (Schiller and Schmidt, 2002).

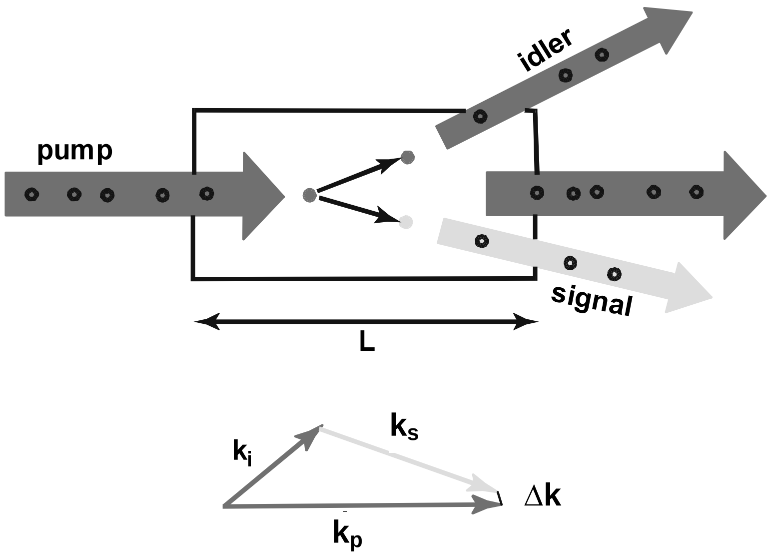

Fig. 1.8. Production of a signal and an idler wave by a pump wave in an OPO crystal. The wave vectors of the produced photons approximately fulfil the phase matching condition $\Delta k = k_p - k_s - k_i = 0$. This condition determines the wave propagation of signal and idler. Adapted from Schiller and Schmidt (2002).

An optical uniaxial crystal has different refractive indexes for light polarised perpendicular (ordinary, o) and parallel (extraordinary, e) to the main intersection. For phase matching the fundamental wave and the second harmonic have to be o or e polarised, respectively, with different refractive indexes n_{lo} and n_e. While n_{lo} is independent from the incident angle θ relative to the optic axis, $n_e(\theta)$ is strongly angle dependent. By proper choice of the direction of θ it is possible to match both refractive indexes (Eichler and Eichler, 2001).

1.6.4. OPO Based Laser System for CRDS

The pulsed optical parametric oscillators (OPOs) applied for the CRD spectroscopic analysis in this thesis are generating widely tunable coherent radiation. They consist of β-barium borate (BBO) which is pumped by the third harmonic of a Q-switched Nd:YAG laser (355 nm) and they emit tunable radiation in the visible (400 – 710 nm) and near infrared (710 – 2500 nm) range. This wide tuning range can be extended into the UV to wavelengths as short as 205 nm by frequency doubling. This is done by second harmonic generation (SHG) of the visible OPO output in a second BBO crystal.

The nonlinear material BBO allows both type-I ($e \rightarrow o + o$) and type-II ($e \rightarrow o + e$) phase matching, meaning that both the OPO signal and idler wave are o-polarized in the case of type-I phase matching. Anstett et al. (2001) showed that type-II phase matching in combination with double-passing the pump radiation improves the conversion efficiency, reduces the spectral bandwidth and lowers the divergence of the OPO waves simultaneously. Thus, this set-up is optimal for the application in this work.

Three sets of mirrors, coated for the red, green and blue spectral ranges, can be used to ensure optimum reflectivity and, thus, high conversion efficiencies in the whole tuning range. The mirror set consists of an input coupling mirror which is highly reflective for the signal wavelength and an output coupling mirror with a reflectivity of about 70%. All OPO mirrors are transparent for the idler and pump wavelengths. First the reflection of the laser pump radiation back into the OPO was accomplished by an external mirror, which was highly reflective for the pump wavelength but transparent for the OPO wavelengths. However, in this way the divergence of the OPO output beam could be reduced in the phase matching plane only. To also reduce the divergence in the vertical plane, the HR mirror of the OPO was replaced by a 90° prism which is aligned as a retro-reflector with an angle of 45° between the apex and the phase matching plane (**Fig. 1.9.**). The reflection in the prism exchanges the OPO beam components in the vertical and horizontal plane in each cavity round trip. This results in a reduction of the OPO divergence in both directions. Depending on the refractive index of the prism material, there is a certain rotation of the polarisation of the signal wave after reflection in the prism. To ensure high conversion efficiencies, this rotation is compensated by an additional half-wave plate in an appropriate angular position. The pump wave is coupled into the cavity by a 45° HR mirror which is transparent for the OPO wavelengths.

With this set-up the divergence of the OPO signal beam can be reduced to 1.6 mrad in both directions while maintaining a narrow OPO bandwidth of less than 0.1 nm. Doubling efficiencies of up to 35% can be achieved. Anstett et al.(2001).

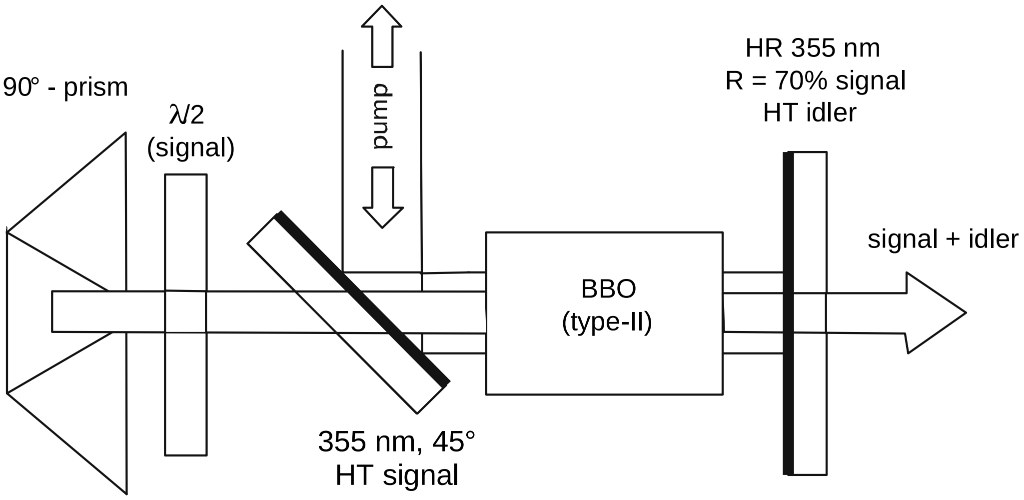

Fig. 1.9. Experimental set-up of a type-II phase matched BBO-OPO with a retro-prism which is aligned as a retro-reflector. The half-wave plate compensates changes in direction of the polarisation of the signal wave (Anstett et al., 2001)

The linewidth diagram in **Fig. 1.10.** shows the OPO laser linewidth of the applied VisIR2 in dependence of the wavelength in comparison to a conventional broadband OPO. The linewidth is clearly improved, especially near the degeneracy at 709.4 nm (which is twice the third harmonic of the Nd:YAG laser) and shows values around 6 cm^{-1}.

The extended spectral range into the UV after second harmonic generation with a second BBO crystal is depicted in **Fig. 1.11.**. In the diagram the SHG pulse energy is plotted against the wavelength emitted by the OPO.

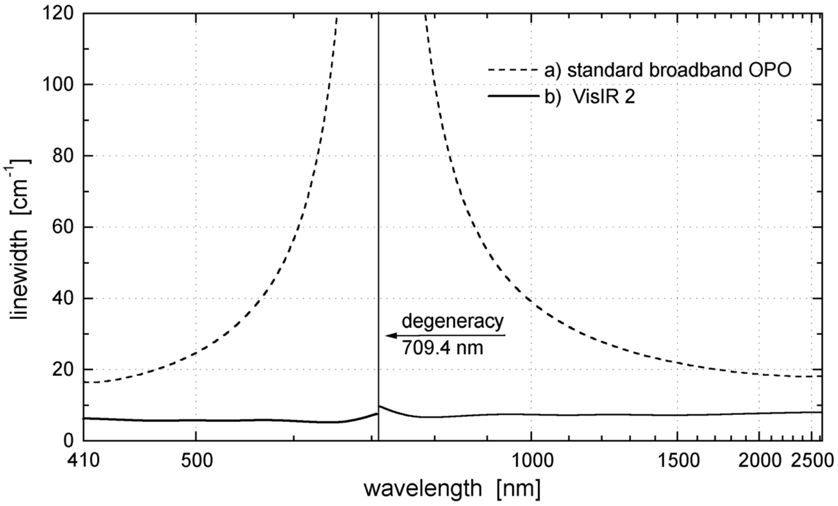

Fig. 1.10. Linewidth of the OPO-Laser. a) standard values of a tunable OPO. b) recently developed laser source VisIR2 which was applied in this work. Göritz (2000).

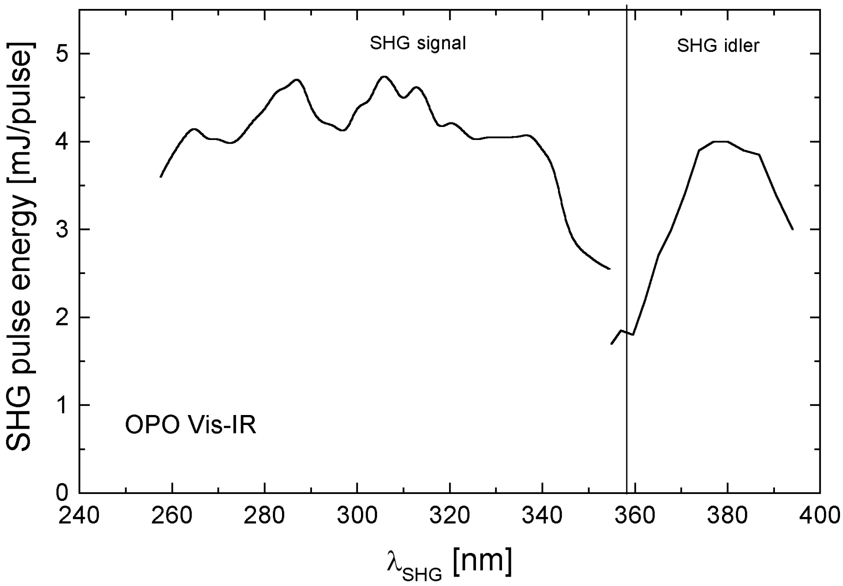

Fig. 1.11. Spectral range of the emission of the VisIR-OPO in the UV and visible after second harmonic generation (frequency doubling). Göritz (2000).

1.7. Comparison with CRDS Applying CW-Lasers

Although the experiments presented in this thesis refer to CRDS applying pulsed laser sources, a short review of CRDS with continuous wave (cw) light sources will be added. Some shortcomings of the pulsed method are a data acquisition rate, which is limited by the repetition frequency of the laser, a restricted spectral bandwidth, and the size of the laser system. However, pulsed lasers have the great advantage that radiation can be produced over a very wide wavelength range, which extents into the UV-spectral region.

The Lorentzian longitudinal cavity modes and the frequency spacing of these cavity modes is shown in **Fig. 1.12.**.

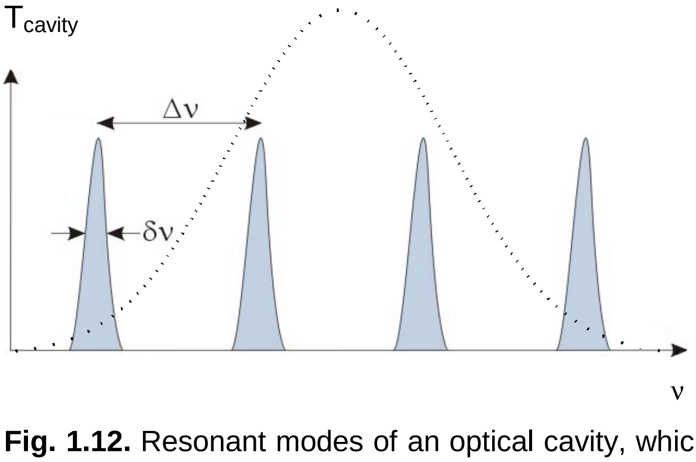

Fig. 1.12. Resonant modes of an optical cavity, which are superimposed by a laser pulse (pointed line).

The frequency interval between two longitudinal modes, the Free Spectral Range (FSR), can be written as:

$$\Delta\nu = \frac{c}{2 \cdot L} \qquad [1]$$

c: speed of light, L: cavity length

Thus, for the 0.5 m cavity used in the experiments in the course of this thesis, the longitudinal mode spacing for the TEM_{00} mode is 300 MHz (0.01 cm^{-1}).

As indicated in **Fig. 1.12.**, the linewidth of a pulsed laser usually spans several cavity modes (this is especially true if additional to longitudinal modes higher transverse modes are excited). Consequently, in this case no frequency matching is necessary. However, conditions are different when a cw laser with narrow linewidth in the 20 – 100 MHz range (≈ 0.001 – 0.003 cm^{-1}, ≈ 10^{-4} nm) is applied, which is in the spectral range of the cavity modes and the FSR. Because the power of narrow cw laser is low, it is necessary to match the resonant cavity mode TEM_{00}, which lead to higher cavity transmission. It requires careful frequency matching (He et al., 1998). In other words, when using narrow band cw lasers for CRDS, the cavity will have to be frequency locked to the laser by tuning the laser to one of the cavity resonances (or *vice versa*). A strong ringdown signal may then be observed after the laser beam is quickly interrupted (Romanini et al., 1997). The commonly used approach is to actively adjust the length of the cavity such as to match the frequency of one of the longitudinal modes of the high finesse cavity to the laser frequency. This can be performed, using a piezoelectric transducer slowly scanning the cavity length. For this purpose Romanini et al. (1997) introduced an active cavity tracking circuit while He et al. (1998) matched the cavity by periodically wobbling its length.

In another approach the radiation from a scanning narrow band cw laser is coupled into the cavity via the accidental coincidences of the laser frequency with the frequency of one of the multitude of the cavity modes (Engeln et al., 1998). This technique was successfully tested with a laser diode (λ = 680nm; EOSI) for the set-up described in the experimental section by replacing the OPO-system. While the laser was scanned by a piezo over a range of ±50 GHz (≈ 3 cm^{-1}, 0.14 nm), different cavity modes were excited.

A shortcoming of CW CRDS is the limited scanning range of the diode module usually spanning circa 20 nm (OPO: 1-2 μm). As the spectral range of laser diodes covers near infrared and infrared (OPO: UV to Vis), CW CRDS and pulsed CRDS complement each other concerning this point of view. Concluding, it can be stated that the cw technique is especially suitable for high-resolution measurements in a restricted wavelength range and for measurements in the IR.

1.8. Simulations on Optical Cavities

The optical cavity applied in CRDS (**Fig 1.7.**, **Fig. 2.3.**) has to be well designed for absorption measurements in order to reach high sensitivity range. The laser beam has to cover a very long distance within the cavity and, therefore, it has to be kept stable within this cavity. Hence, a simulation has been developed, which allows determining fundamental parameters and failure criteria for the considered functions of the optical cavity. In addition, it is essential that the coupling of the laser beam with the optical cavity reaches an optimum. The parameters for this coupling are determined by another simulation, which is likewise performed with LabVIEW software.

1.8.1. Stability of Optical Cavities

For a generalised optical system, as shown in **Fig.1.13.** (Busch et al., 1999), a ray will be characterised by its displacement *r(z)* from the optical z-axis and its slope, given by *tan* $\alpha(z)$, where

$$\tan\alpha(z) = \frac{dr}{dz} \approx \alpha(z) \qquad [1]$$

as the deviations from the optical axis are small (paraxial approximation).

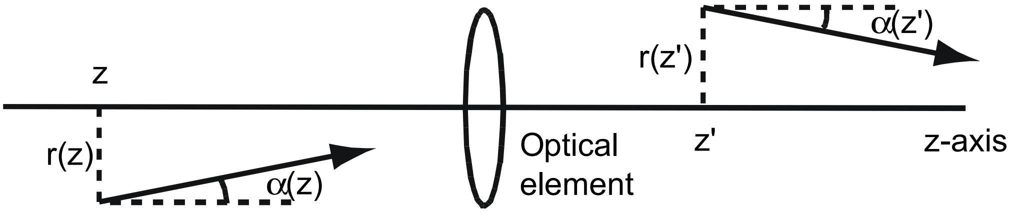

Fig. 1.13. Generalised optical system.

After passing through an optical system, the ray will be characterised by a new set of parameters, which are related to the original parameters by the following matrix transformation (Svelto 1989, Busch et al., 1999; Meschede, 1999):

$$\begin{bmatrix} r(z') \\ \alpha(z') \end{bmatrix} = \begin{bmatrix} A & B \\ C & D \end{bmatrix} \bullet \begin{bmatrix} r(z) \\ \alpha(z) \end{bmatrix} \tag{2}$$

For a ray propagation through a homogeneous medium over a distance *d* the new parameters are (**Fig. 1.14.**):

$$\begin{aligned} r(z') &= r(z) + \alpha(z) \cdot d \\ \alpha(z') &= \alpha(z) \end{aligned} \tag{3}$$

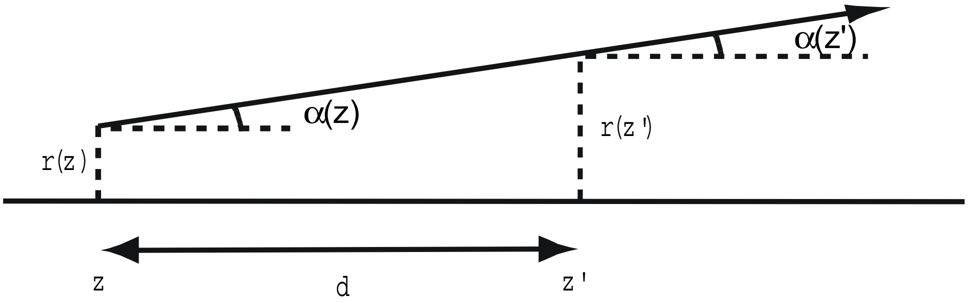

Fig. 1.14. Ray propagating through a homogeneous medium.

In terms of matrix notation equations [2] and [3] can be represented by:

$$\begin{bmatrix} r(z') \\ \alpha(z') \end{bmatrix} = \begin{bmatrix} 1 & d \\ 0 & 1 \end{bmatrix} \bullet \begin{bmatrix} r(z) \\ \alpha(z) \end{bmatrix} \tag{4}$$

For a spherical concave mirror the ray transfer matrix is given by (Svelto, 1989):

$$\begin{bmatrix} A & B \\ C & D \end{bmatrix} = \begin{bmatrix} 1 & 0 \\ -\frac{2}{R} & 1 \end{bmatrix} \tag{5}$$

where *R* is the radius of curvature of the mirror.

For a given optical resonator composed by two spherical mirrors with the radii of curvature R_1 and R_2 separated by a distance L, a ray starts at the entry mirror (R_1), propagates through a distance L, is reflected by the exit mirror (R_2), returns through a distance L, and is reflected by the entry mirror (R_1). As the matrix corresponding to several optical transformations is the product of the individual matrices for the optical system taken in reverse order to the propagation, the ray matrix corresponding to a round-trip in the cavity can be represented by:

$$\begin{bmatrix} A & B \\ C & D \end{bmatrix} = \begin{bmatrix} 1 & 0 \\ -\frac{2}{R_1} & 1 \end{bmatrix} \bullet \begin{bmatrix} 1 & L \\ 0 & 1 \end{bmatrix} \bullet \begin{bmatrix} 1 & 0 \\ -\frac{2}{R_2} & 1 \end{bmatrix} \bullet \begin{bmatrix} 1 & L \\ 0 & 1 \end{bmatrix} \tag{6}$$

$$\begin{bmatrix} A & B \\ C & D \end{bmatrix} = \begin{bmatrix} 1-\frac{2L}{R_2} & 2L-\frac{2L^2}{R_2} \\ \frac{4L}{R_1R_2}-\frac{2}{R_1}-\frac{2}{R_2} & 1-\frac{2L}{R_2}-\frac{4L}{R_1}+\frac{4L^2}{R_1R_2} \end{bmatrix} = M$$

This ray matrix *M* corresponds to one round trip through the cavity, however the aim of this analysis is the behaviour of the ray for n roundtrips. We search cavity (and beam) parameters, which keep the cavity stable, i.e. it must be able to trap rays so that they are unable to escape after multiple reflections. For the (n+1)th round-trip we obtain:

$$\begin{bmatrix} r_{n+1} \\ \alpha_{n+1} \end{bmatrix} = M \bullet \begin{bmatrix} r_n \\ \alpha_n \end{bmatrix} \qquad [7]$$

As it must be avoided that the ray misses one of the mirrors and escapes off the cavity, the displacement r_n must never exceed the mirror radius. The positions of the ray on the cavity mirror after the n^{th} round-trip are depicted in **Fig 1.15.** (page 41) for different beam and cavity parameters.

Another aspect are the different refractive indices for the mirrors and the ambient air. While entering the cavity, the initial beam parameters r_0 and α_0 are changed by two transitions air→mirror and mirror→air and, furthermore, the differing refractive index for the passage through the mirror must be taken into account. Thus, the initial beam parameters (r_0; α_0) have to be multiplied by the following matrices:

$$\begin{bmatrix} r \\ \alpha \end{bmatrix} = \begin{bmatrix} 1 & 0 \\ -\frac{1}{R_1} \cdot \frac{n_{air} - n_{mirror}}{n_{air}} & \frac{n_{mirror}}{n_{air}} \end{bmatrix} \bullet \begin{bmatrix} 1 & \frac{d_1}{n_{mirror}} \\ 0 & 1 \end{bmatrix} \bullet \begin{bmatrix} 1 & 0 \\ 0 & \frac{n_{air}}{n_{mirror}} \end{bmatrix} \bullet \begin{bmatrix} r_0 \\ \alpha_0 \end{bmatrix} \qquad [8]$$

The three matrices describe (with n_{air} and n_{mirror} as the refractive indexes of air and the mirrors and d_1 as the thickness of the left mirror):

$$\begin{bmatrix} r \\ \alpha \end{bmatrix} = \begin{bmatrix} \text{spherical dielectric} \\ \text{interface} \end{bmatrix} \bullet \begin{bmatrix} \text{free space propagation} \\ \text{within the mirror} \end{bmatrix} \bullet \begin{bmatrix} \text{plane interface bet-} \\ \text{ween 2 dielectrics} \end{bmatrix} \bullet \begin{bmatrix} r_0 \\ \alpha_0 \end{bmatrix} \qquad [9]$$

for $n_{air} = 1$, eq. [8] simplifies to:

$$\begin{bmatrix} r \\ \alpha \end{bmatrix} = \begin{bmatrix} 1 & 0 \\ \frac{n_{mirror} - 1}{R_1} & n_{mirror} \end{bmatrix} \bullet \begin{bmatrix} 1 & \frac{d_1}{n_{mirror}} \\ 0 & 1 \end{bmatrix} \bullet \begin{bmatrix} 1 & 0 \\ 0 & \frac{1}{n_{mirror}} \end{bmatrix} \bullet \begin{bmatrix} r_0 \\ \alpha_0 \end{bmatrix} \qquad [10]$$

Eq. [10] has to be applied only once (for the entrance of the laser pulse into the cavity) unlike to eqs. [6]-[7], which have to be applied n times for n roundtrips.

The simulation was performed by a LabVIEW program resulting in graphics similar to **Fig 1.15.** (page 41). In these figures different parameters are varied: beam divergence (**Fig.**

1.15.a), mirror distance (**Fig. 1.15.b**), and mirror radius (**Fig. 1.15.c**). The ray which is reflected back and forth between the mirrors must not miss the mirrors, that means its position must not exceed the mirror edge indicated by horizontal lines in **Fig. 1.15.**. For instance, unfavourable conditions occur in the case of large beam divergencies (**Fig. 1.15.a**) or long mirror distances (**Fig. 1.15.b**).

1.8.2. Coupling Laser-Cavity

In order to exclusively excite the TEM_{00} modes of the cavity a connection between the incident beam and the fundamental Gaussian beam of the cavity has to be established. This accordance implies that the two beams must have the same transverse section on the inner surface of the entry mirror as well as a radius of equal curvature. A single lens can suffice to realise the accordance. The adjustment parameters to be determined are the distance lens – laser source (d_1) and the distance cavity – lens (d_2) (**Fig. 1.16.**). The formalism of the Gaussian beam in order to know the complex Gaussian parameters (or the complex curvature radius) as well as the matrices ABCD will be applied. The distances d_1 and d_2 will be determined by equalising the Gaussian parameter of the incident beam propagating towards the cavity (+z) with the Gaussian parameter leaving from the cavity towards the laser source (-z) on the internal side of the entry mirror.

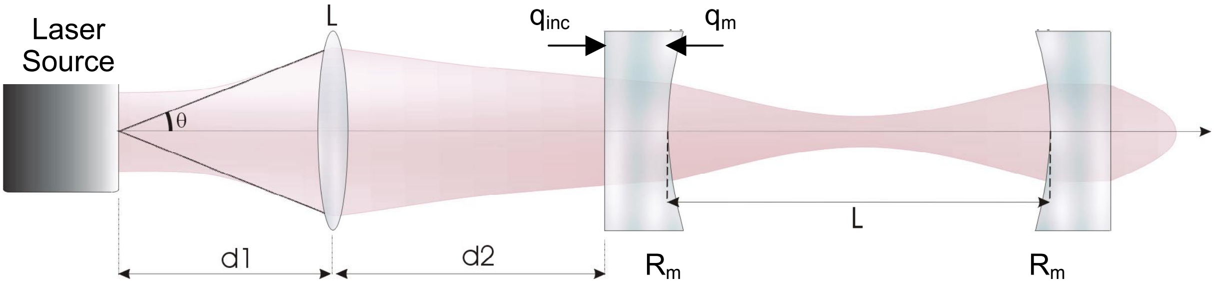

Fig. 1.16. Coupling cavity – laser. Motto-Ros (2002).

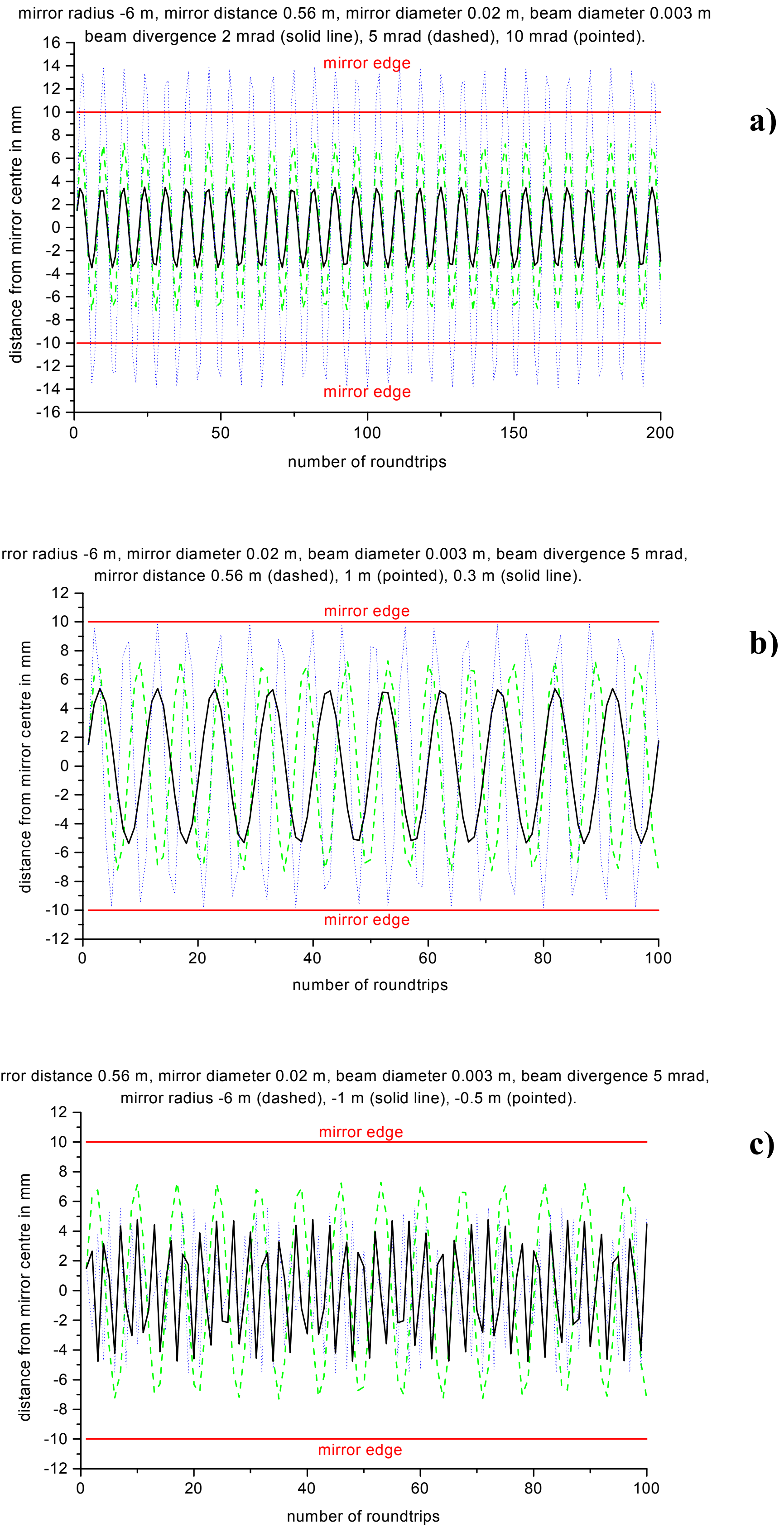

Fig. 1.14. Simulation for varying beam divergence (**a**), mirror distance (**b**), and mirror radius (**c**). The horizontal lines “mirror edge” indicate the stability boundaries.

The transverse dimension ω_m of the TEM_{00} mode on the surface of the entry mirror is given by (Svelto, 1989; Davis, 1996, Morville, 2001):

$$\omega_m = \left(\frac{\lambda \cdot L}{2\cdot\pi}\right)^{\frac{1}{2}} \cdot \left(\frac{2\cdot R_m^{\;2}}{L\cdot\left(R_m - \frac{L}{2}\right)}\right)^{\frac{1}{4}} \qquad [11]$$

ω_m= beam section on inner surface of entry mirror, R_m = radius of beam and entry mirror, λ = beam wavelength, L = cavity length.

It can be seen that the beam can be entirely described by its section ω and its radius R which should be equivalent to R_m at the surface of the entry mirror. The complex Gaussian parameter q_m of the TEM_{00} mode in this spot is given by:

$$\frac{1}{q_m} = \frac{1}{-R_m} - i\frac{\lambda}{\pi\cdot\omega_m^{\;2}} \qquad [12]$$

The transfer matrix of the entry mirror linking the incident parameter q_{inc} to the parameter q_m on the inner side of the mirror can be written as:

$$\begin{bmatrix} A & B \\ C & D \end{bmatrix} = \begin{bmatrix} 1 & 0 \\ \frac{1}{2\cdot R_m} & n \end{bmatrix} \cdot \begin{bmatrix} 1 & d \\ 0 & 1 \end{bmatrix} \cdot \begin{bmatrix} 1 & 0 \\ 0 & \frac{1}{n} \end{bmatrix} = \begin{bmatrix} 1 & \frac{d}{n} \\ \frac{1}{2\cdot R_m} & \frac{d}{2\cdot R_m}+1 \end{bmatrix} \qquad [13]$$

n = refractive index of the mirror, d = mirror thickness

The parameter q_{inc} can be deduced from the relation:

$$q_{inc} = \frac{B - D\cdot q_m}{C\cdot q_m - A} \qquad [14]$$

Now q_{inc} has to be linked up with the beam parameter emitted by the laser source q_{laser}. The novel transfer matrix represents the combination of a propagation into the free space d_1 followed by a thin lens of the focal length f and a propagation in the free space d_2, and is written as follows:

$$\begin{bmatrix} A & B \\ C & D \end{bmatrix} = \begin{bmatrix} 1 & d_2 \\ 0 & 1 \end{bmatrix} \cdot \begin{bmatrix} 1 & 0 \\ -\frac{1}{f} & 1 \end{bmatrix} \cdot \begin{bmatrix} 1 & d_1 \\ 0 & 1 \end{bmatrix} = \begin{bmatrix} 1-\frac{d_2}{f} & d_1+d_2-\frac{d_1 \cdot d_2}{f} \\ -\frac{1}{f} & 1-\frac{d_1}{f} \end{bmatrix} \qquad [15]$$

f = focal length of the thin lens, d_1 = distance laser source – lens, d_2 = distance lens - cavity

In this way, a relation between the complex Gaussian parameter q_{laser} at the exit of the laser source and the parameter q_m at the internal side of the mirror can be obtained:

$$q_{inc} = \frac{A \cdot q_{laser} + B}{C \cdot q_{laser} + D} \qquad [16]$$

Considering the focal length of the fixed thin lens, this relation allows to evaluate d_2 as a function of d_1:

$$d_2(d_1) = \frac{q_{inc} \cdot q_{laser} - f \cdot q_{inc} + f \cdot q_{laser} + d_1 \cdot (f + q_{inc})}{q_{laser} - f + d_1} \qquad [17]$$

The parameter q_{laser} can be obtained by experimentally measuring the laser divergence θ and applying the relations:

$$\omega_{laser} = \frac{\lambda}{\pi \cdot \theta} \quad \text{and} \quad q_{laser} = i\frac{\pi \cdot \omega_{laser}{}^2}{\lambda} \qquad [18], [18]$$

θ = laser divergence

As the relation $d_2(d_1)$ is based on complex values, a zero value has to be imposed on the imaginary part of d_2 and a positive value on its real part in order to obtain physical solutions.

Setting $q_{laser} = i\gamma$ and $q_{inc} = \alpha + i\beta$ different values of d_1 can be searched for which $Im(d_2) = 0$. Hence, a second order equation in respect to d_1 has to be calculated:

$$\gamma \cdot f^2 + \gamma^2 \cdot \beta + \beta \cdot (d_1 - f)^2 = 0 \qquad [19]$$

The solutions:

$$d_1 = f \pm \sqrt{\gamma \cdot \left(\frac{f^2}{\beta} - \gamma \right)} \quad \text{with} \quad f^2 > \gamma \cdot \beta \qquad [20]$$

of its two values for d_1 correspond to two values $Re(d_2)$ with the physical solution corresponding to a positive value of $Re(d_2)$.

This coupling proves to be essential as it allows at once to optimise the intensity entering the cavity and to excite exclusively the fundamental mode TEM_{00}.

An optimisation program written in LabVIEW which permits to calculate the ideal positions of the optical elements was developed by Motto-Ros (2002) for cw laser sources. The simulation is based on different optical systems which are a single thin lens, a single thick lens, a telescope, and an association of two thin lenses. Regarding the numerous tests which were realised, the use of a single thin lens seems to be widely sufficient in order to realise a good coupling. However, this program only considers linear cavities with identical mirrors. The different input parameters consist of the wavelength and the divergence of the laser source, the cavity length, the refractive index, and the thickness as well as the radius of the ringdown mirrors. Finally, according to the optical system under consideration, different parameters prove to be necessary: in the case of a single thin lens, its focal length has to be given.

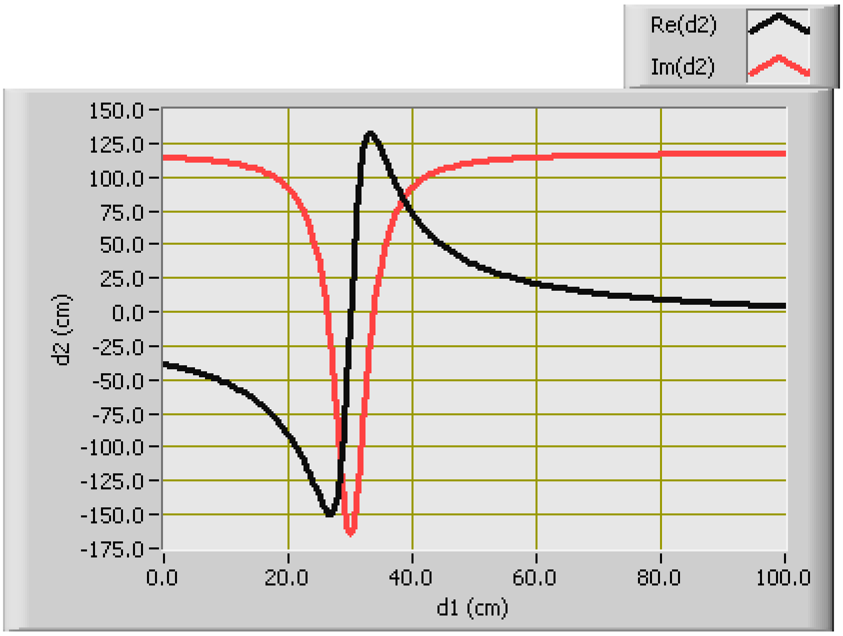

Fig. 1.17. Result of a coupling simulation for the main parameters: wavelength 400 nm, beam divergence 2 mrad, mirror radius 6 m, cavity length 54 cm, **single thin lens** with f = 30 cm.

An example of a simulation performed for typical parameters of NO_2-measurements applying the set-up described in the experimental section is shown in **Fig. 1.17.**. For a laser wavelength of 400 nm, a beam divergence of 2 mrad, a cavity length of 54 cm, and a mirror radius of 6 m, a single thin convex lens with a focal length of 30 cm has to be situated at a distance d_1 = 33.8 cm from the laser output and a distance d_2 = 130.8 cm from the cavity input mirror. However, the results react extremely sensitive to changes in some input parameters: a beam divergence of 3 mrad would extend the total length $\Delta d = d_1 + d_2$ to barely realisable 271 cm (instead of 165 cm), and a divergence of 1.5 mrad would reduce Δd to 94 cm. Replacing the lens by another one with f = 25 cm results in Δd = 110 cm, and f = 20 cm diminishes Δd to 33 cm. Thus, it has to be stated, that an optimum coupling is very difficult to achieve in the case of the set-up applied in this thesis. However, for a modified device, the laser-cavity coupling program described above could be an extremely useful tool and for this reason it was presented in this section.

It should be added, that the simulation reveals no existing solution for the spatial filter applied in the experimental set-up and which consisted of two convex lenses (f = 5 cm, f = 10 cm). However, this spatial filtering is very effective in suppressing undesirable transversal modes (Davis, 1996; Meschede, 1999), an effect which outweighs the non-perfect coupling.

1.9. Traces Concentration Retrieving Procedure

1.9.1. Derivative Spectroscopy

It can be shown in **Fig.1.18.** how two compounds stand out more and more clearly in the derivatives $d^nA/d\lambda^n$ of increasing order of a sum spectrum while they are completely hidden in the non derivated initial spectrum. The components become particularly distinct in the fourth derivation while the peak direction remains the same as in the initial spectrum. As

$$\frac{d^nA}{d\lambda^n} = c \cdot x \cdot \frac{d^n\varepsilon}{d\lambda^n} \quad \text{(Lambert-Beer's law)} \qquad [1]$$

A = absorption, λ = wavelength, c = concentration, x = sample thickness, ε = extinction coefficient

the peak height of the derivated spectra is directly proportional to the concentration. Indeed, with increasing order of the derivative danger is growing of being hoaxed by artefacts like the secondary maxima of the fourth derivation in **Fig.1.18.**. Derivatives of higher order are especially suitable for the analysis of single components in multi component analysis. Furthermore, particularly in the case of the fourth derivative the shift of the peaks is diminished in a sum spectrum of differently broad Gauss curves, an aspect which is shown in **Fig. 1.19.**. Otherwise the maximum of the narrow peak is shifted into the direction of the broader peak. All together, the derivative spectroscopy yields the following advantages (Schmidt, 1994):

- peaks become more narrow banded, the wavelength resolution is increasing.
- flat signals can be suppressed by the proper choice of Δλ. This includes variations in mirror reflectivity, Rayleigh/ Mie-scattering, and aerosol influence.

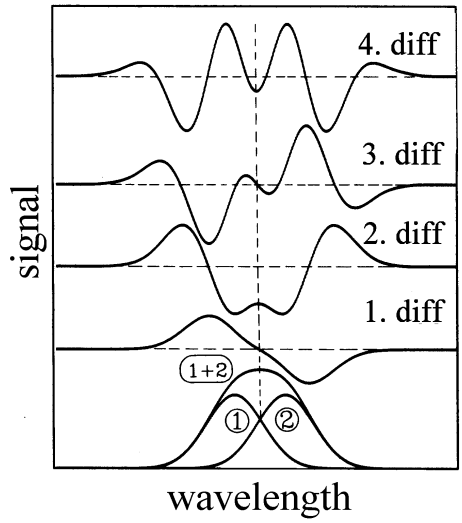

Fig. 1.18. First to fourth derivative of a sum spectrum composed of two identical Gauss curves (adapted from Schmidt, 1994).

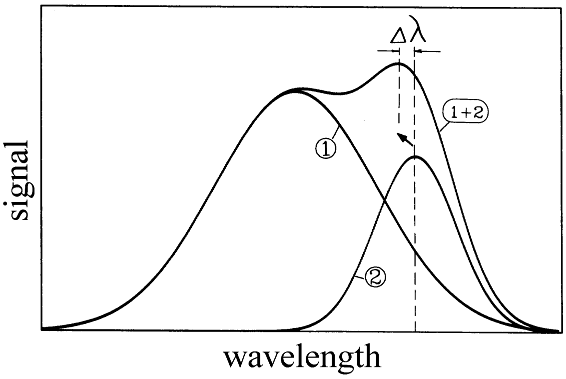

Fig. 1.19. In a sum spectrum (1 + 2) of two differently broad Gauss curves the peak of the narrow component (2) is shifted by Δλ into the direction of the broad peak (1). This shift is reduced for higher derivations. Schmidt (1994).

As can be already seen in the name of the method, derivative spectroscopy is applied in Differential Optical Absorption Spectroscopy (DOAS) (Stutz and Platt, 1996; Geyer, 2000). In this approach the differential reference spectrum for analyte 1 is subtracted from the differential experimental spectrum and the residual is regarded closely. From this residual the reference spectrum for the next analyte 2 is removed in the similar way and the procedure is repeated for more “candidates” until the residuals is pure noise (Schiff, 1992). The principle of the procedure is shown in **Fig. 1.20.**. However, the evaluation technique presented in this thesis for CRDS differs from the DOAS approach as the selected analyte reference spectra are fitted by a multicomponental least square fit to the experimental spectrum.

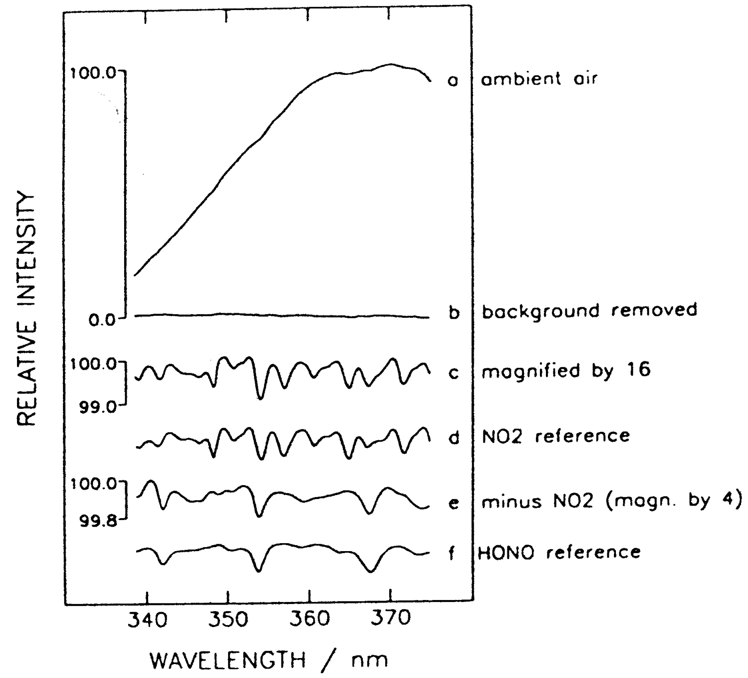

Fig 1.20. Analytical procedure used to determine the concentration of HONO in ambient air by DOAS. a) ambient air spectrum; b) broadband spectrum subtracted; c) same as b) magnified by a factor of 16; d) NO_2 reference spectrum; e) 4 • c) – d); f) HONO reference spectrum. Schiff (1992).

1.9.2. Convolution of the Spectra

The convolution method represents a very suitable procedure for noise reduction and smoothing of the experimental data and spectra (Schmidt, 1994; Hecht, 1999; Jamal and Pichlik, 1999). In this approach a function f(λ) is multiplied by a function g(λ) shifted relatively to the wavelength (x-coordinate) and, subsequently, averaged (integrated) over the whole data range. This can be described mathematically by the convolution integral:

$$h(\lambda) = \int_{x=-\infty}^{+\infty} f(\lambda') \cdot g(\lambda - \lambda') d\lambda' \qquad [2]$$

or $$h(\lambda) = f(\lambda) \otimes g(\lambda) \qquad [3]$$

By convolution of the spectrum with a Gauss curve of suitable width at half maximum height (width σ of a generated Gauss curve at 5/8 maximum height) an excellent smoothing is attained and the noise is suppressed. The Gauss curve simulates the shape and spectral resolution of the laser beam. In most cases σ = 0.2 nm or σ = 0.3 nm is assumed for the width of the Gauss curve.

1.9.3. Multi Compound Analysis

In a sample mixture the concentrations of single components, which do not interact with each other, shall be determined. According to Lambert-Beer's law [1] the total absorption A of a mixture of n components at the wavelength λ_i is:

$$A(\lambda_i) = \sum_{j=1}^{n} \varepsilon_j(\lambda_i) \cdot c_j \qquad [4]$$

In matrix style the sum spectrum can be composed in the following manner:

$$\begin{bmatrix} A(\lambda_1) \\ A(\lambda_2) \\ \cdots \\ A(\lambda_m) \end{bmatrix} = \begin{bmatrix} \varepsilon_1(\lambda_1) & \varepsilon_2(\lambda_1) & \cdots & \varepsilon_n(\lambda_1) \\ \varepsilon_1(\lambda_2) & \varepsilon_2(\lambda_2) & \cdots & \varepsilon_n(\lambda_2) \\ \cdots & \cdots & \cdots & \cdots \\ \varepsilon_1(\lambda_m) & \varepsilon_2(\lambda_m) & \cdots & \varepsilon_n(\lambda_m) \end{bmatrix} \bullet \begin{bmatrix} c_1 & c_2 & \cdots & c_n \end{bmatrix} \qquad [5]$$

With B•X = Y the solution vector X and, therefore, the different concentrations c_1, c_2, … c_n can be computed from the input matrix B ($\rightarrow\varepsilon(\lambda)$) and the known vector Y($\rightarrow A(\lambda)$).

Two component analysis are simple and accurate, errors below 5% are still achievable for three component analysis, while an simultaneous analysis of more than five components makes sense in some particular cases only. Schmidt (1994).

1.9.4. CRDS Evaluation

1.9.4.1. General Evaluation Mode

The time dependent intensity I(t) of a CRDS-signal detected by a PMT behind the exit mirror of the cavity is:

$$I(t) = I_0 \cdot e^{-\left[(1-R)+\alpha \bullet L\right] \bullet \frac{c}{L} \bullet t} \qquad [6]$$

I_0 = initial intensity, R = mirror reflectivity, α = absorption, L = cavity length, c = speed of light.

The measured slope of the CRDS-signal is:

$$slope_{meas} = \left[(1-R)+\alpha \cdot L\right] \cdot \frac{c}{L} \qquad [7]$$

with $$\alpha = \frac{1}{L} \cdot \left[slope \cdot \frac{L}{c} - (1-R)\right] \qquad [8]$$

and $$\alpha = N \cdot \sigma \qquad [9]$$

(N = number of molecules per cm^{-3}, σ = absorption cross section in cm^2)

The number of N, which corresponds to the concentration of a species, can easily be calculated for known absorption cross sections. For the conversion of the concentration into units of ppb or ppm it must be considered that:

1 ppm = $2.46 \cdot 10^{13}$ cm^{-3}
1 ppb = $2.46 \cdot 10^{10}$ cm^{-3}

For a background corrected spectrum, i.e. a sample spectrum after subtraction of a background spectrum, eq. [8] simplifies as, for example, changing mirror reflectivities are already taken into account:

$$\Delta\alpha = \alpha_{sample} - \alpha_{backgd} = N \cdot \sigma \sim \Delta slope_{meas} \qquad [10]$$

Generally, for a known absorption cross section σ (from reference spectra like Merienne et al., 1995; Hitran96, 1996; Trost et al., 1997; Nölle et al. 1998; Etzkorn et al. 1999; Stutz et al. 2000) and the measured slope at the wavelength λ a concentration value can be calculated for the single measurement at this wavelength. However, the aim is the derivation of a complete spectrum by plotting α(λ) versus λ. In this way, an improved value for the concentration can be calculated by least square fit to a reference spectrum of a specific concentration or corresponding absorption cross sections.
For a mixture of several absorbing compounds we get:

$$\begin{bmatrix} slope_{meas}(\lambda_1) \\ slope_{meas}(\lambda_2) \\ \ldots \\ slope_{meas}(\lambda_m) \end{bmatrix} \sim \begin{bmatrix} \sigma_1(\lambda_1) & \sigma_2(\lambda_1) & \ldots & \sigma_n(\lambda_1) \\ \sigma_1(\lambda_2) & \sigma_2(\lambda_2) & \ldots & \sigma_n(\lambda_2) \\ \ldots & \ldots & \ldots & \ldots \\ \sigma_1(\lambda_m) & \sigma_2(\lambda_m) & \ldots & \sigma_n(\lambda_m) \end{bmatrix} \bullet \begin{bmatrix} N_1 & N_2 & \ldots & N_n \end{bmatrix} \qquad [11]$$

1.9.4.2. Linear Evaluation

Theoretically one should get a directly evaluable sample spectrum if the raw spectra obtained for an empty cell (i.e. streamed by N_2 or clean air) is subtracted from the raw spectrum for the cell streamed by the sample gas. Thus, the influences of wavelength dependent mirror reflectivities or Rayleigh and Mie scattering are eliminated. As result an even spectrum should be obtained with extinction values directly comparable to a spectrum calculated from the absorption cross sections found in literature. However, a shift of the background level of the sample spectrum compared to the blank spectrum obtained before or thereafter was observed in most cases. This means that the resulting spectrum (sample spectrum minus background spectrum) shows a too high or too low (sometimes even negative) net extinction values. Furthermore, the resulting spectrum often exhibits a linear or even polynomial slope.

A shift of the background level can be caused by aerosol influence and by thermal effects produced by different temperatures of the gas fillings in the cell or by thermal instabilities of the laser system. An example for the spectra shift against a reference spectrum of the same analyte concentration is depicted in **Fig. 1.21.**.

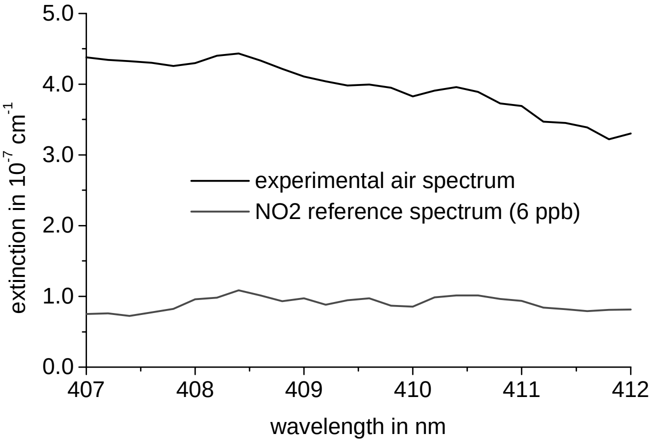

Fig. 1.21. Shift of a background corrected air spectrum compared to a reference spectrum of the same NO_2-concentration.

As the peak height is not affected by the shift of the background level of the spectra, it is possible to evaluate the spectrum and to determine the analyte concentration via the difference between the maximum and minimum of a peak in the spectrum. This method is not very accurate, however, a very high time resolution of the measurement can be achieved. The extreme case is a 2-point measurement at only two wavelengths, one at a minimum and one at a maximum in the spectrum. The obtainable time resolution lies only in the range of seconds. Another possibility is the shift of the experimental and the reference spectra to the base line (0-extinction) and the evaluation via the least square fit method. This proceeding improves the accuracy and precision, however, the shifting procedure still causes a remarkable error (10-20%) as it is difficult to define when a spectrum has exactly reached the base line.

A suitable method to overcome this problem is to subtract the polynomial fit of a spectrum from this spectrum. If the experimental spectrum is only shifted, a fit of 0^{th} polynomial (i.e. straight line without gradient) order will suffice. For an additional tilting of the spectrum (as, e.g., observed in **Fig. 1.21.**), a 1st polynomial fit order correction (i.e. straight line with gradient) is adequate. With a supplementary bending of the spectral curve, a 2nd order polynomial fit is a good solution to treat and shift the *experimental* spectrum, however, problems might occur for *reference* spectra as can be seen in **Fig. 1.22.**. While the order of the polynomial fit is of negligible influence in **Fig. 1.22.a**, for a simple peak as depicted in **Fig. 1.22.b**, severe shape variation become obvious. The calculation procedure for the reference spectrum should consider an extended spectral range, e.g. instead of the experimental range 407 – 412 nm the range 406.5 – 412.5 nm should be regarded for the calculation of the reference spectra according to **Fig. 1.22.**. This is especially important for the performance of the convolution procedure. Another example for the problems involved by the fit order is shown in the "results-section" (chapter **3**).

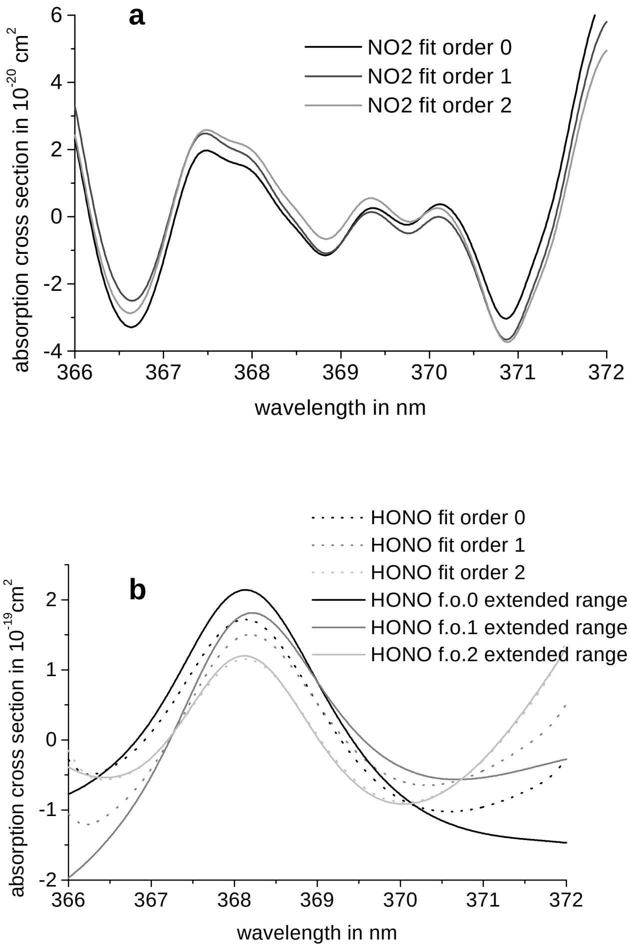

Fig. 1.22. Subtraction of different linear and polynomial fits from example spectra and the influence of the fit order of the correction as well as the influence of the spectral range onto the peak shape. **a:** structured multi-peak spectrum, **b:** simple peak.

Despite of the occurring problems, a non-differential evaluation method should be preferred for analytes with broad and smooth absorption structure as this feature is much less distinct or even disappears by the differentiation procedure. An important example for this kind of analyte is represented by nitrous acid.

1.9.4.3. Differential Evaluation

First order

Problems caused by the shift and tilting of the experimental spectra can be overcome by performing a derivation $dA/d\lambda$ of the spectrum. Thus, a simple shift ΔA_0 can be eliminated completely and a linear shift $\Delta A(\lambda)$ is transformed to a shift ΔA_0. The remaining shift ΔA_0 can be treated equivalent to means described in the "linear evaluation" – section (correction by a 0th order polynomial fit) or by subtraction of the mean value of the spectral array. This parameter is a good description of the shift as the mean of a differential spectrum generally should be approximately zero.

Higher orders

The big advantage of higher (2nd or 4th) order differential spectroscopy is the possibility of performing the evaluation without any background subtraction (i.e. background correction). Any shift or drift of the spectrum due to temperature or aerosol effects is deleted automatically. Disadvantageous, however, is the resulting strongly structured spectrum which is very sensitive to small shifts in the wavelength. It has to be mentioned, that wavelength shift and adjustment are not always strictly constant over the whole spectral measurements range. Artefacts might occur and, even worse, these artefacts might be strongly amplified. An example for the influence of the derivative order on the spectral shape and structure is shown in **Fig. 1.23.**.

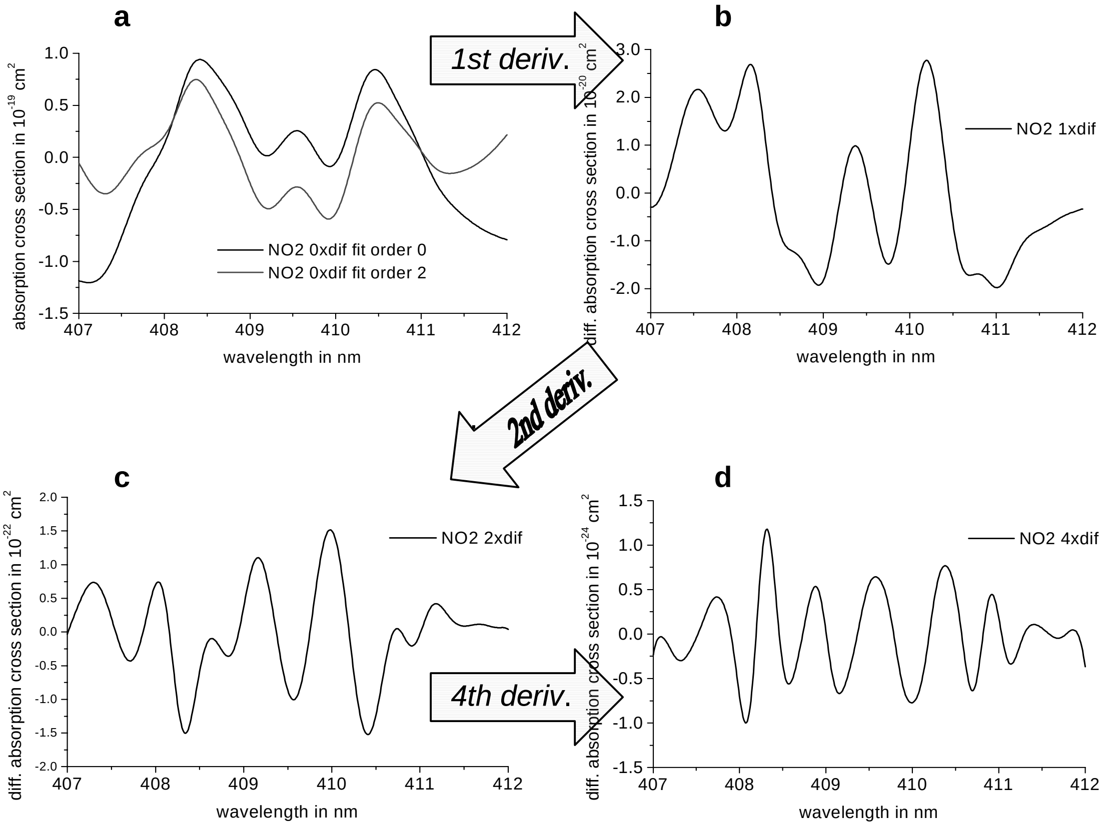

Fig. 1.23. Increasing derivative order applied on the same spectrum. **a:** no differentiation, **b:** first differentiation, **c:** second differentiation, **d:** fourth differentiation.

1.9.4.4. Evaluation with Experimental Reference Spectra

Another approach is the comparison with experimental spectra obtained for diluted standard reference gases instead of tabulated absorption cross sections. This method takes into account the instrumental parameters in a much better way. For instance the influence of the N_2/clean-air-mirror-flow, which is introduced to protect the mirrors from contamination, influences the experimental sample spectra of standard reference gases in the same way as the spectra of the ambient air. However, the experimental effort is much bigger. Furthermore, as discussed extensively in Chapter **3.1.**, clean air from the pure air generator does not exactly represent the properties of real air: for instance, the water vapour content of external ambient air has remarkable influence on the total quenching rate of the bath gas in the measurement cell. The non-representative character of reference gas measurements is especially significant when pure nitrogen is used as carrier gas due to multiple photochemical and photophysical effects as discussed in Chapter **3.1.**.

A good compromise is the determination of a correction factor obtained by the comparison of experimental spectra on reference gases with theoretical spectra calculated from absorption cross sections. This correction factor now can be applied on any experimental spectrum, i.e. spectra of real air samples.

An interesting option for the future is the addition of reference NO_2 to a stream of external ambient air which is strongly controlled by a high-quality flowmeter. In this way, all problematic effects occurring in an artificial atmosphere are omitted. The behaviour of NO_2 in this “real” atmosphere can be studied by adding a big excess of reference NO_2 to the low but unknown concentration of NO_2 in the sucked in outside air. This can be 100 ppb reference NO_2 regarding to about 10 ppb in the external air, however, city air might reach much higher concentrations which are not negligible against 100 ppb. The method of choice, however, could be the standard addition method (Skoog et al., 1988): employing this approach, two or more different well defined concentrations of standard gas are added to the real air sample (e.g. +10 ppb, +20 ppb, +50 ppb). The measured values obtained for the specified concentrations are plotted against the concentrations and the intersection of the linear fit with the x-axis directly reveals the NO_2-concentration in the outside air. This is schematically done in **Fig. 1.24.**: the 0-value of x corresponds to the measured sample value, the intersection of the dashed line with the y-axis to the concentration in the sample (with negative sign). The standard addition method is a very suitable procedure in order to eliminate so-called *matrix effects.* Unfortunately, this technique is comparatively time-consuming.

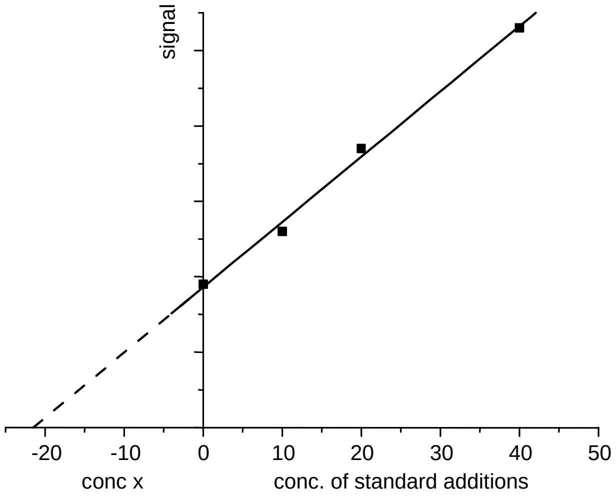

Fig. 1.24. Principle of the standard addition method. The 0-value corresponds to the measured sample value, the intersection with the y-axis to the concentration in the sample (-21.5).

1.10. Atmospheric Analysis with CRDS

1.10.1. CRDS-Studies with Atmospheric Concern

The technique is widely applied in laboratory (Busch and Busch, 1999) for molecular spectroscopy where detection of optical extinction as low as to 10^{-10} cm^{-1} has been reported (He et al., 1998). An overview is given by Berden et al. (2000) which also provides a comprehensive tabulation of the species probed by the CRDS-technique up to June 2000. Since two years, however, an increase in the interest of its application for environmental studies is obvious.

Laboratory CRDS studies of NO_2 were performed by Lauterbach at al. (2000) using a dye laser at 612.9 nm reaching a detection limit not better than 200 ppb. This can be explained by unfavourable absorption cross sections of NO_2 in this spectral range being 12-fold lower compared to the absorption maximum at 413 nm. Diffusion processes and catalytic degradation of NO_2 on the steel surfaces of the measuring cell were analysed showing first-order kinetics for the degradation into NO and O_2 under low pressure (long free-path length) of 1 mbar and no gas flow. Thus, it can be concluded that normal pressure and gas flow should overcome this problem.

Toxic compounds including nitrogen dioxide and four chlorinated aromatic volatile organic compounds were analysed by Vasudev et al. (1999). The detection limits were in the ppm-range, the spectral range was 562 – 569 nm for NO_2 and the fixed wavelength 266 nm (fourth harmonic of a Nd:YAG laser) for the VOCs. The most significant aspect of this work was, in opposite to LIF and REMPI, the independence of the sensitivity against the degree and site of the chlorination. A very interesting aspect of CRDS in this context is a possible detection of larger chlorinated aromatics like dioxins.

Evertsen et al. (2002) analysed NO and NO_2 in the exhaust of a diesel engine measuring values as high as 212 ± 22 ppm for NO at 226 nm and 29 ± 4 ppm for NO_2 at 438 – 450 nm. A sensitivity of 25 ppm and 3 ppm, respectively, was obtained for a reduced absorption path length of only 12 mm. With this set-up the influence of engine running conditions on the production of NO_x and soot could be studied.

First in-situ measurements of the NO_3 radical at fast time scales were performed by CRDS by King et al. (2000). The analyte NO_3 was detected in ambient room air that had been doped with a precursor of this radical, dinitrogen pentoxide, N_2O_5. It was recorded around its maximum absorbance at 662 nm applying a diode laser and performing on/off measurements at two wavelengths. The retrieved detection limit was 3 ppt.

Czyzewski et al. (2001) presented a study on NO_2 monitoring using a broadband laser source and a detector with a high spectral resolution. Signal detection was performed with a spectrograph equipped with a gated ICCD camera making it possible to analyse the signal simultaneously at various wavelengths within the laser linewidth around 425 nm. The technique proved to be much faster than commonly used CRDS and has a time resolution which is only limited by the repetition rate of the pulsed laser.

The same method was applied by Ball et al. (2001) for the monitoring of NO_3 in the atmosphere. They used a dye laser pumped by a Nd:YAG laser lasing in a continuous range of some 20 nm and a CCD camera for the simultaneous detection of spectrally resolved ringdown signals. The method has shown able to quantify NO_3 in laboratory samples simultaneous with impurities of NO_2. The achievable detection limit was 1.6 ppb, however, an estimation for field measurements revealed ringdown times smaller by a factor of 3 to 4. Brown et al. (2001) demonstrated in-situ monitoring capability of NO_3 and N_2O_5 using a laboratory arrangement which is able to heat the air flow through the inlet to 340-345 K and thermally dissociates N_2O_5 to yield NO_3. A comparison of the measured NO_3 concentration in its strong 662 nm band with and without heating allows the determination of N_2O_5. A detection limit of 0.3 ppt is reported for NO_3. The instrument was field tested and provided the first in-situ detection of N_2O_5 and first observations of this species in the troposphere. Again, laser source was a Nd:YAG pumped dye laser. Apart from Rairoux et al. (2002), which results are presented in this work, it seems to be at present the only CRDS-study performed on real atmosphere under field conditions.

Wang and Zhang (2000) performed laboratory CRDS-measurements on nitrous acid and report a detection limit of 5 ppb at the maximum absorption wavelength (354.2 nm). However, they predict a possible sensitivity of about 0.1 ppb for CRDS-analysis of

HONO by improving the parameters. Near-UV laser radiation (1-2 mJ/pulse) was generated from frequency doubling the output of a Nd:YAG 532 nm-pumped dye laser, the analysis is based on on- and off-resonance absorption measurements. Due to the lack of reliable reference absorption cross sections for HONO (thanks to the study of Stutz et al. (2000) this problem is overcome) the authors made their own absorption cross section measurements whereby a comparison with available literature values confirmed their method on principle. Interestingly, the measured HONO absorption cross sections were about 35% lower when argon was used as carrier gas instead of air. This can be explained by less efficient quenching of the electronically exited NO_2 by argon compared to air.

A completely different species was examined by Spuler et al. (2000) who made laboratory measurements on mercury. The Hg absorption profile in the 254 nm spectral region was analysed showing a dynamic range of 50 – 0.5 ppt.

Aerosols were measured by Smith and Atkinson (2001) with a portable pulsed CRD transmissometer simultaneously at two wavelengths at 532 nm and 1064 nm separating the scattering and absorption components. They applied various impactor stages and, hence, particle size cut-offs separating particles with diameters <1.6 um, <0.5 μm, and <0.2 μm. A laboratory based method for determination of atmospheric optical extinction by airborne particulate matter at 510 and 578 nm was presented by Thompson et al. (2002).

Table 1.1. gives an brief overview of all studies discussed in this section.

NO_2:	O'Keefe (1999), Vasudev (1999), Lauterbach (2000), Czyzewski (2001), Evertsen (2002), Rairoux (2002)*
NO_3:	King (2000), Ball (2001), Brown (2001)
HONO:	Wang Zhang (2000), Rairoux (2002)*
NO:	Evertsen (2002)
N_2O_5:	Brown (2001)
Aromatic VOCs:	Vasudev (1999)
Hg:	Spuler (2000)
Aerosols:	Smith and Atkinson (2001), Thompson (2002)
Field measurements:	Brown (2001), Rairoux (2002)*

* : results of the paper refer to this thesis

Table 1.1. Overview of CRDS-studies with atmospheric reference

1.10.2 Atmospheric Traces Suitable for CRDS

A selection of compounds of atmospheric interest which could be detected by the experimental set-up presented in this thesis is listed in **Table 1.2.**. Furthermore, the main absorption band, the dynamic range, and the theoretical detection limit can be learned from this table. The detection limits are based on simulation calculations considering the specified mirror reflectivities (R = 0.9999) and the respective differences in absorption cross sections found in literature (Merienne et al., 1995; Hitran96, 1996; Trost et al., 1997; Nölle et al. 1998; Etzkorn et al. 1999; Stutz et al. 2000). In another presentation (**Fig. 1.24.**) the differential absorption cross sections of selected atmospheric trace gases are visually displayed directly showing possible interferences. The detection limits from **Table 1.2.** were added to this presentation prepared for DOAS by Geyer (2000).

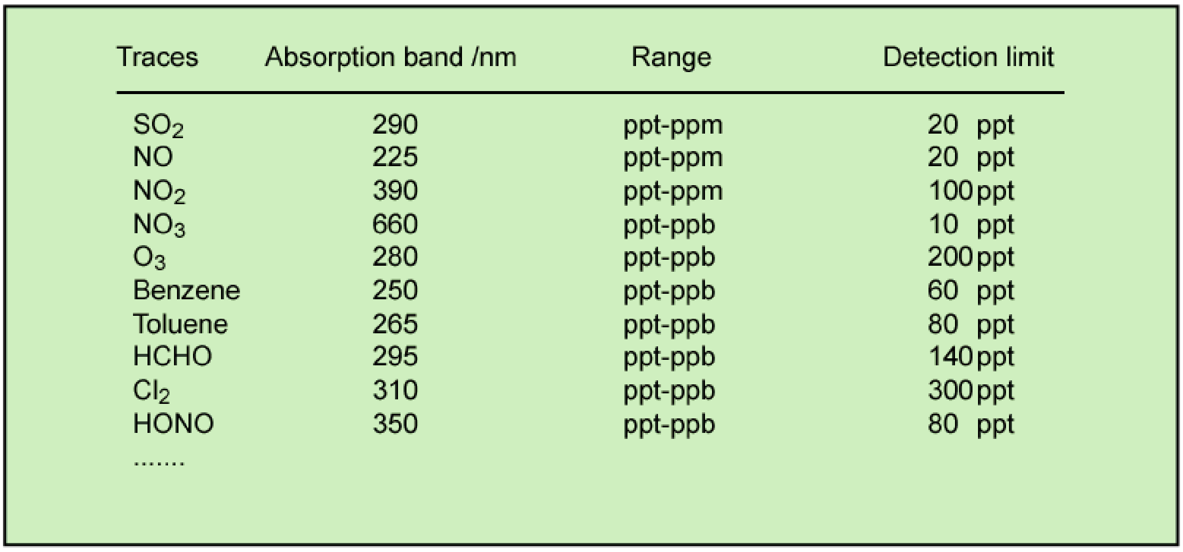

Traces	Absorption band /nm	Range	Detection limit
SO_2	290	ppt-ppm	20 ppt
NO	225	ppt-ppm	20 ppt
NO_2	390	ppt-ppm	100 ppt
NO_3	660	ppt-ppb	10 ppt
O_3	280	ppt-ppb	200 ppt
Benzene	250	ppt-ppb	60 ppt
Toluene	265	ppt-ppb	80 ppt
HCHO	295	ppt-ppb	140 ppt
Cl_2	310	ppt-ppb	300 ppt
HONO	350	ppt-ppb	80 ppt
....			

Table 1.2. Survey of compounds detectable by CRDS including their main absorption band and theoretical detection limit (calculation based on simulation).

1.10.3. Selection of Test Analytes

The wide spectral range and the distinct structure of the absorption spectrum of NO_2 in the visible and near UV-range makes it a very suitable test compound for the newly developed CRDS-monitoring device. The heights of the well-structured sharp and distinct peaks in the spectral region around 410 nm exhibit an extinction of about $6 \cdot 10^{-8}$ cm^{-1} (10 ppb), values which easily should be in the range of the apparatus. These concentrations can be artificially adjusted by mixing clean air or N_2 with commercially available synthetic NO_2. Furthermore, because NO_2 can be well monitored by standard in-situ monitoring devices based on photoluminescence, the detection of this compound is well adapted for performing devices comparison. As its detection can be difficult due to its low atmospheric concentration in rural and remote areas (background value: 100 ppt), the determination of NO_2-contents in the ambient air is a good challenge for CRDS.

The detection of HONO is basically possible with CRDS and as its absorption spectra interfere with NO_2 in the near UV/ visible spectral range a simultaneous determination can be performed. However, the smooth shape of the HONO-absorption profile makes its detection a difficult analytical task. Last but not least it must not be forgotten, that NO_2 as well as HONO are compounds of high interest in atmospheric chemistry as described in Chapter **1.2.**. Thus, it can be stated that these species are perfect test analytes for verifying the functionality of the CRDS-instrument.

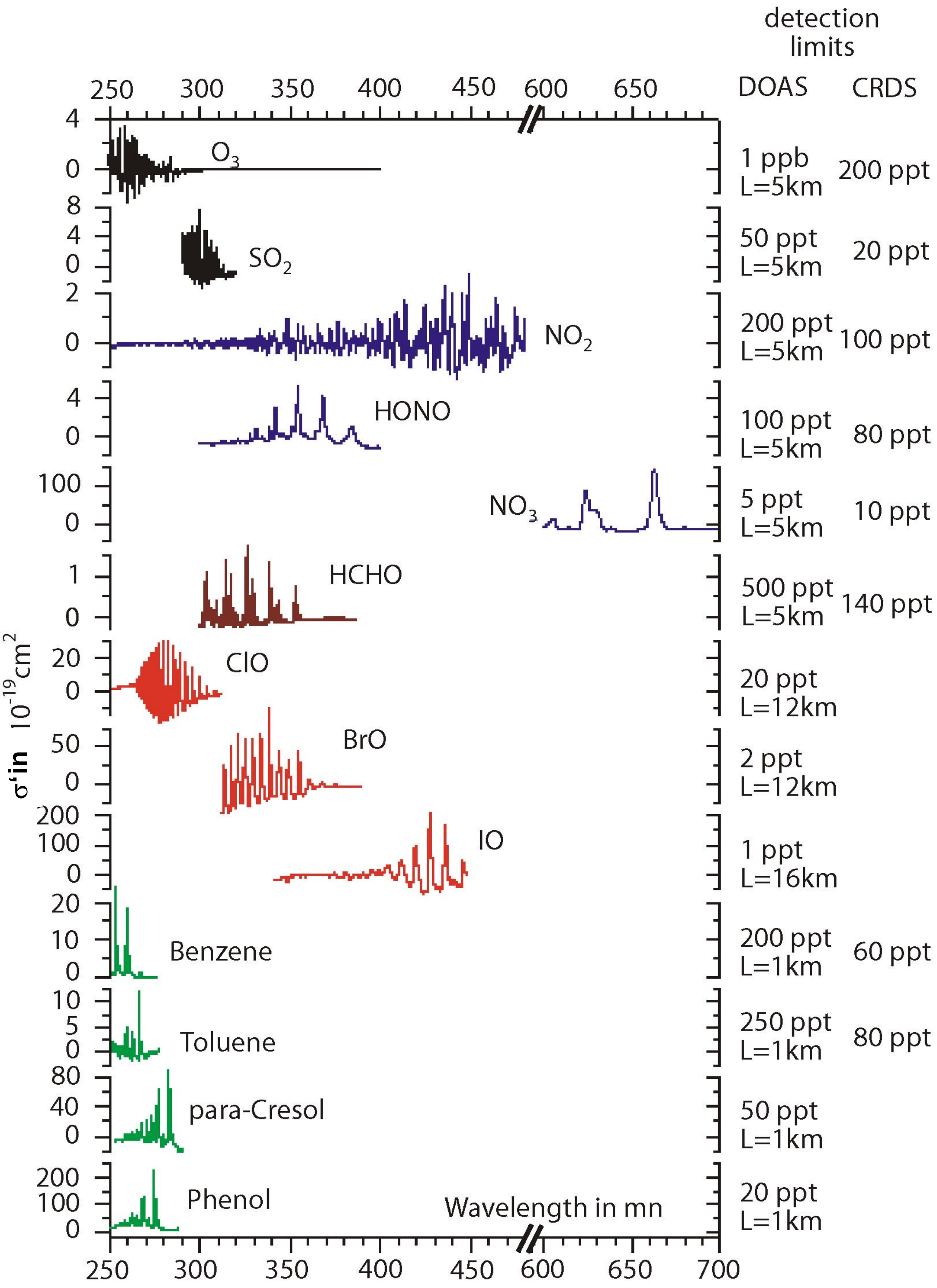

Fig. 1.25.. Differential absorption cross sections σ′(λ) of selected atmospheric trace gases measurable by CRDS and DOAS. Adapted from Geyer (2000). It can be seen easily which compounds interfere with each other.

2. Experimental Approach to Cavity Ringdown Spectroscopy

2.1. Experimental Set-Up

2.1.1. General Set-Up

The functional elements and manner of operation of the cavity ringdown spectroscopy device are schematically presented in **Fig 2.3.**. The laser source is based on a pulsed (10 Hz, 4 ns) Nd-YAG (Surelite II, Continuum, USA) pumped OPO laser (VisIR, GWU, Germany) with a SHG module (**Fig.2.1.**). It is continuously tunable between 250 nm and 1100 nm with a constant linewidth of 5 cm^{-1}. As described in Chapter **1.6.** the laser generates simultaneously two frequencies (signal and idler) which lie in the visible (500-700 nm) and in the near infrared spectral range (700-1100 nm), respectively. The generation of the second harmonics (SHG) of both emissions allows to cover the UV-visible spectral range (250-400 nm) with pulsed energy in the 5 mJ level.

The laser source was especially developed for this application in the framework of the DBU (Deutsche Bundesstiftung Umwelt) project "Atmospheric Diagnostics". The thermal and mechanical stability of the laser were optimised in order to be compatible with field measurements. Moreover, a novel configuration of the laser oscillator could drastically decrease the beam divergence, below 1 mrad, and also getting a symmetric beam profile (Anstett G., 2001).

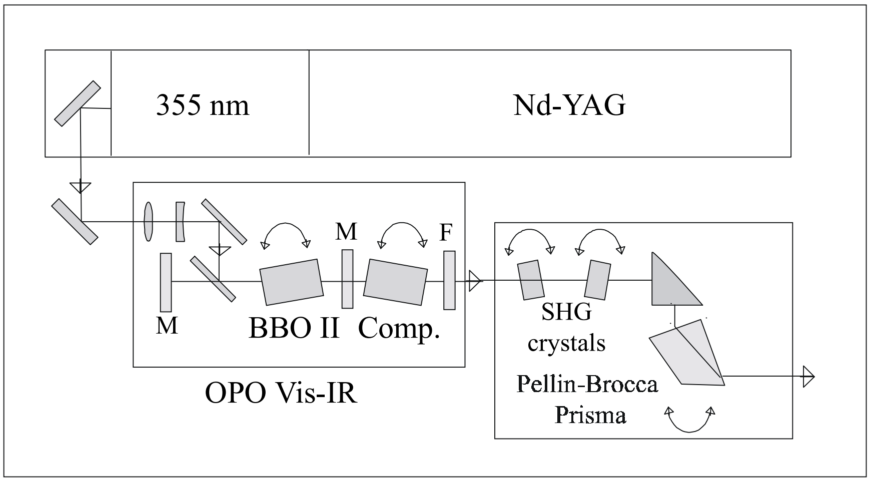

Fig. 2.1. Set-up of the OPO laser system. It consists of a nonlinear BBO-crystal pumped by the third harmonic of a Nd:YAG-laser. The achievable wavelength range is extended by another pair of nonlinear SHG-crystals.

Between OPO output and input mirror of the optical cavity a spatial filter consisting of two convex lenses was situated.

The beam leaving the OPO passes a 3 mm – pinhole before being optimised by a head-on lens (50 mm focus length) followed by a 100 mm lens forming the space filter. In this way disturbing transversal modes can be suppressed. An optional pinhole could be placed between the two lenses, another 1 mm – pinhole was installed in front of the input mirror of the cavity.

The optical cavity consists of two concave mirrors (6m radius of curvature) having a reflectivity better than 99,95 % (Los Gatos Research, USA) and a distance of 50 cm. A stainless steel gas cell is set between the mirrors providing a constant gas flux to be probed. The flow cell consists of parts of the Leybold vacuum system (Leybold, Germany) and can easily be prolonged or cut by adding or removing additional Leybold-“bricks”. (**Fig. 2.2.**). Each brick is 10 cm in length, flexibility in the total length is provided by bellow parts. Furthermore, the cell can be run under pressure or vacuum. A small flow of dry N_2 passes through the mirrors assuring that they remain clean during air probing. For this purpose a small purge chamber (L = 3 cm) streamed by N_2 was separated in front of the dielectric mirrors by 8 mm-diameter diaphragms allowing the laser beam to pass. The added flow in the cell decreases the probing length of the cavity by a value of 11 %. How the cell looks like in operational reality is presented on the photos in **Fig. 2.8.**.

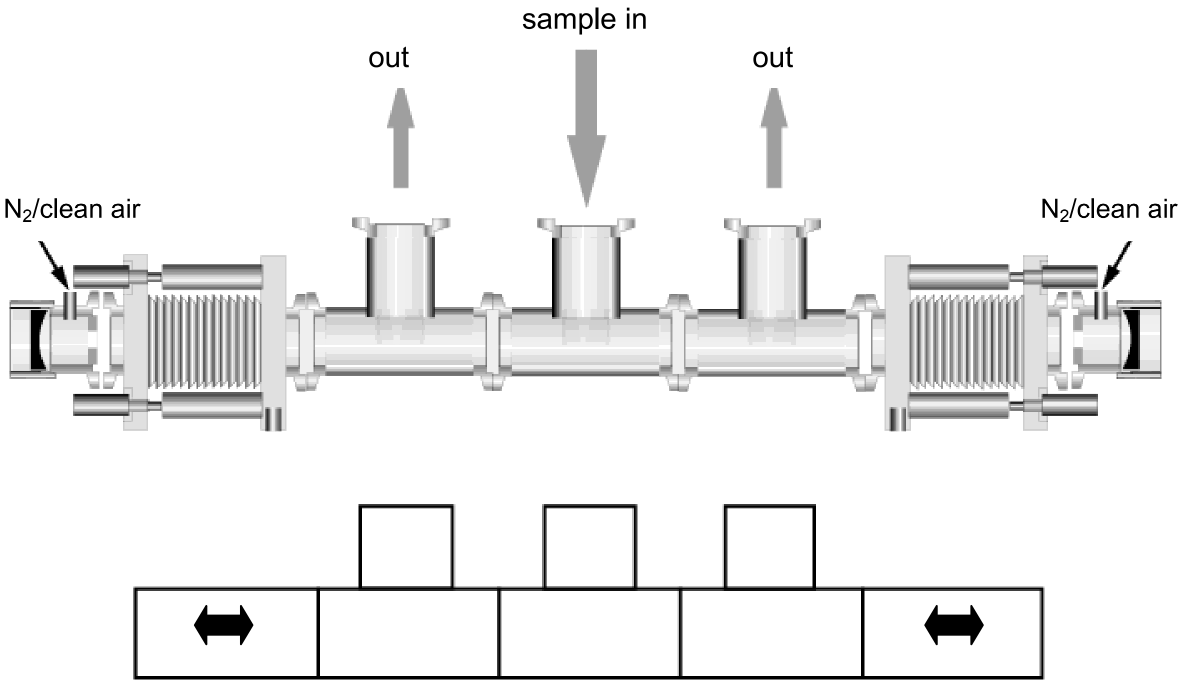

Fig. 2.2. Picture and rough diagram of the measuring cell. Major changes in length can be made by adding or removing bricks, minor changes within the bellows. Mirror alignment is performed by micrometer screws indicated left and right in the picture.

Time resolved signal measurement is performed by using a fast photo-detector (Hamamatsu R7400P4, Japan) electrically coupled to a 12 bits digital transient recorder (Licel, Germany). Alternatively the signal can be recorded with an oscilloscope (tektronix TDS 3032). This is especially useful when the CRDS-signal is searched during cavity alignment and for course adjustment. The signals are recorded on PC and are on-line elaborated using self developed procedures (LabView, USA). The entire CRDS device is mounted in a 1,5 x 0,6 x 0,5 m rigid rack allowing an easy implementation in the different monitoring platforms (container, track, airplane) as shown in Chapter **2.1.3.**.

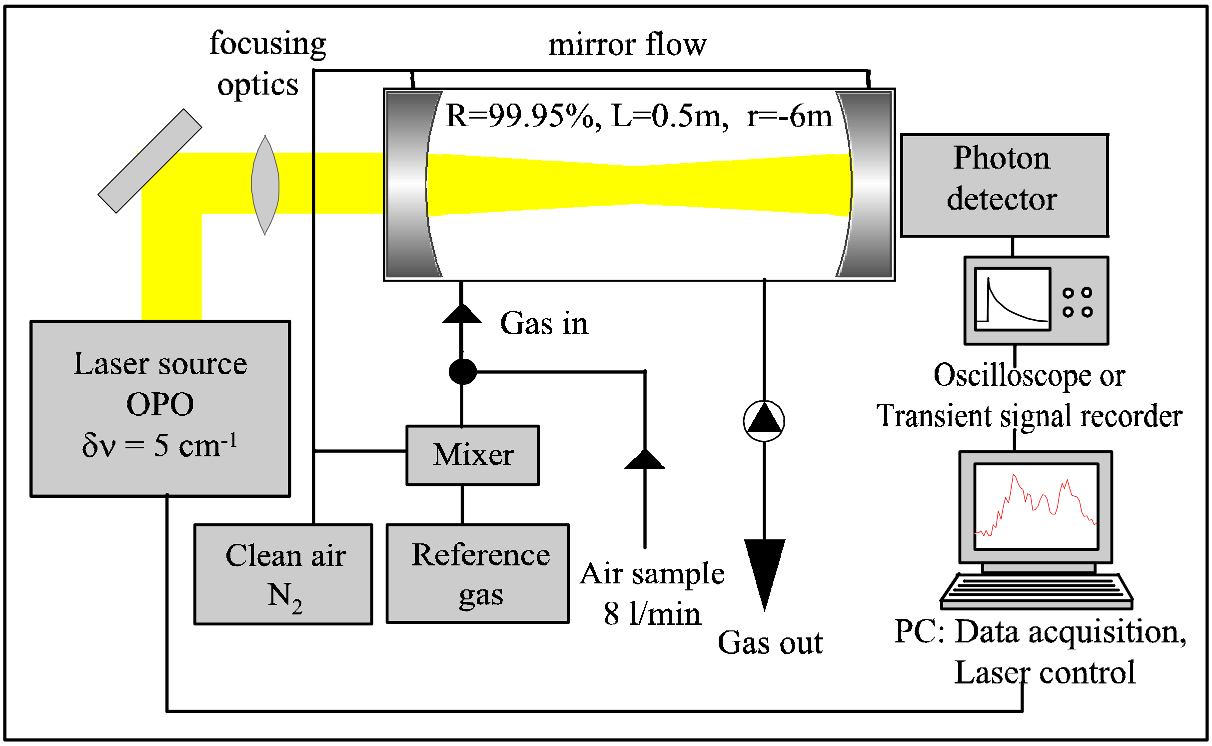

Fig. 2.3. Set-up of the cavity ring down spectroscopy (CRDS) monitoring device.

2.1.2. Mirrors and Filters

Dielectric mirrors

Mirrors of low loss and high degree of reflection can be realised by sandwich-like stacks of λ/4 layers. These transparent layers are alternating between a high and low refractive index and have an optical thickness $nd = n'd' = \lambda/4$. They are deposited by evaporation on a transparent substrate. Constructive interference of the light waves reflected at the boundary planes leads to a high degree of reflection for large numbers of layers. Typical high reflectance mirrors may be composed of up to forty λ/4-dielectric layers and reach a reflectivity of more than 99.99%. As shown in **Fig. 2.4.**, the reflectivity is strongly wavelength dependent. By comparison of this experimentally determined reflectivity curves for LGR mirrors (HR at 390 nm) with the absorption spectrum of NO_2 (**Fig. 2.5.**) a suitable spectral range for the analysis can be selected and the measurable extinction can be estimated. Busch and Busch (1999), Eichler and Eichler (2001).

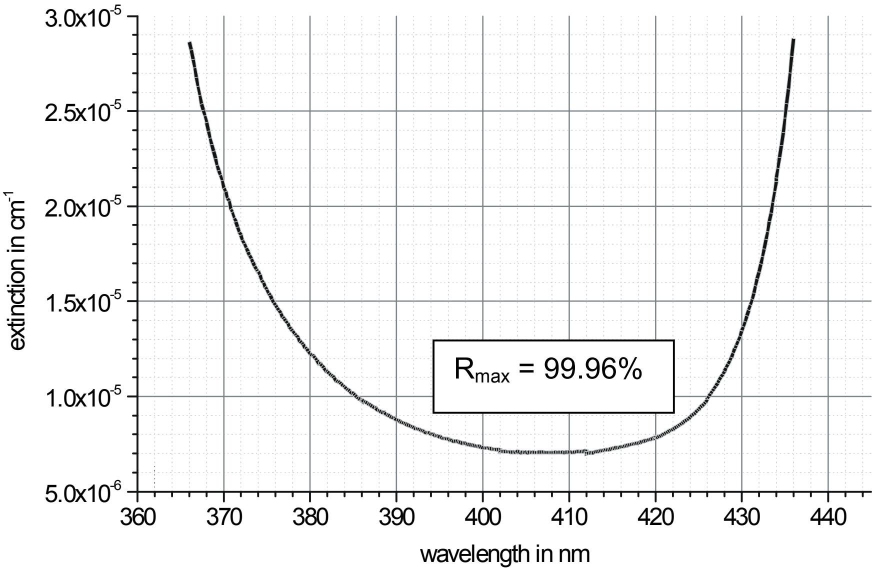

Fig. 2.4. Experimentally determined reflectivity curve for Los Gatos mirrors with specified HR at 390 nm. Maximum reflectivity is 99.96%.

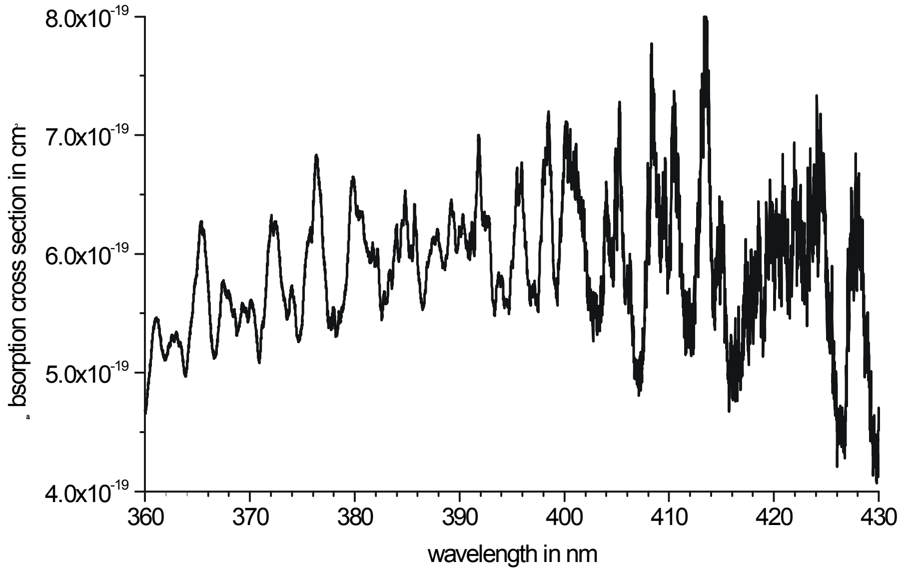

Fig. 2.5. Absorption spectrum of NO_2 for the spectral range of suitable mirror reflectivity.

Filters

In order to avoid disturbing and interfering light an optical filter has to be installed between the CRDS measuring cell and the photon detector. As most measurements were performed in wavelength ranges around 400 nm an interference filter with a specified maximum transmittance at 400 nm (L.O.T-Oriel, Darmstadt) was applied. Its transmission curve is depicted in **Fig. 2.6.**.

As HONO-analysis has to be carried out at 368 nm, a wavelength with obviously too low filter transmittance according to **Fig. 2.6.**, the following filter property was utilised: the transmission of interference filters depends on the filter inclination against the incident light beam. In this way the central wavelength can be lowered by 10 – 20 nm (**Fig. 2.7.**), though at the expense of a broadening and lowering of the transmitted filter band.

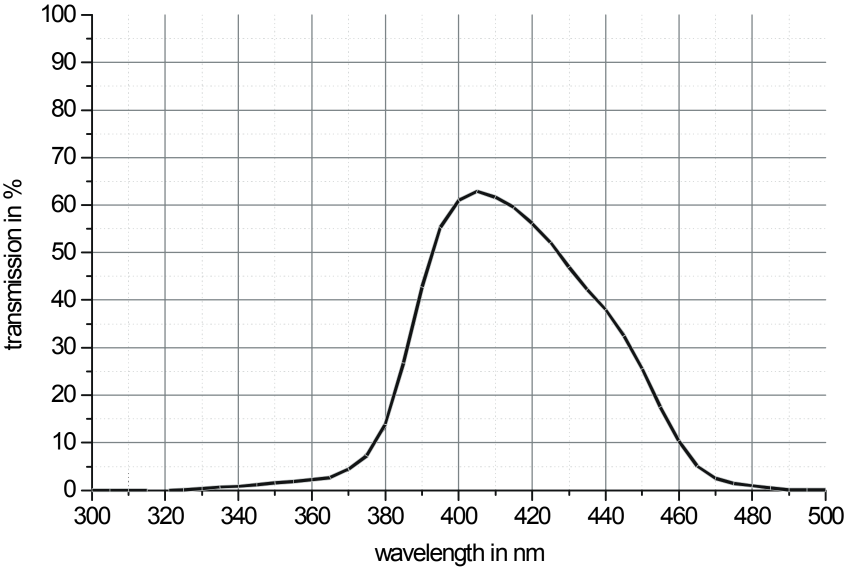

Fig. 2.6. Transmission of the LOT-filter applied for NO2 and HONO analysis

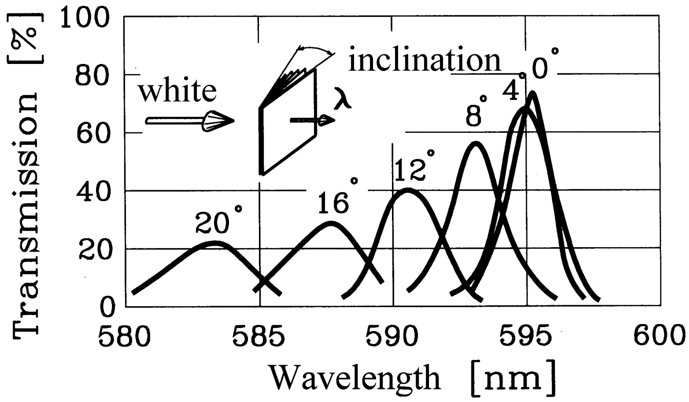

Fig. 2.7. Example for the shift of the central wavelength and the transmission of a interference filter in dependence of its angle of rotation. Schmidt (1994).

2.1.3. Set-Up for the FELDEX 2000 Field Campaign

The photos **Fig. 2.8.** show the CRDS set-up integrated in a caravan for the FELDEX 2000 field campaign on Kleiner Feldberg (825 m) in the Taunus region near Frankfurt/Main (Germany). The caravan is a good example for the integration options of the CRDS set-up, however, further minimising is possible without problems. The momentary core of the system is the rack depicted in the foreground of **Fig. 2.8.b** while the rack containing the voluminous gas mixing system (background of **Fig. 2.8.b**) is negligible. The left part (according to **Fig. 2.8.a**) of the caravan is separated by a robust light and noise absorbing curtain and contains a comfortable PC desktop. During the campaign the system proved its reliability even under harsh conditions.

Fig. 2.8.a. For the FELDEX 2000-campaign near Frankfurt the CRDS-set-up was installed in a caravan. The gas inlet can be seen on the top, the pump was deposed in the boot on the right.

Fig. 2.8.b. Rack containing the set-up including pump laser, OPO and measurement cell. In the rear the laser power supply (left) and the rack with the gas mixing system can be distinguished (right).

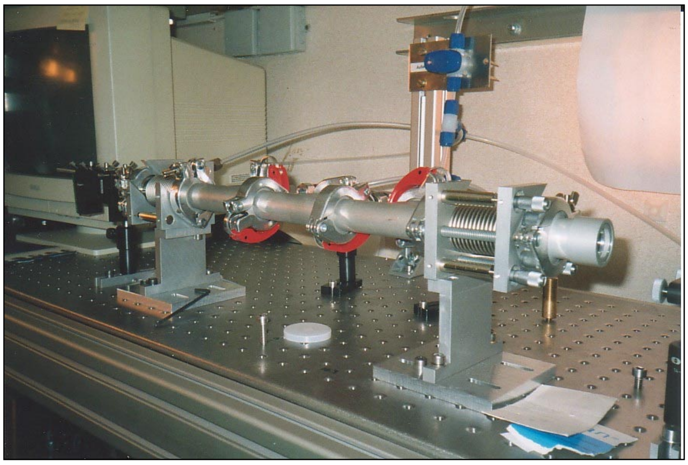

Fig. 2.8.c. Optical cavity and measurement cell

Fig. 2.8.d. Desk with PC for data acquisition and evaluation (and panorama window)

2.2. Set-Up Optimisation

2.2.1. Distance of the Focusing Optics

The position of the focusing optics (telescope), realising the coupling of the laser beam into the optical cavity, can be experimentally optimised by observing the CRDS-signal on the oscilloscope and improving its shape and structure. After that a further optimisation can be performed regarding the signal minus fit (residual) diagram obtained by the transient recorder (**Fig. 2.14.**, Chapter **2.4.**).

Another possibility to optimise the lens distance and position is the simulation programme written in LabVIEW which was presented in Chapter **1.8.**.

2.2.2. Gas Flow

Measurements were carried out for equal reference gas mixing ratios within the cell which were produced by different gas flows. This was performed by different flows of N_2/clean air and 1 ppm/ 10 ppm standard gas which lead to the same mixing ratios. As no variation in the measured NO_2-concentrations could be detected for different total gas flows in the cell, an independency of the results from the gas flow can be concluded.

2.2.3. Shot Characteristics

Variation of the pump laser energy

The energy of the third harmonic of the Nd-YAG-laserpulses was measured by a Powermeter (Molectron J25) situated directly behind the laser head. For protection of the powermeter a concave lens was fixed between laser head and powermeter in order to enhance the beam divergency. As can be seen from **Fig.2.9.** the Surelite II is running very stable, the variation within the single pulses is below 4%.

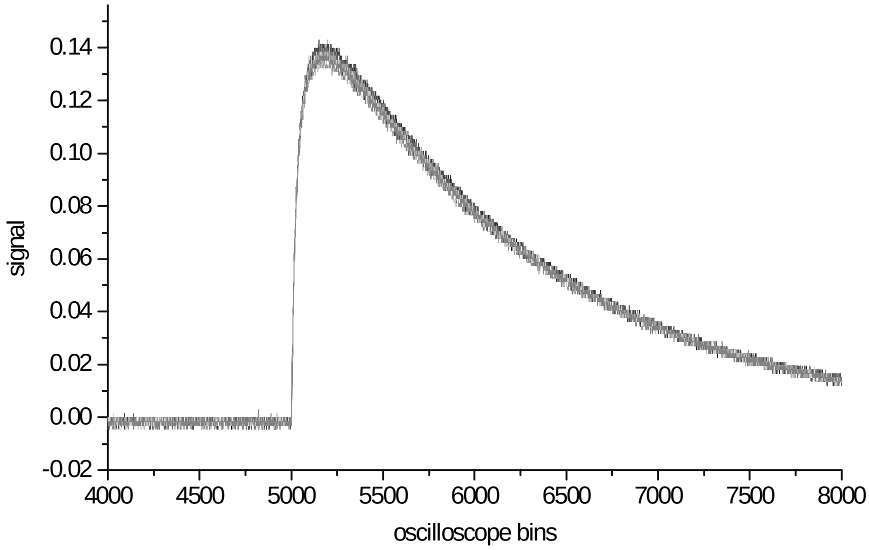

Fig. 2.9. Variation of the Nd-YAG-laserpulse-energy for 20 consecutive shots.

Signal variation

The distribution of the maximum peak heights of a big amount of consecutive CRDS-signals is depicted in **Fig. 2.10.**. In order to check the influence of the general mean peak height on the variation properties the measurements were performed at three different wavelengths (reflecting varying mirror reflectivities). Thus, it was possible to keep any other parameters constant, especially the voltage at the photon detector. Regarding the standard deviations, it is obvious that at least 27% of the signals should be deleted. This corresponds to about the seventh of the highest and the seventh of the lowest signals. A look at the shape of the three curves reveals that a signal amplitude of 50-60 mV should not be exceeded as the distribution properties are becoming worse for the 412 nm-curve which shows a signal amplitude of 74 mV.

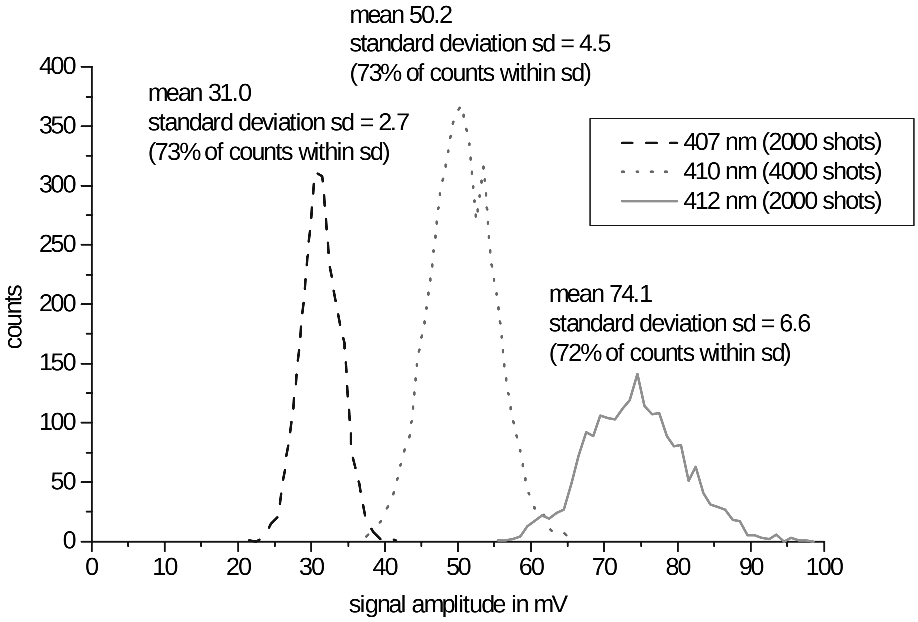

Fig. 2.10. Distribution of the maximum peak heights at three different wavelengths.

The positive influence of signal deletion on the variation of the CRDS-signals and, therefore, on the noise of the measured extinction and, finally, on the spectrum structure and the detection limit can be seen in **Fig. 2.11.**. After deletion of the five highest and the five lowest signals in a set of 20 signals the overall variation can be reduced remarkably.

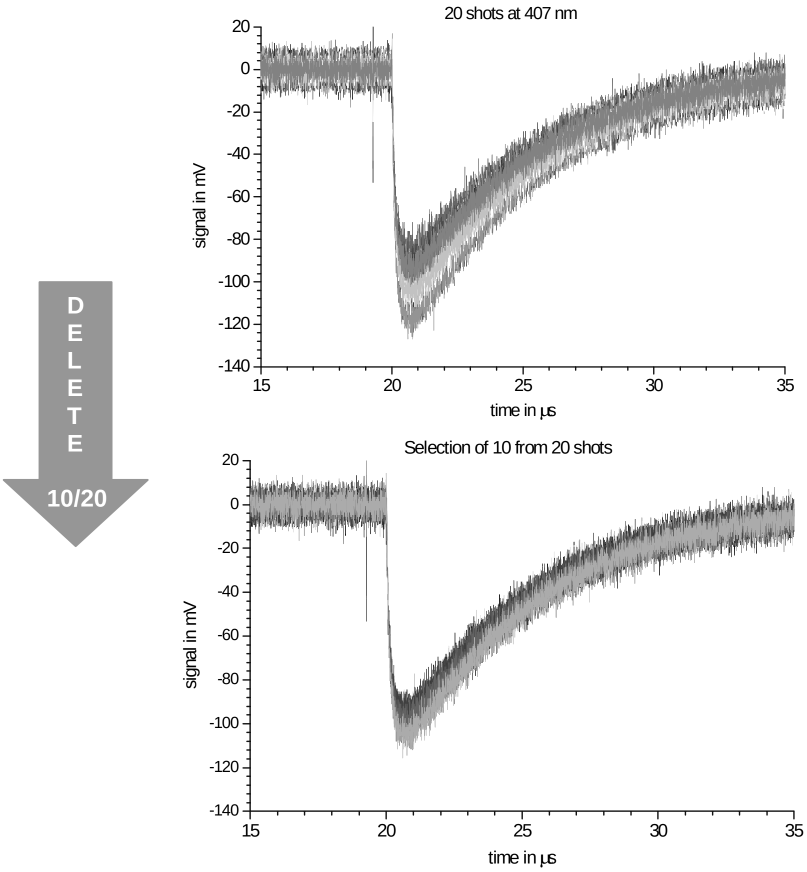

Fig. 2.11. Reduction of the variation of the CRDS-signal after deletion of the lowest and highest signals of the set.

2.2.4. Optimisation of the Shot Selection

The total number of shots to be averaged and the number of shots to be deleted has to fulfil several contra-productive aspects in order to optimise the variation and the quality of the CRDS-measurements. A large number of averaged signals improves the spectrum quality, however, consequently the time resolution is deteriorated. Another aspect to be considered when averaging very big number of shots are changing longer term properties like temperature effects and aerosol influences. Decisive parameters are the error bars depicted in **Fig. 2.12.** for any result, and obviously the increasing bar for the very right point gives a hint on the aspects mentioned above. As minimum error bars appear for a measurement of 90 averaged shots with 30 signals deleted, these values were used as initial parameters.

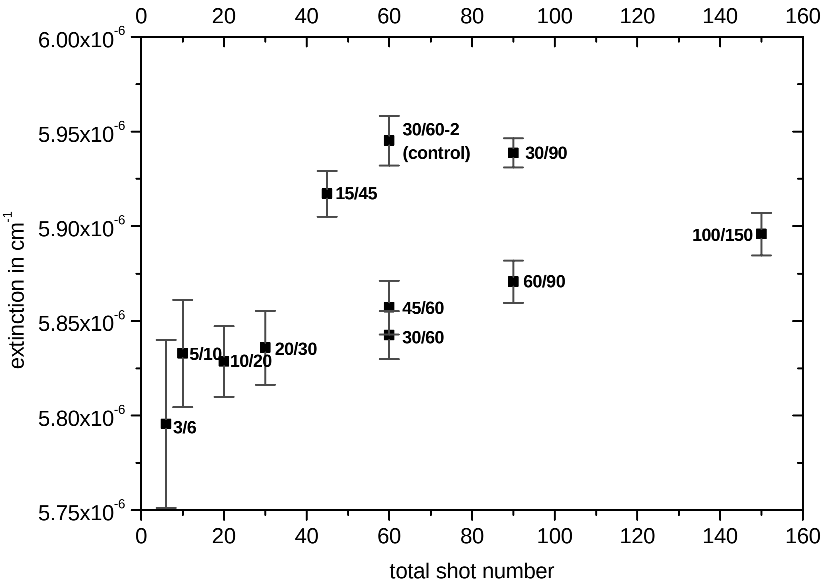

Fig. 2.12. Number of deleted shots in relation to the total number of shots and the influence of these parameters on the error bars (standard deviation) of the measured extinction values.

2.3. Calibration and Reference Gas Measurements

The calibration procedure is performed in two steps. The first one consists of the determination the spectral dependence of the time constant in the monitoring spectral range. For this, the cavity is filled with a 0.5 – 6 l/min constant flow of dry Nitrogen (5.0 quality, Messer Griesheim). A pure air generator (PAG 003, Eco Physics) has also been used for this purpose during field measurements. The second step consists of the calibration of the absorption measurement and the concentration retrieval procedure. For the calibration of NO_2 and HONO measurements in the 400 nm band, the cell is filled with NO_2-standard gas (Messer Griesheim, Germany) of the specified concentrations 0.86 ppm and 9.79 ppm, respectively, diluted by nitrogen (5.0 quality, Messer Griesheim) using flow controllers (MKS instruments 20 slm, Tylan 2900 series 3 slm). Alternatively, a clean air generator and gas mixer (Eco physics) were applied for dilution purposes. A basic calibration was performed in laboratory which sets the dynamic range and the detection limit. During field experiments the calibration is ideally performed within a cycle of one hour by fixed concentration (10 ppb) of NO_2 reference gas to assure the data quality. However, as reference gas measurements in nitrogen or clean air atmosphere systematically reveal too low values compared to the adjusted concentration, correction factors for the respective gas atmosphere have to be introduced. Possible reasons for this underestimation are explained in detail in Chapter **3.1.**.

Most calibration measurements were performed in the 407 nm to 412 nm spectral range with 0.2 nm spectral resolution. The measurement time was 6 minutes per spectra and each CRDS signal was averaged on 60 laser shots.

This calibration procedure does not consider interferences with other trace gases and aerosols. The contributions of other trace gases are taken into account applying absorption spectra from the literature (Merienne et al., 1995; Hitran96, 1996; Stutz et al., 2000) in the concentration retrieval procedure.

2.4. Data Acquisition

A simplified scheme of the data acquisition procedure is depicted in **Fig.2.13.**. The basic structure of the data acquisition program written in LabVIEW consists of *three loops*: the read procedure for consecutive wavelengths is performed in the innermost loop. This represents a scan over the whole wavelength range determined by the initial parameters. One of these initial parameters is the scanning step width which determines the spectral resolution. Maximum resolution is 0.1 nm, however, the step width can be enhanced for a better time resolution. OPO step motors responsible for adjusting the wavelength are controlled by a PC via a RS232 serial port. It is possible to switch off the OPO control in order to perform long-term measurements on one single wavelength. This is especially useful for the study of temperature and aerosol effects. Furthermore, the cavity alignment by optimising the signal shape and slope is simplified when the OPO is switched off due to the faster repetition rate of the single signals.

The data transfer from the transient recorder or, alternatively, the oscilloscope to the PC is realised by a GPIB-card and a NIDAQ-card, respectively. Succeeding the "read-step" the best signals, i.e. the mean signals of the whole range of shots, are selected considering the results described in Chapter **2.2.**. In a sub-VI (VI = Virtual Instrument) the single CRDS-signals are ordered according to their maximum peak height and, subsequently, the highest and lowest signals are deleted. The program also includes an option to save single CRDS-decay-signals.

After application of the natural logarithm to the CRDS-signal showing an exponential decay curve, a linear fit is performed. A plot which shows the signal, its fit, and, most important, the difference between signal and fit (**Fig.2.14.**), gives two important information: the cavity alignment can be performed regarding two aspects, the measured value of the slope and the signal-fit-difference (residual) which should look as straight and even as possible. In other words, the cavity can be aligned by optimising the signal slope simultaneously with the shape of the residual curve by tilting the mirrors, varying lens and pinhole distances, pinhole diameters and so on. The second information which can be extracted from **Fig.2.14.** is the fit range of the CRDS-signal. In this context the end of the fit range should be situated near the cross section of the signal-fit-line ("linear fit" in Fig. 2.14.) with the signal-minus-fit-curve ("difference" in Fig.2.14.). As one bin corresponds to 25 ns, the 1000 bins of the transient recorder correspond to 25 µs or 7.5 km. Typical fit ranges amounted to 600-700 bins (15 µs). The single spectrum consisting of a 2-dimensional array of measured signal slopes and wavelengths is plotted on the panel and can be saved optionally.

The middle loop in **Fig.2.13.** allows the repetition of the scan and immediately gives the mean spectrum obtained from the single scans. Normally three scans or single spectra, respectively, were averaged to a mean spectrum which was saved automatically. Long-term measurements can be performed by the use of the outermost loop enabling any sequence of mean spectra covering any time period.

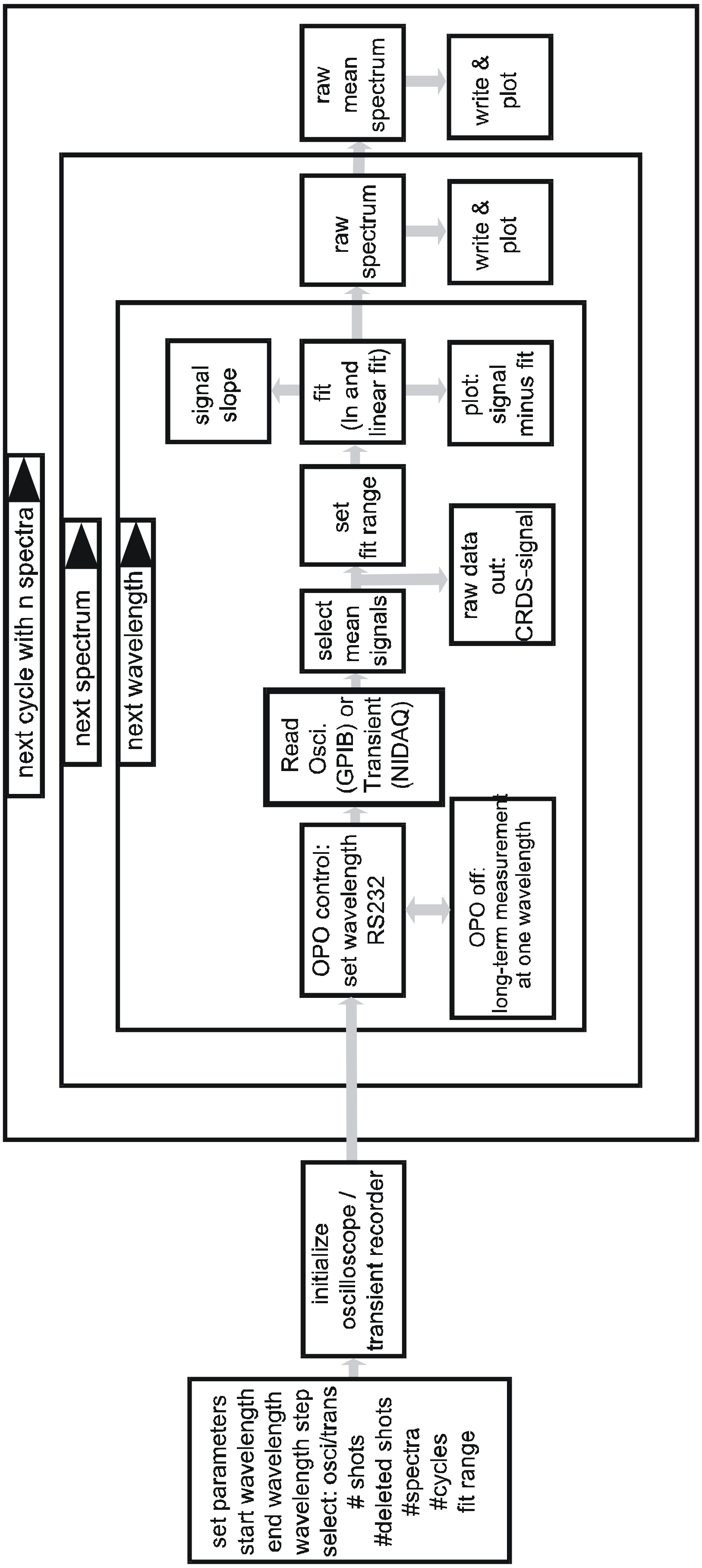

Fig. 2.13. Simplified scheme of the data acquisition program

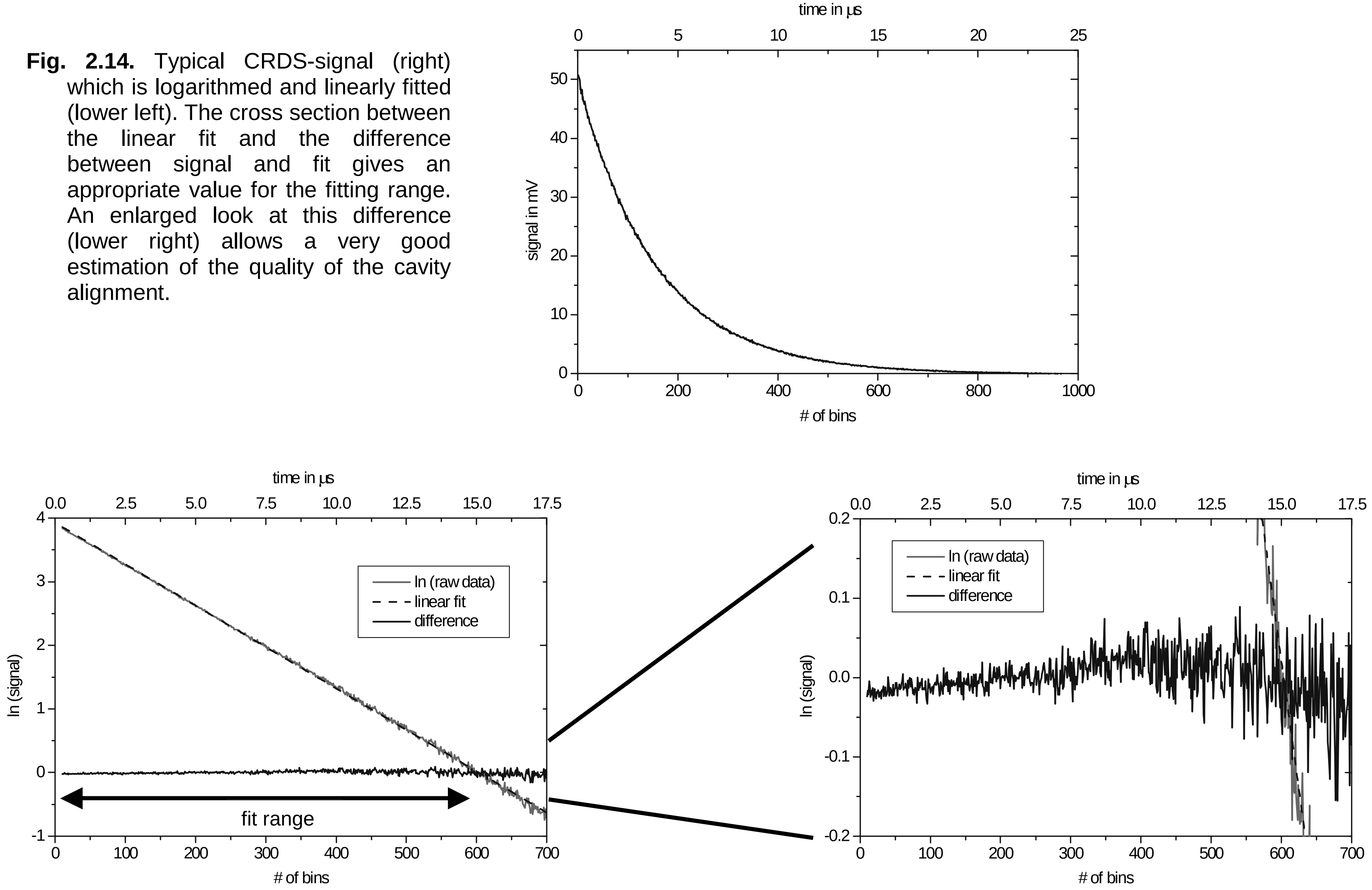

Fig. 2.14. Typical CRDS-signal (right) which is logarithmed and linearly fitted (lower left). The cross section between the linear fit and the difference between signal and fit gives an appropriate value for the fitting range. An enlarged look at this difference (lower right) allows a very good estimation of the quality of the cavity alignment.

2.5. Evaluation Procedure

2.5.1. Evaluation Scheme

A simplified scheme of the evaluation procedure performed by a LabVIEW program is depicted in **Fig. 2.15.**. Input (all inputs in the scheme are indicated by *grey* boxes) is a 2-dimensional array consisting of the measured extinction in cm^{-1} and the joined wavelengths in steps corresponding to the wavelength steps during data acquisition.

The 1-dimensional extinction array is convoluted with a Gauss-curve simulating the laser beam, a procedure, which results in a considerable smoothing of the raw spectrum. Critical parameter of the Gauss-curve is its width at 5/8 maximum height, which was chosen in the range between 0.1 nm and 0.5 nm. For successful convolution the extinction array and the Gauss-curve have to be set on the same scale, i.e. an equivalent array length at a preferable resolution of 0.01 nm. For lower resolutions (like the wavelength step 0.1 nm – 0.5 nm during data acquisition) no smooth Gauss-curve can be generated. Hence, an interpolation of the extinction array is unavoidable.

In the next step the evaluation mode can be selected between evaluation without differentiation (called “linear evaluation” in the scheme) or derivative spectroscopy for any derivative order. Best results can be obtained for “linear evaluation” including the subtraction of a polynomial fit of the raw spectrum or for the first derivation of the spectrum including the subtraction of its mean. In both cases a shift of the raw spectrum onto the baseline (0-extinction) is performed in order to eliminate any slopes within the spectrum caused by aerosols and/or temperature effects. Another method of choice revealing the same effect could be an evaluation by the second or fourth derivative of the spectrum. Further details on advantages and disadvantages of the different evaluation modes are discussed in chapter **1.9.**.

Now the modified spectrum can be compared to an experimental or calculated reference spectrum of appropriate concentration concerning the main analyte. For instance, in most cases a 10 ppb NO_2-spectrum has proved to be suitable for this purpose as this concentration lies in the rough range of atmospheric NO_2-contents. However, any other comparison concentration can be adjusted in the program. The comparison procedure enables the determination of wavelength shift and evaluable spectral range. Several cycles might be necessary in order to find the optimum values concerning the parameters wavelength shift and spectral range under consideration.

Finally, the analyte concentration is calculated for the optimised parameters by the least square fit method and multi-compound analysis (algorithm described in chapter **1.9.**). Input is the respective array containing the absorption cross sections for the different analytes. On principle, the number of analytes is unlimited, however, it makes no sense to consider more than three different species (chapter **1.9.**). As output an array containing the concentrations of the analytes is obtained as well as a new and corrected plot of the spectrum including a reference spectrum.

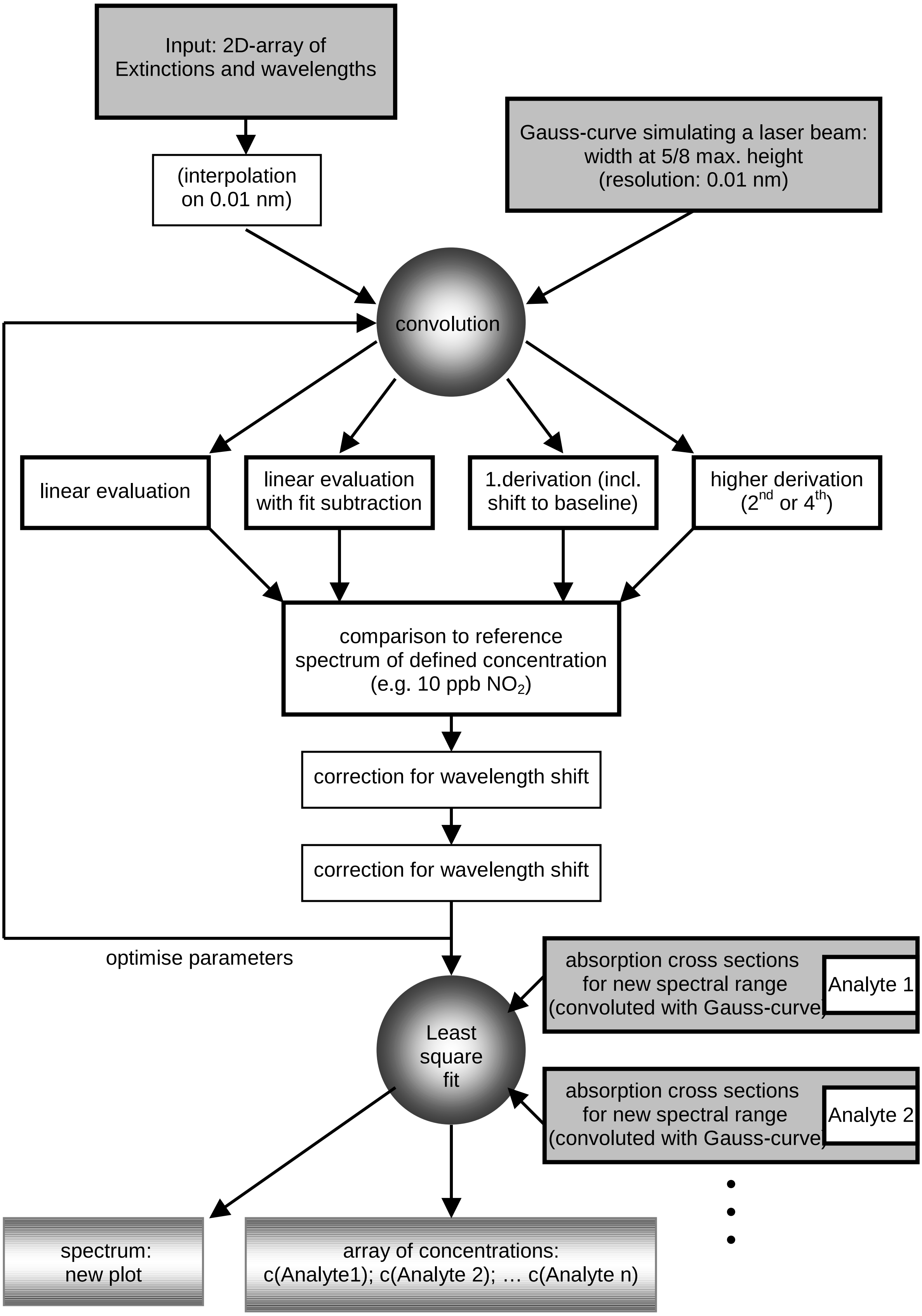

Fig. 2.15. Simplified scheme of the evaluation procedure

2.5.2. Example Spectra for Real Air Measurements

Two spectra from 23 Nov 2001 were selected in **Fig. 3.6.** as example demonstrating the spectral shape in dependence on the applied evaluation mode. Already in the plots of raw data measurements in **Fig. 3.6.a** two major peaks of NO_2 at 408.5 nm and 410.5 nm as well as a minor peak around 409.5 nm can be recognised. The predominant shape of the spectra mainly corresponds to the changing mirror reflectivity.

In **Fig. 3.6.b** the background spectrum obtained for pure nitrogen was subtracted. Due to the reasons discussed in Chapter **1.9.**, mainly aerosol influence and temperature effects, no even spectra results for which the extinction values are directly correlated to the real NO_2-concentration. Both spectra are shifted and reveal a tilted and slightly bent shape.

Hence, in **Fig. 3.6.c** the linear fit as well as the polynomial fit curve of each spectrum was subtracted from the respective spectrum. The same procedure was applied to the 10 ppb-reference-spectrum. The subtraction was performed after the smoothing step by convolution with a Gauss curve of 0.3 nm at 5/8 peak height. “Even” spectra are resulting from the fit procedure which are shifted to the zero-line and which can be evaluated by the least-square-fit method described in chapter **1.9.**. It can be seen, that in this case, i.e. this spectral range, the correction with a polynomial fit curve of 2nd order yields good results for air measurements, however, the reference curve is strongly bent.

A good approach in order to avoid aerosol and temperature effects is the evaluation of the derivative spectrum as done in **Fig. 3.6.d**. The big advantage of the application of higher derivations (**Fig. 3.6.e** and **Fig. 3.6.f**) is the renunciation of background subtraction as any influences causing shifts and tilting of the spectra are eliminated by this measure. However, especially the fourth derivation is very sensitive on slight wavelength irregularities within the spectrum and causes a larger amount of peaks. Thus, both example spectra had to be cut at one end. Higher derivation are only applicable to high-quality spectra obtained for perfect alignment and calibration of the device.

Concerning the concentrations determined by the evaluation procedure, a good agreement occurs between the values obtained for the non-derivative procedure and the values for the first differentiation (**Fig. 3.6.c** and **Fig. 3.6.d**). The same can be stated for the results obtained from the 2nd and 4th derivative (**Fig. 3.6.e** and **Fig. 3.6.f**), however, these values lie about 20% below the concentrations determined by the evaluation procedures of 0th or 1st derivative order. Hence, for comparison purposes a correction factor should be introduced.

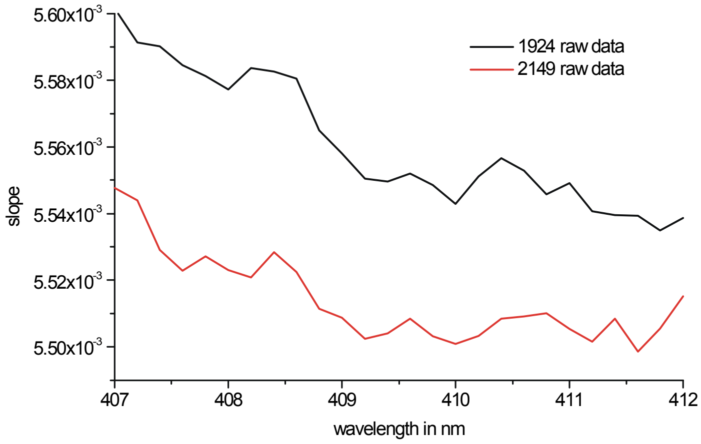

Fig. 3.6.a. Raw data of two selected spectra from 23 Nov 2001 (19:24 and 21:49). Scale of the y-axis is the measured slope of the CRDS decay signal.

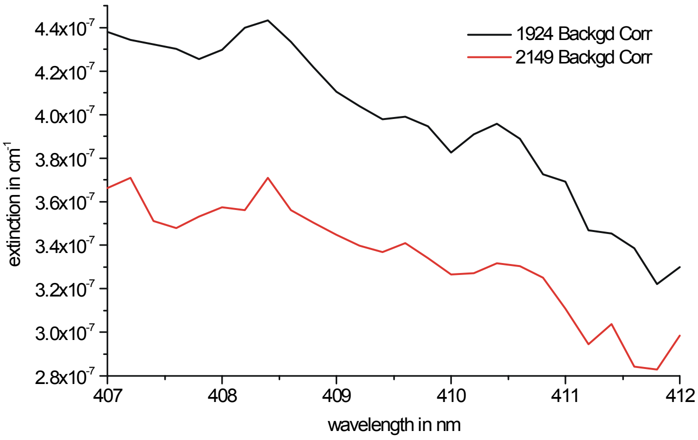

Fig. 3.6.b. Two selected **background corrected spectra** from 23 Nov 2001 (19:24 and 21:49). Scale of the y-axis is the extinction in cm^{-1}.

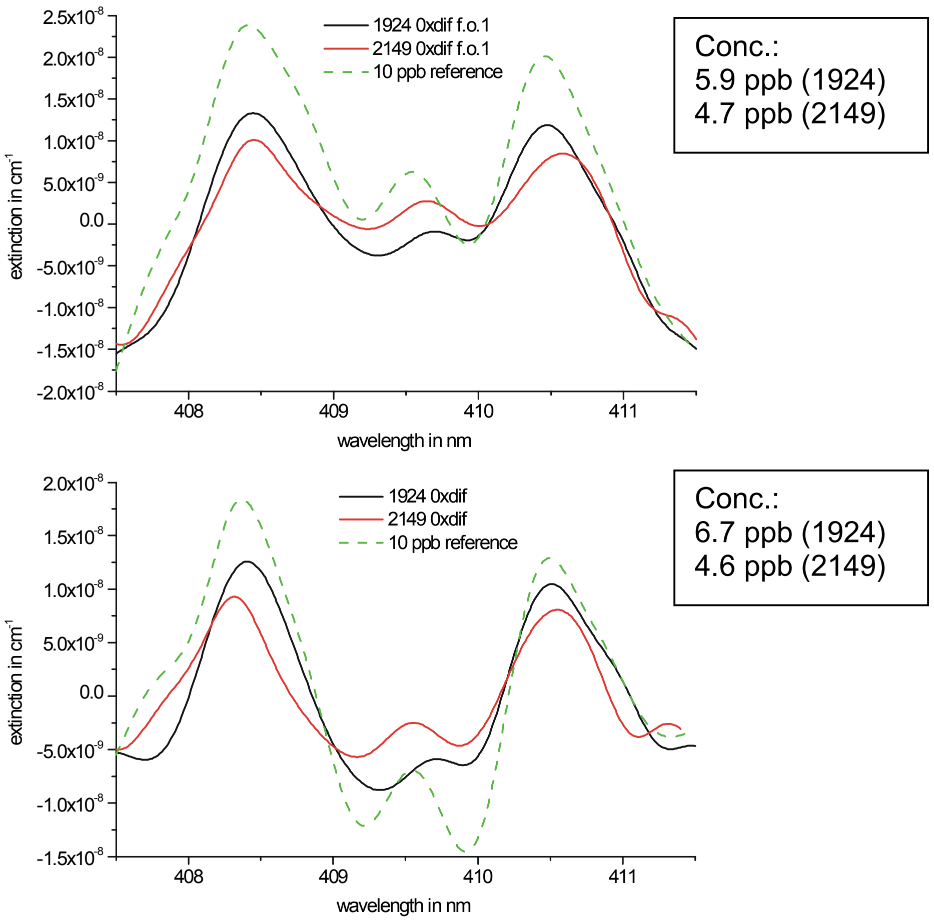

Fig. 3.6.c. Linear **non-differential** plot of two selected **background corrected** spectra from 23 Nov 2001 (19:24 and 21:49). Both spectra in the upper diagram are corrected by a 1st order (linear) fit, the lower spectra by a 2nd order polynomial fit curve. Measured concentrations: 5.9 ppb and 4.7 ppb, respectively (6.7 and 4.6 ppb).

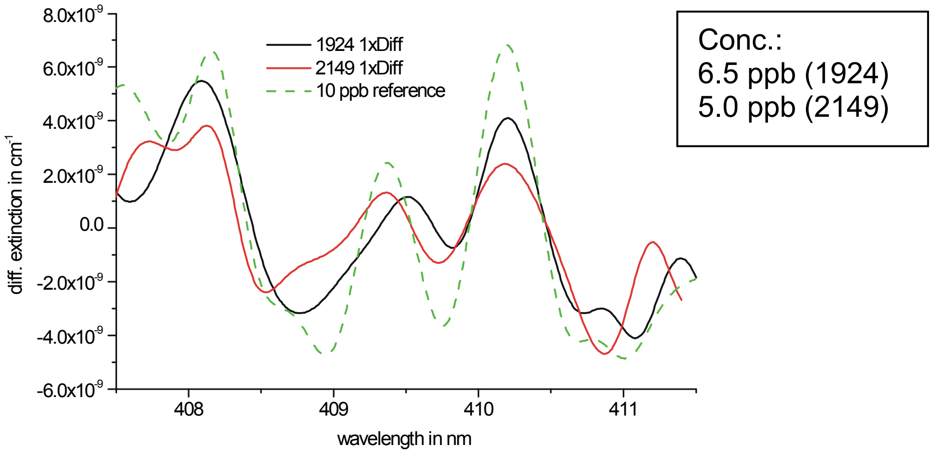

Fig. 3.6.d. Two selected **background corrected differential (1st order) spectra** from 23 Nov 2001 (19:24 and 21:49). Measured concentrations: 6.5 ppb and 5.0 ppb, respectively.

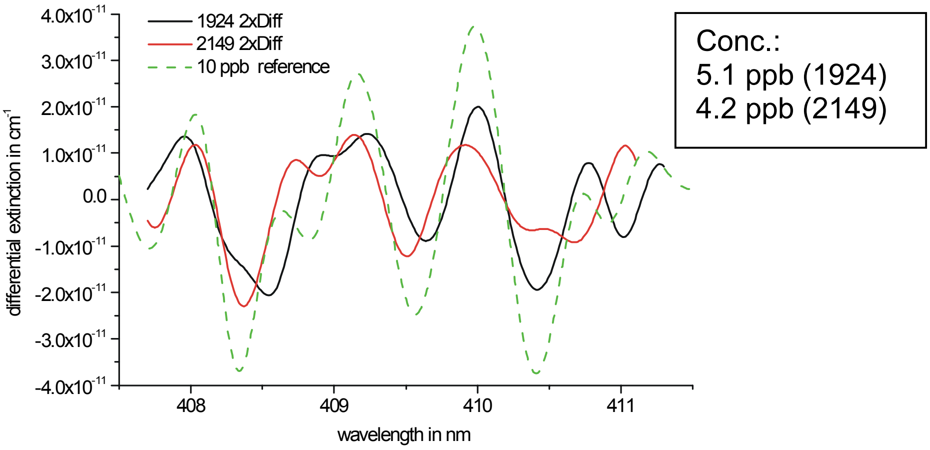

Fig. 3.6.e. Two selected **differential (2nd order) spectra without background correction** from 23 Nov 2001 (19:24 and 21:49). Measured concentrations: 5.1 ppb and 4.2 ppb, respectively.

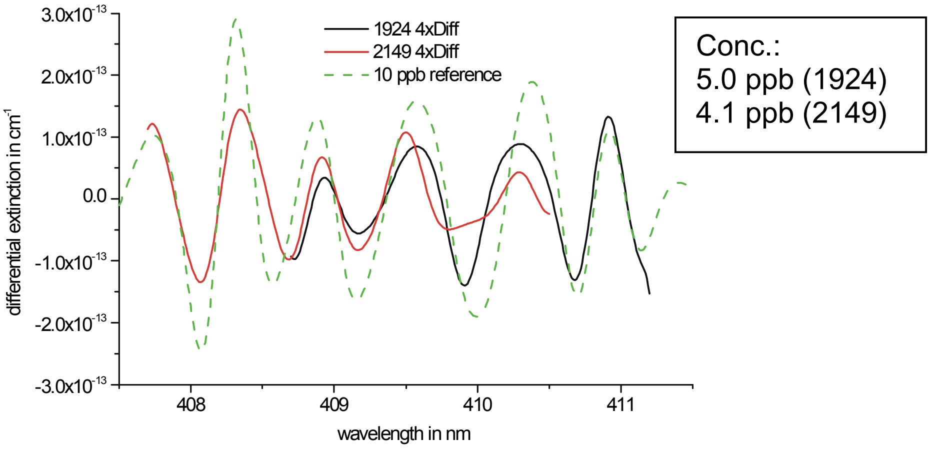

Fig. 3.6.f. Two selected **differential (4th order) spectra without background correction** from 23 Nov 2001 (19:24 and 21:49). Measured concentrations: 5.0 ppb and 4.1 ppb, respectively.

3. In-Situ Analysis of Ambient Air: Results

3.1. Laboratory Measurements

3.1.1. Reference Gas Spectra

First measurements performed with the device were realised in laboratory in order to characterise and to specify the different technical parts of the system. The **Fig. 3.1.** shows the very first absorption spectrum obtained for NO_2. To achieve this measurement in the 410 nm absorption band, a high concentration of 10 ppm was filled in the cell and the laser was tuned within a spectral resolution of 0.5 nm. The comparison of the retrieved absorption spectrum with the tabulated spectrum in literature (Merienne et al., 1995) shows a good agreement.

Example spectra for different dilution factors of 860 ppb standard gas in pure nitrogen are shown in **Fig. 3.2.**. The corresponding calculated concentrations are 8 ppb, 20 ppb, and 40 ppb. At the first glance a comparison with a 10 ppb reference spectrum from literature shows a clear underestimation of the experimental results. The same can be stated for the complete calibration curve discussed in the next section.

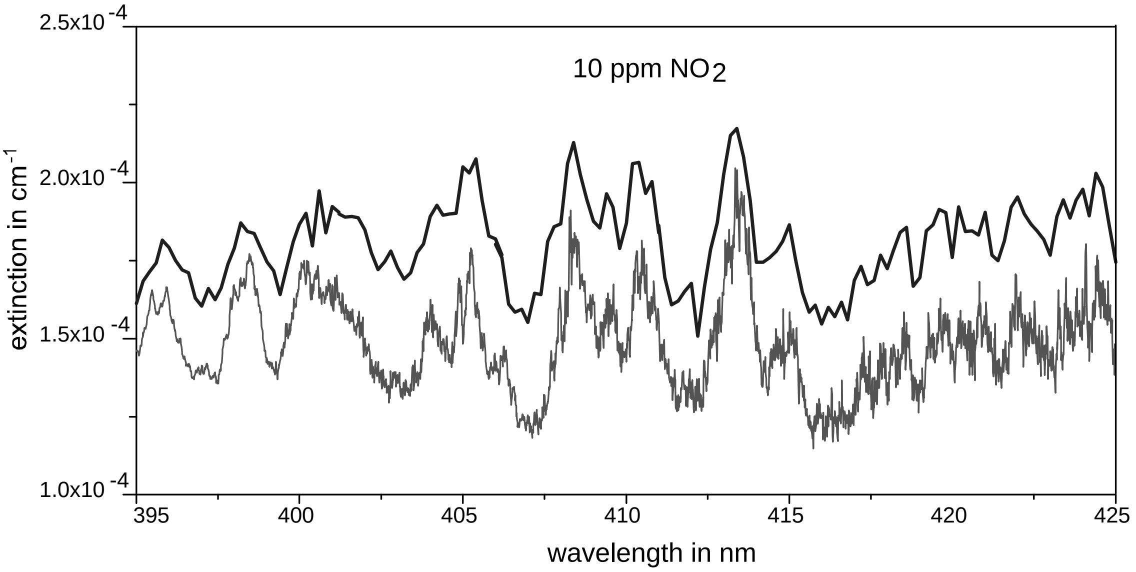

Fig. 3.1. Laboratory measurements of 10ppm NO_2 (upper line) in comparison with tabulated values (lower line) according to Merienne et al. (1995). The curves are shifted for more clarity.

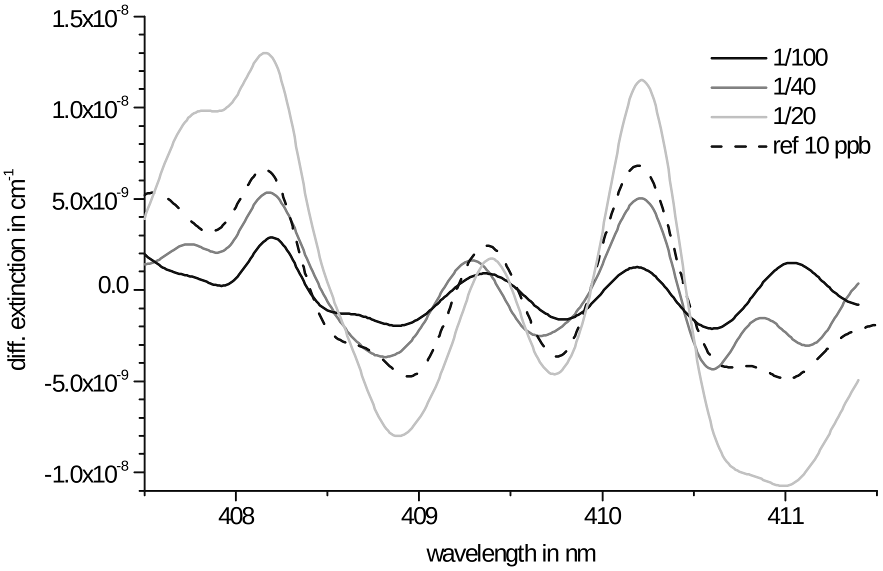

Fig. 3.2. Example of differential reference gas spectra for different dilutions of 860 ppb standard gas in pure nitrogen (8 ppb, 20 ppb, 40 ppb).

3.1.2. Calibration Curve

Reference gas measurements were performed with NO_2-standard-gas of the specified concentrations 0.86 ppm and 9.79 ppm, respectively. This standard gas was diluted using gas flow controllers and nitrogen providing N_2-atmosphere in the cell or, alternatively, a pure air generator and gas mixer streamed the cell by dry air.

For the maximum concentration 9.79 ppm the retrieval rate was about 95%, however, the accuracy of the measurement was reduced due to very high absorption in the gas measuring cell which lead to very short decay times (fit range not more than 1 μs). In the course of increasing dilution the retrieval rate was decreasing continuously: dilutions of 1:13 (9.79 ppm NO_2) revealed not more than 550 ppb or 73% instead of the nominal value of 750 ppb. Similar results and retrieval rates yielded the analysis of the full concentration of the gas bottle containing 0.86 ppm specified NO_2-concentration. In this case only about 600 ppb NO_2 were measured. From these two results it can be concluded that the gas flow controllers are functioning correctly on principle. However, it should be noted, that the specified standard gas concentration not only shows an error of 5%, but it also might have decreased a bit due to a long standing time of the gas bottle. The warranted stability amounts to 6 months only.

The retrieval rate is reduced to about 48% for concentrations around 100 ppb and keeps on decreasing to about 40% for low concentrations near the detection limit. **Fig. 3.3.** shows the calibration of the CRDS monitoring device for NO_2 measurements in the 400 nm absorption band. The calibration is NOT linear within three decades of concentration ranging between 1 ppb and 800 ppb. The detection limit reaches by 500 ppt.

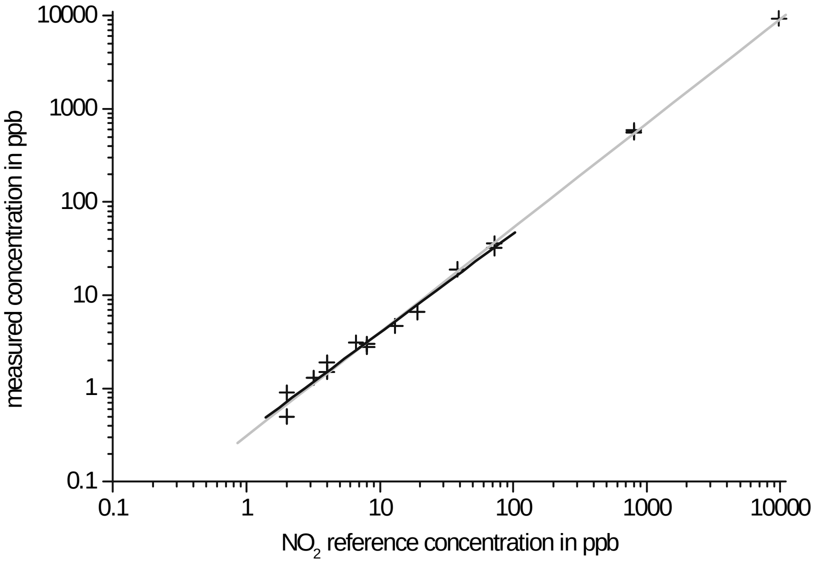

Fig.3.3. Calibration curve of the CRDS NO$_2$-monitoring device. Two linear fit curves are indicated: black is for lower concentrations only while grey includes deviating high concentrations. Notice: the double-logarithmic scale levels strong deviations.

Because of the very good coincidence concerning the shape between the derivated reference spectrum from literature and the experimental spectrum for the same concentration, severe errors caused by the evaluation procedure can be excluded (**Fig. 3.2.**). Values measured for standard gas were too low independently from the gas flow rate, hence, this parameter can not be the reason for the deviation either. The same can be stated for photolysis of the NO$_2$-molecule as measurements in several different wavelength ranges with different photolysis domains and characteristics resulted in very similar concentrations.

As can be seen in Chapter **1.3.** the photochemistry of NO$_2$ is rather complicated in the spectral range around 400 nm which is mainly analysed in this work. First, the strongly changing quantum yields for the photodissociation have to be taken into account and, second, the different compositions of the bath gas play an important role for NO$_2$-analysis.

Low concentrations (<100 ppb)

Analysis below 400 nm

For analysis below 400 nm the quantum yield for the photodissociation is almost 100% playing the main role in NO_2-photochemistry. In mere N_2-atmosphere as produced by dilution of NO_2 using flow controllers, the O-atom generated in the dissociation process can react with NO_2 lowering the nitrogen dioxide concentration of the standard gas in the measuring cell considerably. In contrast, by using a clean air generator for the production of NO_2-standard-gas, the O-atom will react with O_2 in order to form O_3. Additional regeneration of NO_2 can take place in ambient external air samples according to:

$$NO + O_3 \rightarrow NO_2 + O_2$$

$$NO + RO_2 \rightarrow NO_2 + RO$$

This can explain the very low NO_2-concentration measured by application of flow controllers for dilution compared to the reference concentrations (**Fig. 3.3**.) and real air analysis. Further minor reactions which are described in Chapter **1.3.** will have additional influences on nitrogen dioxide values.

Analysis above 400 nm

Measuring in the wavelength range 407 – 412 nm the photodissociation still must be taken into account as it is showing quantum yields between 0.24 and 0.10 having the effects described above. The main reaction, however, is the excitation of NO_2 to the longer lived excited states NO_2^*. As the quenching rate constants differ for different kinds of bath gases like N_2, O_2, and H_2O, further deviations for the measured NO_2 standard gas concentrations will occur depending on the gas composition in the cell. Hence, in this context it must be considered, that the quenching rate of N_2 is 10% below the quenching rate of O_2. The NO_2^* lifetime of about 1.4 ns for common total quenching rates under normal atmospheric conditions is much smaller compared to the cavity ringdown times which lie in the range of 10 µs. However, in pure N_2-atmosphere the lifetime of NO_2^* should be prolonged (no quenching: 30 – 200 µs, > ringdown time). Another reaction which might reduce the measured NO_2-concentration in mere N_2-atmosphere is the dissociation of doubly excited NO_2^{**} into O and NO with consequent reaction of O and NO_2 forming NO and O_2.

A further reduction of nitrogen dioxide content in any bath gas composition can occur by the reaction of NO_2^* with NO_2 as described by the reactions (16) and (17) in chapter **1.3.**.

Another reaction which can not be considered sufficiently in either reference gas measurement is the very efficient quenching of NO_2^* by H_2O. Due to the high quenching rate constant of water a very considerable quenching can be observed in spite of low water concentrations in air. In addition, interferences might occur by the production of HONO from NO_2^* and H_2O. This reaction is restricted to real air measurements.

Thus, a general underestimation of the measured NO_2-concentrations in cell must be taken into account with an additional underestimation in mere N_2-atmosphere.

High concentrations

In the case of very high NO_2-concentrations, i.e. the analysis of reference gas directly introduced from the gas bottles, the measured concentrations approximate to the real concentrations (860 ppb: 70%; 9.8 ppm: 95%).

This might be attributed to recombination effects. For low concentration the immediate recombination

$$NO + O + M \rightarrow NO_2 + M$$

of the photolysis products NO and O is hampered: after dissociation both particles move into different directions and it takes comparatively long time until they get the chance to recombine with another reactant to form NO_2 again. Meanwhile they have left the laser beam or the cell. In the case of high concentrations many dissociated molecules in the direct neighbourhood are available for fast recombination.

Similar recombination effects could occur to a lesser extent in the wavelength range above 400nm (and below 488 nm): The dissociation of facilely produced NO_2^{**} again yields NO and O with the same consequences as just discussed.

Measuring the full gas concentration of 860 ppb in the completely different wavelength range around 685 nm having two orders of magnitude lower absorption cross sections showed even more reduced results. The retrieval rate was only about 40% of the real value. At this wavelengths no two-photon absorption is thermodynamically possible (Crowley and Carl 1997) and NO_2^*(685 nm) will be the inactive end product with long lifetimes (estimated: several ns). The effects are comparable to the strong suppression of the O_2-band at 688 nm which is discussed in Chapter **3.2.**.

Further aspects

Interestingly, independent of the wavelength range and the differing photochemical processes, measurements below 400 nm (e.g. 394 – 403 nm, 366 – 373 nm) and measurements above 400 nm (407 – 412 nm, 425 – 431 nm) yielded approximately the same results. This indicates that the different processes counterbalance each other. Slightly higher values have been measured in the 370 nm range completely dominated by photodissociation.

A completely different aspect is the dilution of the NO_2-content in the cell by a minor N_2-stream coming from the mirror protection chambers. According to the portion of the N_2-chamber-length at the total cell length a reduction of the measured values by 11% should be observed, however, due to the rather large diaphragm holes (8 mm diameter) some deviations in the form of gas transfer in and out of this chambers might occur. Calibration measurements comparing the results obtained with and without mirror gas flow confirm the reduction to 89%.

For experimental NO_2-measurements with reference gases two different correction factors must be introduced, one for N_2-atmosphere (≈ 2) and another one for air from the clean air generator (≈ 1.2). The second value is very close to real air measurements (Chapter **3.3.**) in spite of water and aerosol effects. However, a big disadvantage of clean air generator and gas mixer are their bulkiness making them useless for some transportable set-ups. On the contrary, gas flow controllers are comparatively small and portable.

A way for the determination of a correction factor considering the deviations of NO_2-measurements in ambient air can be a comparison of big data sets obtained by the described CRDS-method with values of another well established method. Comparing 740 data points from ambient air CRDS-measurements in Berlin with the respective BLUME-values (Chapter **3.3.**) gives an underestimation factor of about 0.79, or 0.89 including the dilution effects of mirror rinsing. This could at least partially overcome the problem, that the standard calibration procedure does not consider interferences with other trace gases and aerosols.

Finally it should be mentioned, that the evaluation procedure can lead to a slight underestimation of the results, too. In this respect, a variation of the results depending on the applied procedure (degree of derivation, fitting and sifting process, convolution bandwidth) can be observed.

3.2. O_2-Measurements

In order to check a pair of Los Gatos Research mirrors with a specified maximum reflectivity at 690 nm (purchased for H_2O-analysis) the absorption band of molecular oxygen at 688 nm was analysed. As the results were intrinsic for the other CRDS measurement described in this thesis, they will be shortly specified in this section.

In addition to the absorptions in the ultraviolet, O_2 also has very weak absorptions in the red (762 and 688 nm) and infrared (1.27 and 1.06 μm), known as the atmospheric oxygen bands. They produce O_2 in the singlet excited states (singlet oxygen) $b^1\Sigma^+_g$ and $a^1\Delta_g$, respectively. The two bands 762 and 688 nm correspond to transitions to two vibrational levels, $\upsilon' = 0$ (762 nm) and $\upsilon' = 1$ (688 nm) within the $b^1\Sigma^+_g$ state. When $O_2(b^1\Sigma^+_g)$ and $O_2(a^1\Delta_g)$ are formed by energy transfer, O_3 photolysis, and exothermic chemical reactions they do not readily undergo radiative transitions to the ground state because the processes are forbidden. Thus the radiative lifetime of the $b^1\Sigma^+_g$ state is ≈ 12 s. As a result, when these electronic states are formed in the atmosphere, they are primarily collisionally deactivated to ground-state O_2. (Finlayson-Pitts and Pitts, 2000).

First measurements showed almost no peak in the spectral region of interest (**Fig. 3.4.a**) although the peak is very dominant in this range as can be seen in **Fig. 3.4.b**. It could be shown that two aspects are absolutely fundamental for the observation of this band and, evidently, for other bands as well. First, a gas flow has to be applied, i.e. the ambient air was pumped through the measurement cell. Second, an optical filter has to be installed in front of the PMT: in the case presented here, an interference filter (L.O.T. Oriel) with a central wavelength at 690 nm (691.8 nm, 8.7 nm at 50% maximum height) and, alternatively, at 700 nm (699.3 nm, 17.3 nm at 50% maximum height) were used. Obviously, some interference occur in the OPO output and therefore any measurement with this apparatus should be performed with an appropriate filter between exit mirror and

PMT. The new measurement considering the above mentioned two aspects revealed the upper curve in **Fig. 3.4.a** showing clearly the strong O_2-absorption band. However, the calculated O_2-concentration in air is ≈ 1% only. Possibly, the applied pump capacity (8 l/min) was not strong enough.

As conclusion it can be stated that O_2-measurements without pump are absolutely impossible. Obviously, the laser beam being reflected back and forth meets the same molecules at any reflection and those excited molecules which have lifetimes as long as 12 s do not absorb. The pump is able to remove the excited inert molecules to a certain extent.

It should be mentioned that the NO_2-concentrations measured in the spectral range around 685 nm are not influenced in the same way as O_2. Independently from the gas flow NO_2 was showing constant concentrations. The reason could be the much shorter lifetimes of excited NO_2 molecules with the consequence that the probability for the laser beam meeting an already excited molecule is much lower than for O_2. In addition, excited NO_2 still might absorb laser light to some extent.

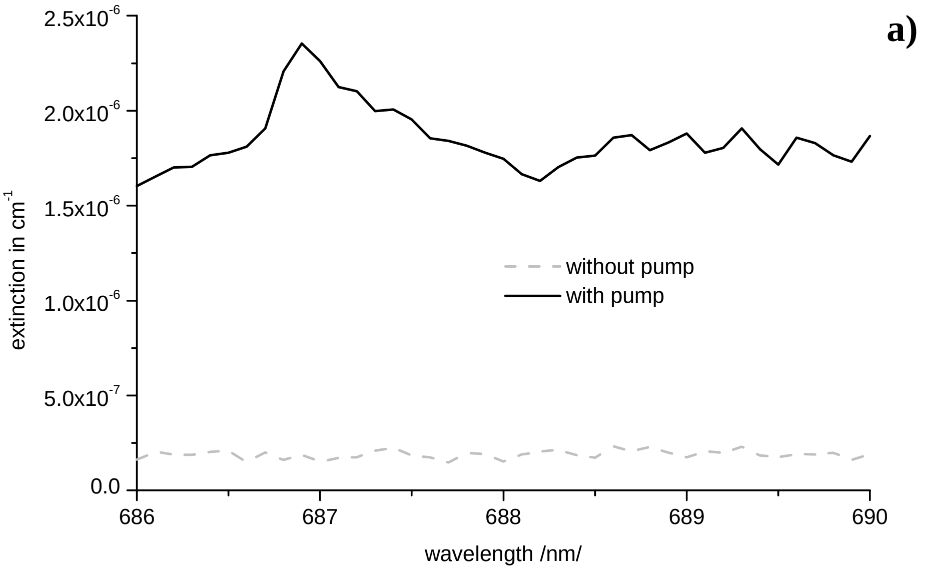

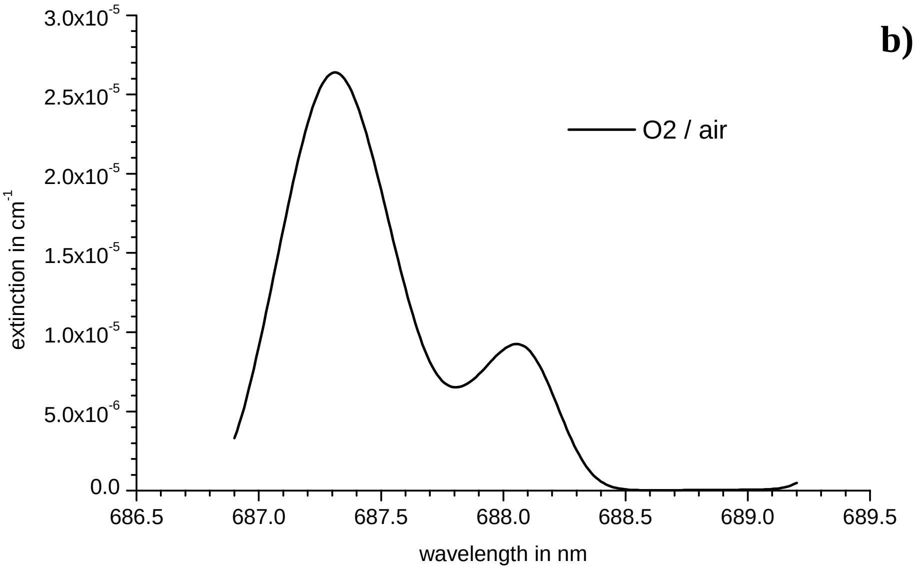

Fig. 3.4.a. Air/O_2 measurement with and without pump (08.01.02)

Fig. 3.4.b. Theoretical spectrum (Hitran96) of O_2 in air (21%), convolution 0.2 nm.

3.3. Berlin Measurements

Long-term external ambient air measurements were performed in autumn 2001 and winter 2001/2002 at the laboratory of the institute for air chemistry (BTU Cottbus) which is situated in Adlershof in the south-eastern suburbs of Berlin. The campus shows the characteristics of an suburban area.

3.3.1. Stations

The map in **Fig. 3.5.** shows the stations of BLUME (**B**erliner **Lu**ftgüte**me**ßnetz which means “Berlin air quality network”, translation of Blume ≡ flower) scattered over the city of Berlin and the location of the CRDS set-up at **BTU Cottbus** in **Adlershof**. The BTU-station is situated between two BLUME-stations of similar characteristics, the station **27 Marienfelde** and the station **85 Köpenick**. Hence, these two stations turn out to be ideal for comparison purposes. The NO_2-concentrations by BLUME were measured with conventional chemiluminiscence detectors and, furthermore, wind directions submitted by BLUME were regarded in the discussions.

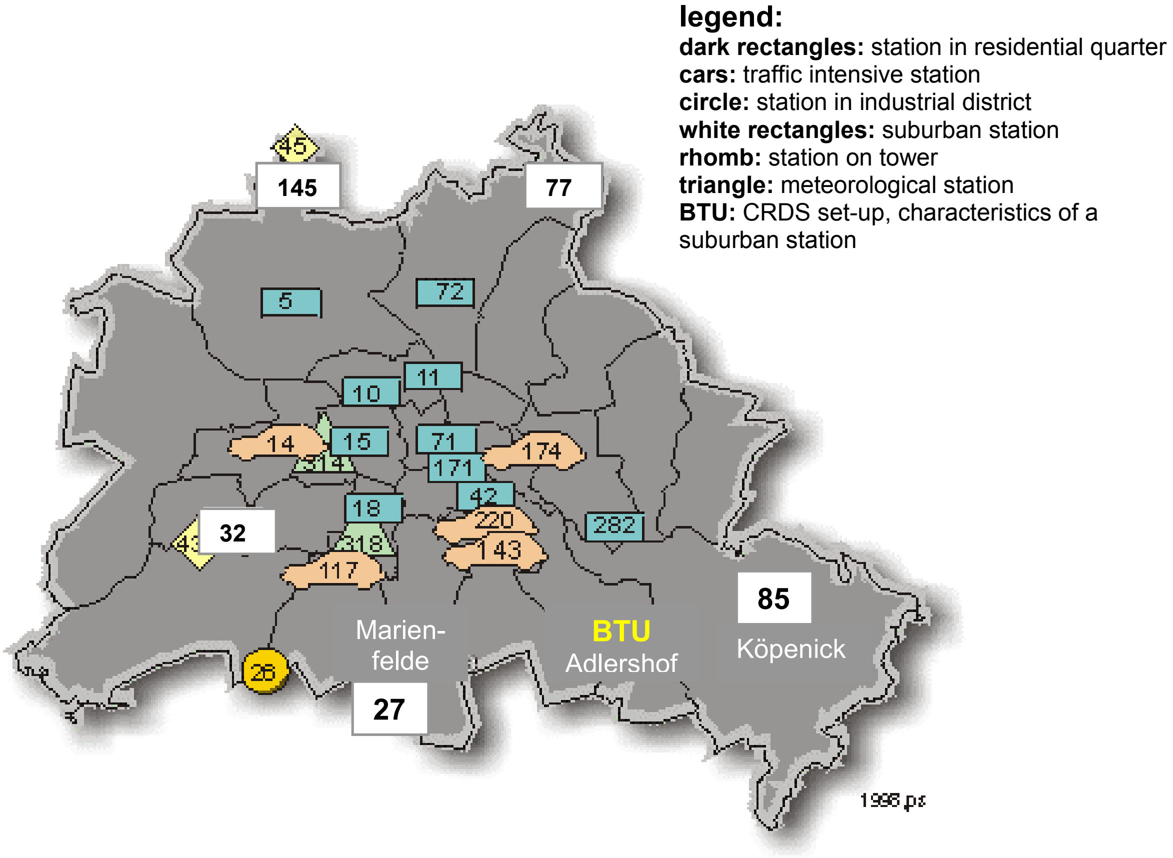

legend:
dark rectangles: station in residential quarter
cars: traffic intensive station
circle: station in industrial district
white rectangles: suburban station
rhomb: station on tower
triangle: meteorological station
BTU: CRDS set-up, characteristics of a suburban station

Fig. 3.5. Locations of the BLUME-stations. Adapted from BLUME (1996).

3.3.2. Time distribution of the Nitrogen Dioxide Concentration

Example spectra for real air measurements obtained during the “Berlin measurement” campaign in autumn and winter 2001/2002 were presented in Chapter 2.5. introducing the experimental concentration retrieval procedure. Any time distribution presented in the following section is based on spectra similar to those depicted in Chapter 2.5..

3.3.2.1. Wavelength Range 407 – 412 nm (Excitation Domain)

Longer-term curves

The evaluation of the following diagrams was performed by convolution of the first derivative of the spectra with a Gauss curve of 0.3 nm at 5/8 peak height as described in Chapter **1.9.**.

23.-26.11.2001

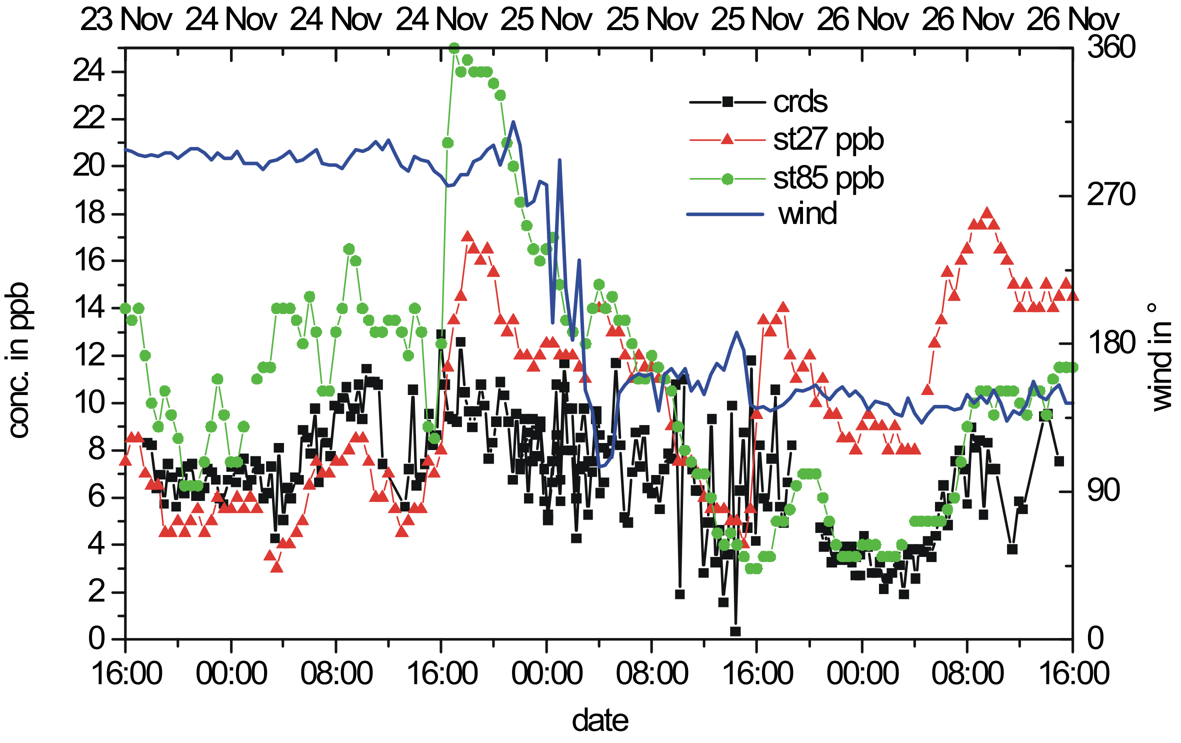

Fig. 3.7. Progress of NO_2-concentrations in the southern suburbs of Berlin between 23 Nov 01 and 26 Nov 01. Squares: CRDS BTU Cottbus. Triangles: BLUME station 27 Marienfelde. Circles: station 85 Köpenick.

Generally, the coincidence between the progress and the absolute concentrations of the CRDS- results and the BLUME-values is good, even minor peaks and sinks occur in any curve. An exception is the major peak at 18:00 on 24.11.01 which is only slightly pronounced in the CRDS-values. This peak is, precisely as the peak at 08:00 on 26.11.01, attributed to the rush hour. However, the main road concerning BTU Cottbus is situated in its north-east and, thus, the campus is less affected by westerly winds dominant during this period. As 25 Nov was a Sunday, the low NO_2-concentrations and the lack of major peaks can be explained easily. Exhausts by a motorway in the south-east of Marienfelde have easy access to station 27 and as motorways have a high traffic density also on Sunday afternoon due to excursionists, a well pronounced peak can be seen in the curve for station 27 at 16:00 (25.11). It is very interesting to see, how the two curves of station 27 (Triangles) and station 85 (Circles) are switching with the abrupt change in the wind direction from north-west to south-east. While the city of Berlin is situated in the north-west of station 85, in its south and a big lake (Müggelsee) can be found, two aspects which can perfectly explain the decline of the Köpenick-values. Compared to station 85 much less parts of the city lie in the north-west of station 27 leading to comparatively low NO_2-values.

Regarding the CRDS-values a remarkable increase in variation can be recognized starting at about 00:00 on 25.11.01 and reaching extreme extents before the gap at 19:00. This can be attributed to a continuous misalignment of the cavity due to mechanical and temperature effects. After a minor realignment during the “gap” in the diagram, the variation shows good values again. However, it can be stated that even during the period of the big variations at least the mean (preferably the gliding mean) shows good coincidence with the comparison values.

17.-19.12.2001

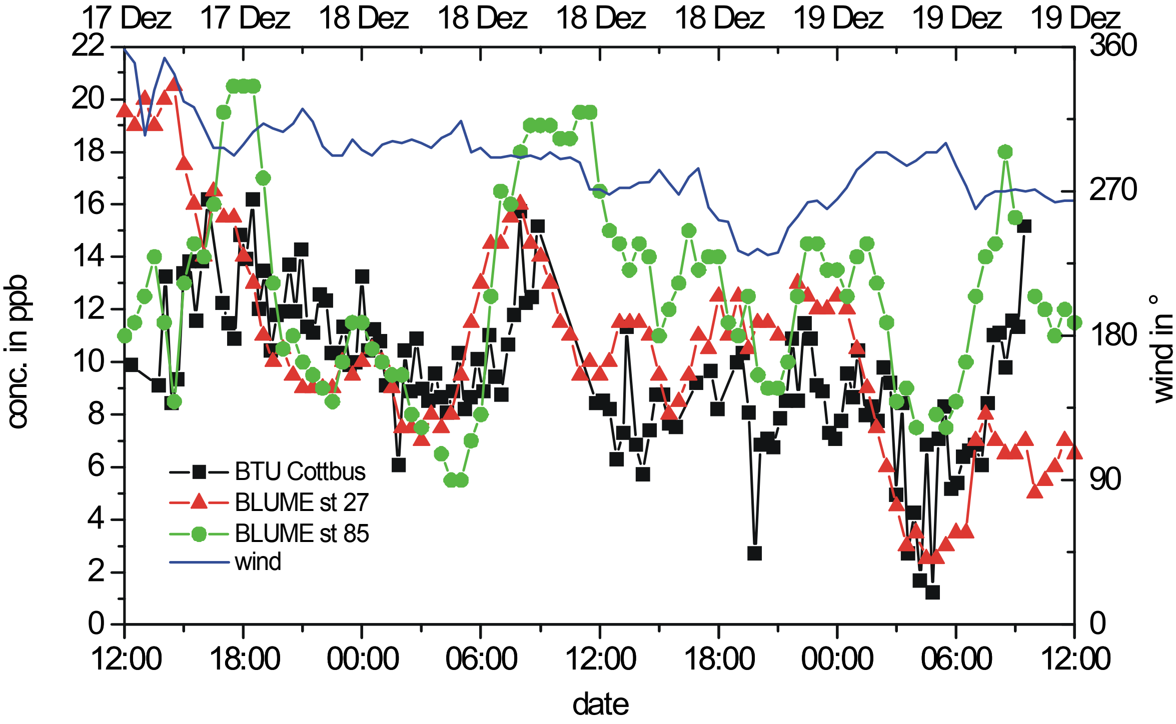

Fig. 3.8. Progress of NO_2-concentrations in the southern suburbs of Berlin between 17 Dec 01 and 19 Dec 01. Squares: CRDS BTU Cottbus. Triangles: BLUME station 27 Marienfelde. Circles: station 85 Köpenick.

Again the CRDS-measurements follow very well at least one of the two comparison curves showing the good capability of this technique to measure NO_2 in external ambient air. Even less distinct structures like e.g. the little double maximum around 00:00 on 19.12.01 are well represented in both the CRDS and BLUME-curves. Compared to the last diagram **Fig. 3.7.**, changes in wind direction are only slight: most time westerly winds remain dominant which is represented in the higher values of the concentrations measured by station 85 lying east from the city. However, the more the wind is coming from the north, the higher are the values from station 27 culminating in a peak in the very beginning of the progress. As can be seen from the map in **Fig.3.5.**, Marienfelde (27) is situated directly south of the city centre.

21.-23.12.2001

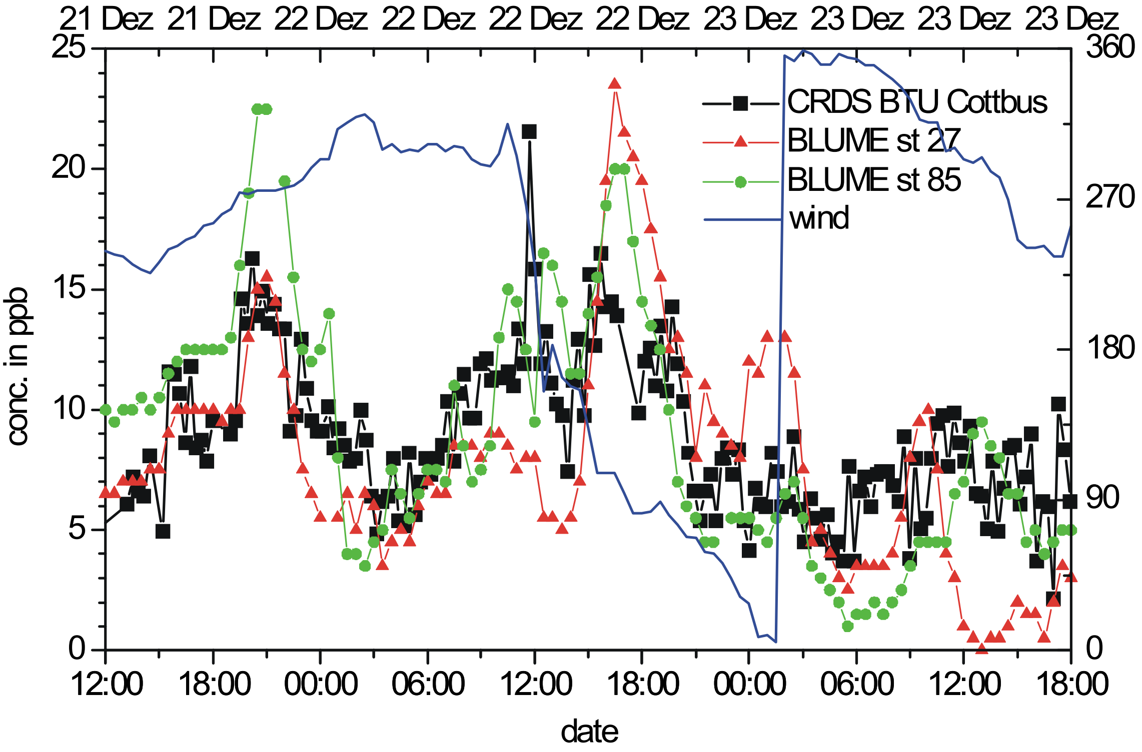

Fig. 3.9. Progress of NO_2-concentrations in the southern suburbs of Berlin between 21 Dec 01 and 23 Dec 01. Squares: CRDS BTU Cottbus. Triangles: BLUME station 27 Marienfelde. Circles: station 85 Köpenick.

Rush hours are well indicated in **Fig. 3.9.** by the peak around 20:00 on Friday 21.12. and the peak at 17:00 on Saturday 22.12.. Once again, Sunday 23.12. was quiet showing no rush peak. Westerly winds made the peak vanish which dominated the Sunday-curve from station 27 in **Fig. 3.7.** and which was attributed to the motorway in the south. It can be seen that the concentrations measured by CRDS never reach very small values as there is always some background concentration caused by the nearby main road “Adlergestell”. There was a rapid 360°-turn of the wind direction which could hardly be followed by the exhausts: e.g. during the short period with southerly winds the values measured at station 85 (remember the large lake in the south) still kept high levels. Possibly the wind speed was too low, however, data for this parameter were not available.

Additional shorter-term curves

Two more shorter-term curves which also were regarded closely for the verification of the evaluation are presented in **Fig. 3.10.** and **Fig. 3.11.**. In **Fig. 3.11.** clearly dominating northern winds are causing constantly enhanced values at station 27 situated directly south of the city. A look at the city map reveals rather identical conditions for Köpenick and Adlershof (BTU) in respect to north winds and, hence, the results are almost identical. Unfortunately, a failure of the device at station 85 caused the loss of data until 10:00 on 12 Dec. Interestingly, the little turn of the wind direction towards the east around 16:30 (12 Dec) immediately causes a decline in the progress measured at station Marienfelde. Again, the dominant main peak can be attributed to the morning rush hour. Obviously, the variation of the CRDS-values is comparatively high, however, at least the gliding mean (over 3 points) indicated in the diagram shows a good coincidence with the comparison values.

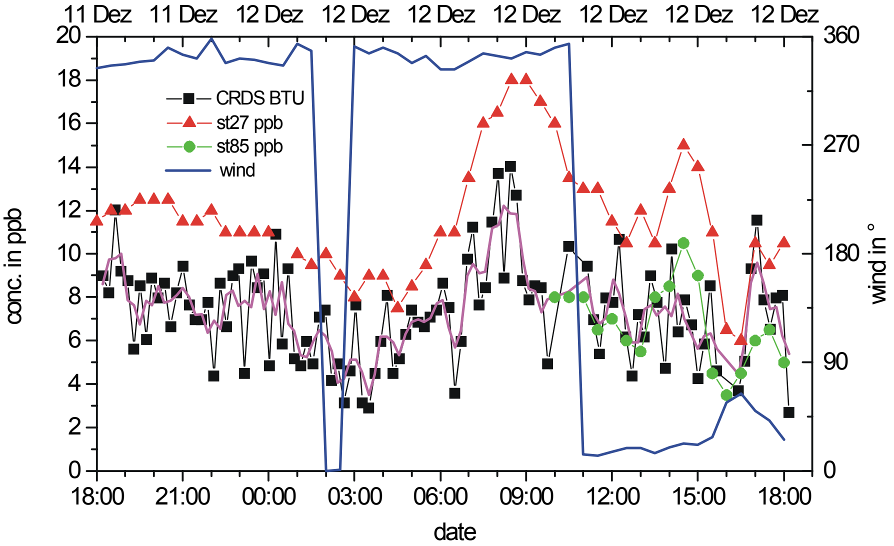

Fig. 3.10. Progress of NO_2-concentrations in the southern suburbs of Berlin between 11 Dec 01 and 12 Dec 01. Squares: CRDS BTU Cottbus. Triangles: BLUME station 27 Marienfelde. Circles: station 85 Köpenick.

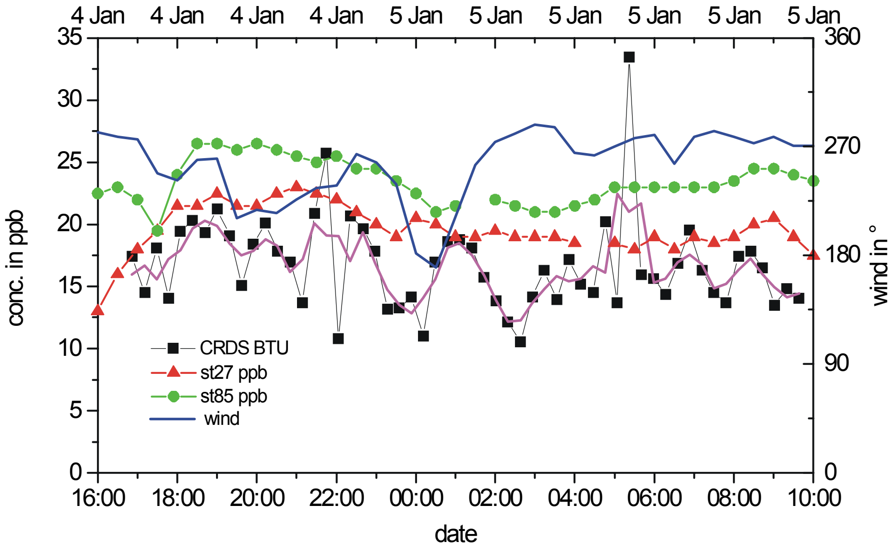

Fig. 3.11. Progress of NO_2-concentrations in the southern suburbs of Berlin between 04 Jan 02 and 05 Jan 02. Squares: CRDS BTU Cottbus. Triangles: BLUME station 27 Marienfelde. Circles: station 85 Köpenick.

Overall high NO_2-concentrations and the lack of major peaks caused by rush hours are the prominent features in **Fig. 3.11.**. Presumably, the high concentrations level these structures. With the city of Berlin situated in the west of station 85 the main wind direction provides this sampler with enhanced values compared to station 27. A temporary turn of the wind to the south causes a relative sink in the curve of the Köpenick station 85 while the otherwise low CRDS-values show a little peak at this point probably caused by the motorways and Schönefeld Airport south of Adlershof. The variations of the CRDS-results are rather big in this diagram: the reason can be found in the fact that these measurements were performed at the end of an about four months long period without major readjustment and recalibration of the laser system. However, the results are still of satisfying quality.

3.3.2.2. Other wavelength ranges (dissociation domain)

The example in **Fig. 3.12.** shows results for the different wavelength range 394 – 403 nm. While the first evening rush hour peak, as observed in most of the previous examples, is less distinct for CRDS compared to BLUME-results, the second maximum is very prominent in the case of the new technique. The rare SE-winds transport exhausts from the nearby traffic junction in Grünau and maybe Schönefeld Airport to Adlershof. The different peak height of the two maxima concerning CRDS-values might be attributed to a change in wind strength. All in all no significant difference occurs compared to previous results obtained for a wavelength range dominated by excitation rather than dissociation.

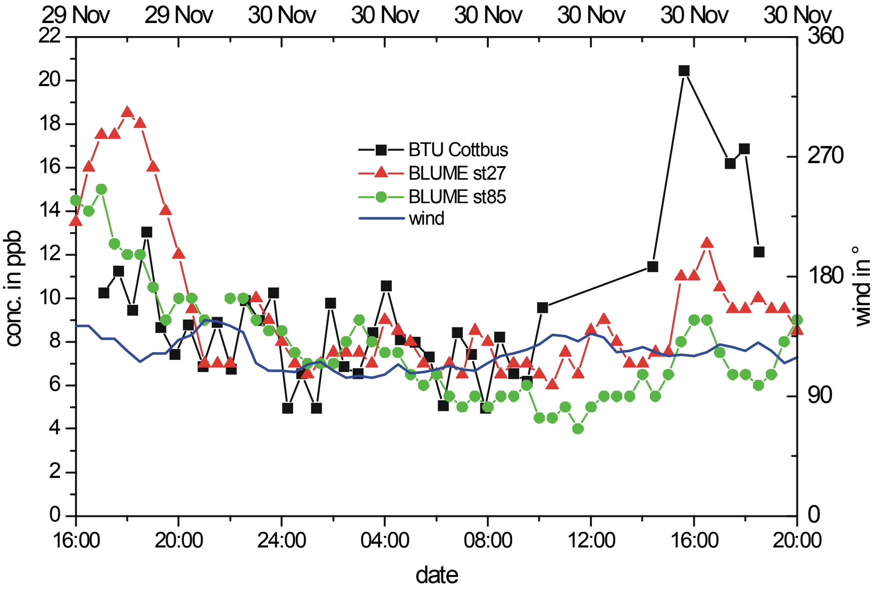

Fig. 3.12. Progress of NO_2-concentrations in the **wavelength range 394 – 403 nm** between 29 Nov 01 and 30 Nov 01. Squares: CRDS BTU Cottbus. Triangles: BLUME station 27 Marienfelde. Circles: station 85 Köpenick.

In contrary to any diagram discussed above, the following two diagrams obtained in the wavelength range 366 – 373 nm were not analysed via the first derivation but in a linear manner in order to elucidate the HONO-contribution in a better way. Furthermore, the stronger variation of the results involves the generation of artificial peaks while performing a derivative analysis.

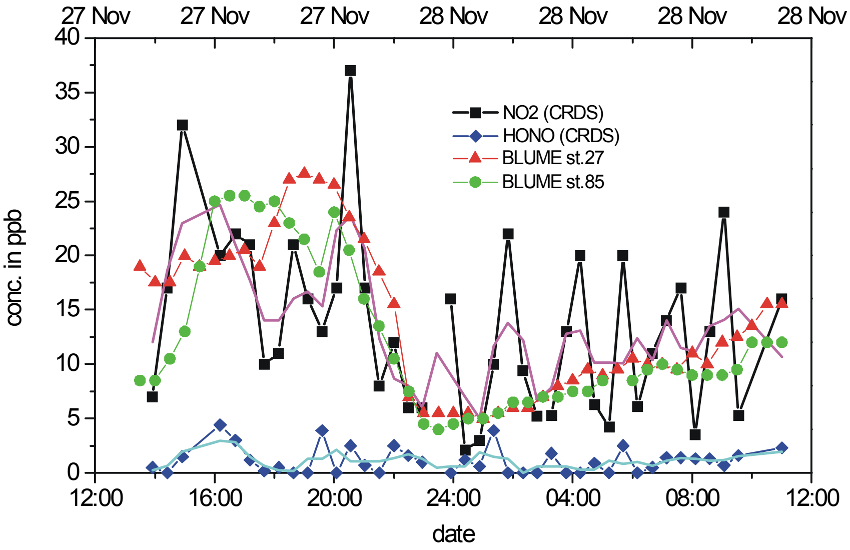

Fig. 3.13. Progress of NO_2-concentrations in the **wavelength range 366 – 373 nm** between 27 Nov 01 and 28 Nov 01. Squares/ Rhombs: CRDS BTU Cottbus. Triangles: BLUME station 27 Marienfelde. Circles: station 85 Köpenick.

Despite of the big variation in the individual point measurements caused by strongly deteriorating mirror reflectivities in the spectral range 366 – 373 nm, the progress of the NO_2-concentrations is very well reflected in the course of the BLUME-values. However, this coincidence becomes only visible after smoothing with a gliding mean over the single values. Even delicate structures like the secondary maximum at 20:00 on 27.11.01 (BLUME-results for station 85) can be confirmed. HONO-results indicated in **Fig. 3.13.** will be discussed in the next section.

Fig. 3.14. is added in order to show the limitations of the CRDS-technique. The depicted results were obtained with unfavourable mirror reflectivities at the end of the long-term measurements of several months duration. The variation is still very high although the convolution was made with a Gauss curve of 0.5 nm at 5/8 peak height for better smoothing. Obviously, it is hard to find coincidences between CRDS and BLUME results. An evaluation in respect to HONO did not reveal conclusive results.

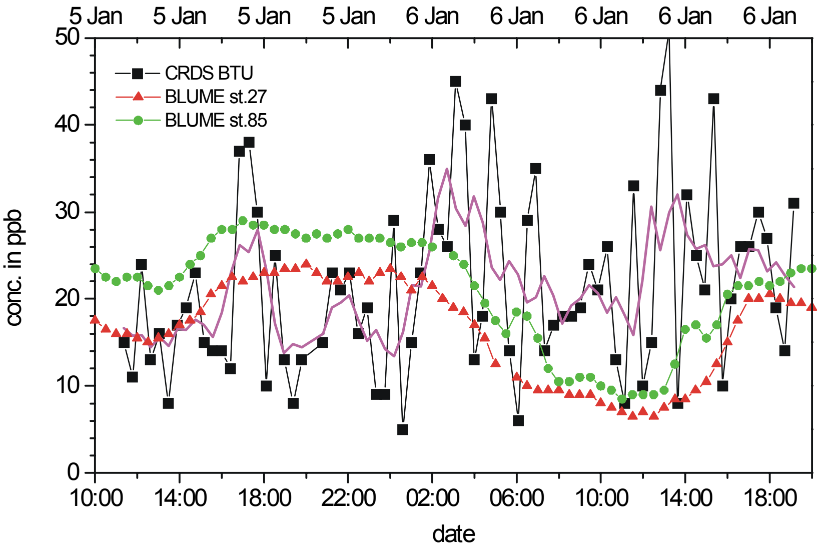

Fig. 3.14. Progress of NO_2-concentrations in the **wavelength range 366 – 373 nm** between 05 Jan 02 and 06 Jan 02. Squares: CRDS BTU Cottbus. Triangles: BLUME station 27 Marienfelde. Circles: station 85 Köpenick.

Resume

Looking at 740 good quality measuring points and comparing them with the values determined by BLUME for the entire periods it can be seen that the overall average of the CRDS-results lies about 12% below BLUME. Although for a big amount of data the entire means should approach each other, real atmospheric features caused e.g. by the position of the sites with predominantly lower values at Adlershof can not be completely excluded. Additional aspects being able to reduce the measured CRDS-values can be based on photochemical and photophysical processes as described in Chapters **1.3.** and **3.1.** and on a general underestimation caused by the evaluation procedure. For a sufficiently large amount of data, a general correction factor for atmospheric CRDS-measurements can be introduced. Based on the results of this work this factor is 1.13, however, it could be improved by any further measurements. As severe problems occur in calibration measurements with standard gases based on different bath gas compositions in the cell and by multiple photochemical and photophysical processes depending on the applied wavelength range (chapter **3.1.**), the establishment of a well-defined experimental correction factor might be a very good solution.

Concerning the maintenance of the set-up during longer-term measurements, it can be stated that a daily quick-check is sufficient. Normally a rapid cavity realignment at the two screws of the input mirror holder will suffice. After 4 –7 days it will be necessary to clean the dielectric mirrors with absolutely water-free acetone. However, the calibration of the OPO should be stable for the duration of weeks and even more robust proofed to be the Nd:YAG pump laser running reliable for at least several months.

3.3.3. Time distribution of the Nitrous Acid Concentration

With the set of mirrors applied (HR @ 390 nm) the HONO-measurements have to be performed at the 368 nm absorption band of HONO. The band at 384 nm is too less distinct and for the other bands at shorter wavelengths (354 nm, 342 nm, see **Fig. 1.5.**) another pair of mirrors has to be used. However, measurements and evaluation already have to be performed near the mirror transmission edge with steeply decreasing reflectivities resulting in high slopes of the CRDS-raw-signals and big noise in the values. In order to elucidate the HONO-contribution in the best way the spectra were evaluated without differentiation as described in chapter **1.9.**.

27./28.11.2001

As depicted in **Fig. 3.13.** rather high HONO-values were obtained during high NO_2-conncentrations around 16:00 on 27.11.01, however, this HONO might have been produced in the long PFA-tube of the gas inlet system. Regarding the fundamentals of atmospheric chemistry and photochemistry, at this time of the day no HONO should occur, especially as the night was rainy. This is different for the constant values and the increase after 06:00 on 28.11.01. (example spectra: **Fig. 3.15.**) which indeed might be a hint for some atmospheric HONO.

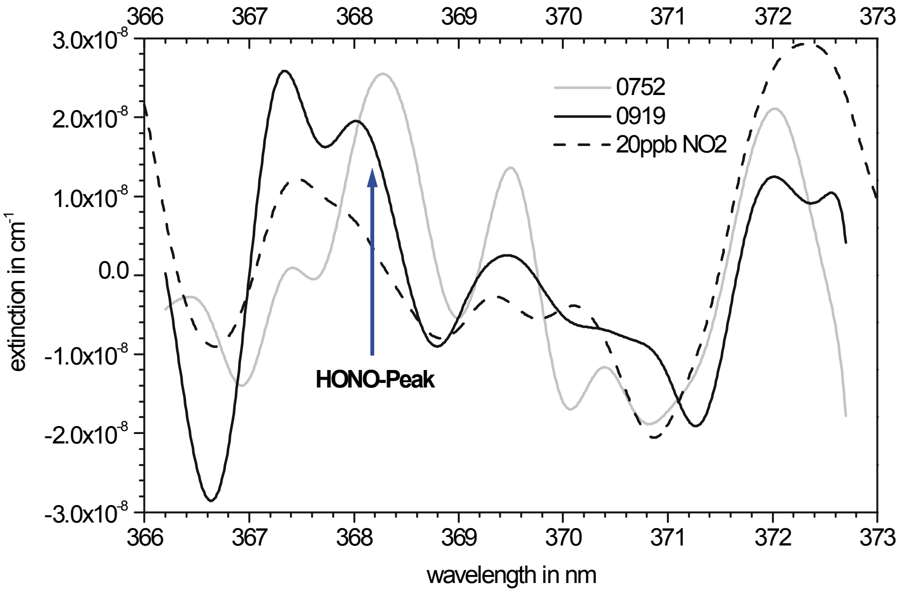

Fig. 3.15. Two example spectra for the possible detection of HONO during the period indicated in **Fig. 3.13.** (27./28.11.2001). The time of the spectra is 07:52 and 09:19, respectively.

20./21.12.2001

Measurement on 20./21.12.01 were performed during snowfall: showing between 3 and 12 ppb, the HONO-values are obviously very high or even too high for normal atmospheric contents. HONO might have been produced on the snowflakes and/or in the gas inlet system.

05./06.01.2002

These measurements were performed with a less good alignment and adjustment of the experimental system which is represented in less good raw data quality: the measured slopes of the CRDS-signals at 369 nm were 0.0212 compared to 0.0170 on 27./28.11.01. This is directly represented in very big variation of the single points and a very bad coincidence with the BLUME-values. However, as NO_2-concentration were very high, at least some experimental spectra showed a very good coincidence with the reference spectrum. Remarkably, even for high NO_2-concentration no HONO-contribution was clearly detectable.

Resume

With the applied set of mirrors reasonable HONO-analysis is very hard to perform due to insufficient reflectivities around 368 nm. However, at least some indications and results on HONO could be obtained and, in addition and even more important, a suitable evaluation method for HONO was worked out. With another pair of mirrors with HR @ 354 nm routine analysis of HONO should be possible in the 354 nm – band, and as a very interesting and important side effect HCHO-analysis should be within the realm of possibility. Regarding the values of NO_2 it could be shown that reasonable results can be obtained for CRDS-signal-slopes better than 0.02. However, really detailed HONO-analysis require a HONO-generator which is able to produce standard gas of defined concentration. A suitable apparatus based on the reaction of gaseous HCl with solid $NaNO_2$ is described by Febo et al. (1995) and Stutz et al. (2000).

As an ideal solution applicable in CRDS, an open cavity will avoid HONO-production within the device and, especially, the tubes. It could be the very best system for in-situ HONO-detection as no other system can renounce those tubes.

3.4. Field Measurements

After laboratory tests and outdoor measurements, the device was field tested during one week in October 2000 on the “Kleiner Feldberg” hill near Frankfurt am Main in Germany. The hill is located at an altitude of 825 m and it is distant of 30 km in the North-East direction from the German stock city Frankfurt. The measurements were performed in the framework of the FELDEX 2000 campaign organised by the “Zentrum für Umweltforschung” (ZUF, Centre for Environmental Research) at the University of Frankfurt under the hospice of the German Foundation for Environment (DBU, Osnabrück, Germany). This campaign was dedicated to the inter-comparison of new developed atmospheric monitoring devices. Because the aim of the campaign was to settle the detection limits and operation deficiencies of the device, rather than the study of the photochemistry, performing such an experiment during the autumn period was beneficial.

The CRDS device was implemented in a monitoring van (**Fig. 2.8.**) allowing point measurement at a height of four meters above ground level. The device was set to monitor NO_2 and HONO. Both compounds were quasi simultaneously monitored by measuring absorption spectra in the 367-412 nm spectral range within a 10 minutes cycle. More optimised measurements concerning special parameters like e.g. PMT-voltage, which is connected to variations in mirror reflectivity, were done in the range 366 – 372 nm concentrating on HONO and in the range 407 – 412 nm regarding NO_2. For a better direct comparison of mere NO_2-results with values obtained from multi-element-analysis in the 366 – 372 nm range some more measurements were done at 374 – 379 nm. Data acquisition and fast on-line evaluation were simultaneously performed.

The suitability of the set-up for NO_2-analysis is shown in **Fig. 3.16.** which depicts the spectrum of 10 ppb NO_2 in clean air. Obviously the retrieval rate is much higher compared to measurements in pure nitrogen atmosphere (**Fig. 3.2.**, chapter **3.1.**) reaching 8.9 ppb or 89%.

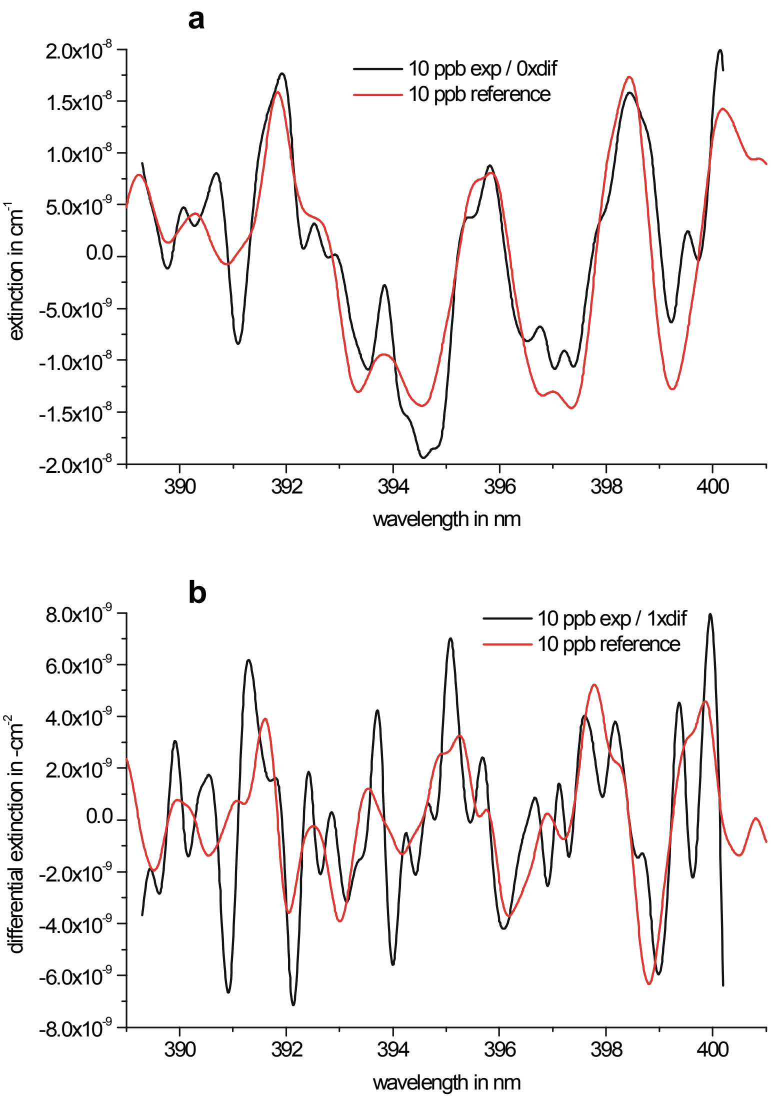

Fig. 3.16. Section of a 10 ppb NO_2 (in pure air) spectrum from 367 to 402 nm. The upper spectrum **a** was analysed in non-differential mode, the shift to the baseline was performed by subtracting the linear fit. The lower spectrum **b** was evaluated via its 1st derivative. Measured analyte concentration: 8.9 ppb (linear) and 8.3 ppb (differential).

An example for real air measurement is plotted in **Fig. 3.17.**, the spectral range of HONO absorption. The analysis was performed in a non-differential mode in order to elucidate the HONO-contribution to the total spectrum as good as possible. Evaluating the spectrum by multi-elemental-analysis gives 7.6 ppb for NO_2 and 0.9 ppb for HONO. However, the result for HONO should be regarded with caution for several reasons: First, in late afternoon (17:32) high HONO-concentration are unlikely as stated in Chapter **1.2.** and it must be assumed, that the measured HONO was at least partially produced in the apparatus, especially in the PFA-inlet-tube. Second, the measurements were performed near the limit of acceptable mirror reflectivities and, consequently, uncertainties and noise are enhanced. This can be seen in the quite odd shape of the HONO-peak being a bit too pointed. Interestingly, the measured slopes of the CRDS decay curves (which are directly correlated to extinctions) showed values which were not attained during further investigations like the “Berlin measurements” in Chapter **3.3.**. Values as good as $1.4 \cdot 10^{-5}$ cm^{-1} were obtained at 366 nm. Consequently, it has to be assumed that the mirror reflectivity has deteriorated over the time. Unfortunately not all measurement parameters (chapter **2.2.**) were optimised at this stage of the experiment. For instance the “shot selection” was introduced later and thus it could not be extracted the optimum from this experiment.

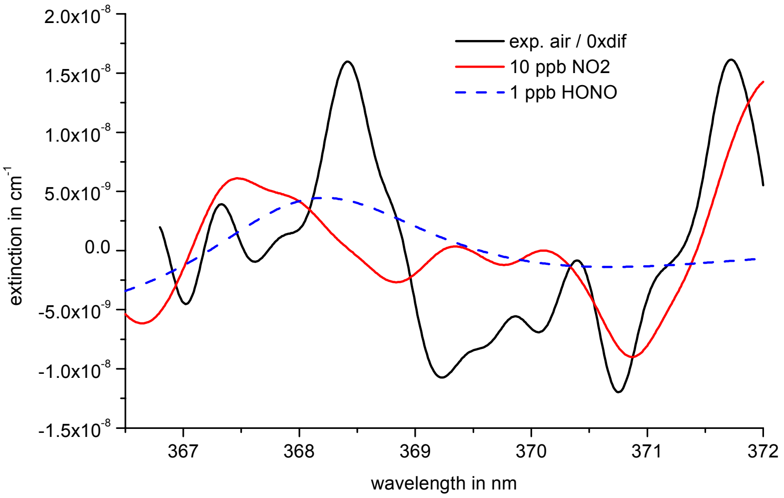

Fig. 3.17. Example of a real air spectrum in the range 366 – 372 nm from 10.10.00 17:32. The spectrum was shifted by the linear fit mode. Concentrations: NO_2 7.6 ppb; HONO 0.9 ppb.

The time evolution of the concentration of the traces is depicted in **Fig. 3.18.**. The values indicate 1/2 hour averaged concentrations. In this diagram error bars are included which were omitted in the other figures of this thesis in order to improve the clarity of the presentation. Their dimension were estimated to about 10% according to the discussion in the next section **3.5.**. The measurement has been continuously performed during three days where lacks of data are related to calibration deficiency and power supply failures. The NO_2 concentration is rather low until October 12, which is related to rainy and foggy weather with high variations of wind velocity and direction. However, the meteorological situation has changed after this period, whereby wind was blowing from the South and South-West direction. The correlated increase in NO_2 concentration could describe air masses coming from the Frankfurt city-plume and the surrounded region.

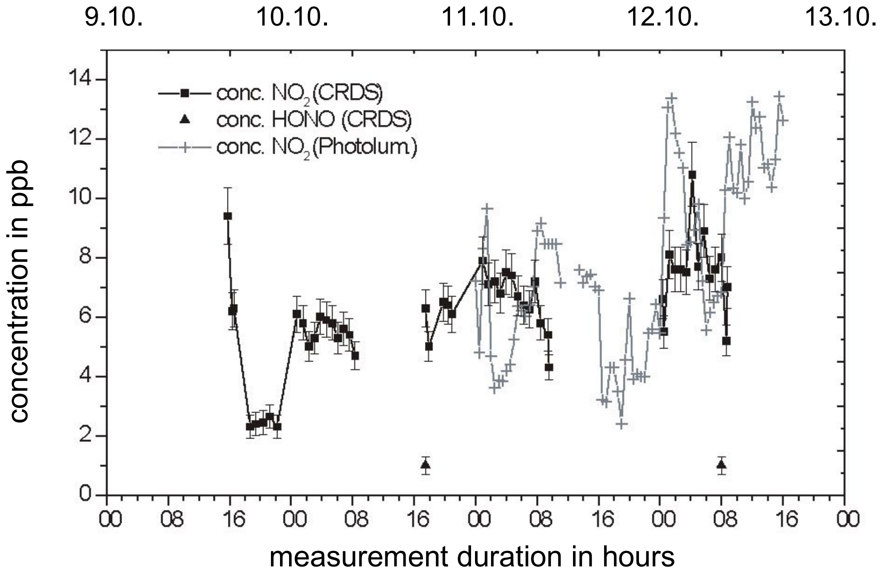

Fig. 3.18. Progress of NO_2 (and HONO)-concentrations between October 09 and October 12 of 2000 on “Kleiner Feldberg” hill near Frankfurt am Main, Germany. Data are ½ hour averaged concentration. Detection limits of CRDS NO_2/HONO measurements : 0.5 ppb, 10% accuracy.

The HONO concentration is only given for two periods because the monitored value were below the 500 ppt detection limit. Moreover such high concentration is quite rare with the weather condition. These two high 800 ppt HONO concentrations should be related to the setup of the air inlet which was 4 m long leading to HONO production in the inlet under high air humidity condition. This points out that the inlet configuration with a small monitoring cell is not appropriated for the monitoring of radicals.

The **Fig. 3.18.** also depicts the blind comparison between the NO_2 measurement performed with the CRDS device and the standard device based on photoluminescence (University Wuppertal). The mean values of the concentrations are in a good agreement but several data lay within a difference of a factor 2. Those discrepancies rely to the atmospheric aerosols content, because during the campaign, filters were not mounted in the air inlet of the CRDS device. The different location of the air inlet used by the devices could also account for these discrepancies.

3.5. Errors and Detection Limits

3.5.1. Theoretical Detection Limits

Detection limits based on simulations for a mirror reflectivity R = 99.99% and tabulated absorption cross section differences are listed in **Table 1.2.** (Chapter **1.10.**). The values are 100 ppt for NO_2 and 80 ppt for HONO, respectively.

3.5.2. Experimental Detection Limits

3.5.2.1. Ambient Air (Environmental samples)

@ 410 nm:

The standard deviation of the measured extinction at one specific wavelength (410 nm) is $5.4 \cdot 10^{-9}$ cm^{-1} (average of 60 single shots). This quantity has to be multiplied by $\sqrt{2}$ for equal averaging of the sample and the blank measurement. Furthermore, it has to be considered that the measurement is performed over a whole spectral range (20-50 points) and not for one point only. The resulting standard deviation σ amounts to $1.7 \cdot 10^{-9}$ cm^{-1}, or 0.27 ppb for the peak at 408.5 nm. $3 \cdot \sigma$ is 0.8 ppb (detection limit), $6 \cdot \sigma$ corresponds to 1.6 ppb (determination limit).

@ 369 nm:

Much better extinction values (raw data) were obtained during the Feldex 2000 field campaign ($1.3 \cdot 10^{-5}$ cm^{-1}) compared to the values measured during the Berlin measurements in autumn 2001 ($2.4 \cdot 10^{-5}$ cm^{-1}). As the optical adjustment was more exact and stable in Berlin, this deviation can be explained by a possible reduction of mirror reflectivity due to contamination and aging processes. This can also explain the disappointingly low improvements of the detection limits in the 410 nm range in autumn/winter 2001/2002 compared to the earlier results in October 2000 in spite of the efforts concerning a perfect alignment.

The detection limit for HONO at 368 nm lies in the same range as for NO_2 at 410 nm. Worse mirror reflectivities at 368 nm causing a variation enhanced by a factor of 2 to 3 are levelled out by bigger differences in absorption cross sections for the HONO-peak at 368 nm (difference minimum to maximum is a bit less than twice the value for NO_2 at 410 nm, see **Fig. 1.4., Fig. 1.5.** in Chapter **1.4.**). This considerations result in $1 \cdot \sigma = 0.3$ ppb for Feldex 2000 and $1 \cdot \sigma = 0.5$ ppb for Berlin 2001/2002.

3.5.2.2. Standard Gas

The standard deviation of the extinction at one wavelength proves to be about factor 2 better than for external ambient air ($1 \cdot \sigma = 2.5\text{-}3 \cdot 10^{-9}$ cm^{-1}) which can be explained by the absence of aerosols and distinct temperature fluctuations. This value is in good coincidence with the theoretical sensitivity calculated for the parameters of the set-up in Chapter **1.5.** ($2.2 \cdot 10^{-9}$ cm^{-1}). The mirror reflectivity based upon the theoretical calculation in Chapter **1.5.** is 0.9995, a value which was obtained from experimental extinction measurements of the empty cavity. However, this value might be improved by profound mirror cleaning applying ultrasonic or by suppressing interfering higher transverse laser modes.

Summarising, the following options for improvements concerning detection limits and sensitivity present themselves:

- prolongation of the cavity to 1 – 3 m. This can be easily performed with the applied system consisting of "Leybold-bricks".
- Laser modes. Suppression of interfering laser modes for example by optimising the spatial filter, inserting pinholes, or introducing a chopper.
- Better mirror reflectivity. To be performed by a profound (ultrasonic) cleaning procedure or by replacing the mirrors.
- Higher repetition rate of the laser.

3.5.3. Errors

Calculating the standard deviation of different measurements of reference gas containing equal mixing ratios of NO_2, an error of 3-4% is observed. As already discussed in the previous section, this value has to be approximately doubled in the case of ambient external air.

The standard deviation of consecutive measurements at one wavelength ($\approx 2{\cdot}5\text{-}3{\cdot}10^{-9}$ cm^{-1} according to the previous section) amounts to ≈ 5% of the extinction of 10 ppb NO_2. This is the value for a point measurement, for a complete spectrum, however, the error of the evaluated concentration will be reduced (1-2%). On the other hand, some error sources are not considered in the standard deviation of the measured extinction: this is especially true for uncertainties in the tabulated absorption cross sections (1), excitation of interfering cavity modes which influence the slope of the transient signal (2), longer term thermal and mechanical variations (the value of the standard deviation mentioned above was determined for consecutive point measurements in the minute range) (3), variations in the wavelength tuning of the laser system (4), and the evaluation technique (5). Regarding the last aspect a good example is the comparison of results obtained for non-derivated and derivated spectra which frequently differ by several percent. An estimation of the overall error from these considerations gives a value approaching 10%.

Proceeding from the error mentioned at the beginning of this section and which was obtained from reference spectra (3-4% for standard gas, 7% for ambient air), the errors number (2) and (5) have to be integrated, and in the case of calibration renunciation as well error (1). Again, the resulting overall error is about 10% for ambient external air. Of course this value is enhanced for concentration approaching the detection limit and, also, for very high concentrations due to very short decay times of the ringdown signal.

Once again, as already stated several times in the course of this thesis, the application of the standard addition method could significantly reduce the error. However, this requires some modifications in the set-up including the acquisition of high-quality flowmeters and valves.

An example for the dimension of error bars resulting from the considerations in this section is shown in the last chapter **3.4., Fig. 3.18.**. For more clarity error bars were omitted in any other illustration of this thesis.

3.6. Aerosol Analysis

3.6.1. Influence of Aerosols

The effect of aerosols on the measurements is threefold: depending on its concentration, the aerosol laser light extinction contributes to the cavity losses which can overcome the amount of the absorption by trace gases. In case of low aerosol concentration, the effect on the total extinction can easily be erased during the concentration retrieval procedure, because the spectral signature of the aerosols shows a smoothed distribution (Bohren, 1983). Thus, after performing a derivation of the spectrum the aerosol influence can be deleted. The second effect is coupled to the aerosol concentration fluctuation during CRDS signal averaging, which increases the signal to noise ratio. The third effect of the aerosols on the CRDS signals is the contamination of the mirrors reflectivity, which happens when the rinsing flow of the mirrors is too low. This effect is shown in **Fig. 3.19.** curve (**b**), where the extinction continuously increases by an amount of 20 % during a 14 hours measurement. The small variations on the steady signal depict the real change of the atmospheric extinction which lay in the 10^{-7} cm^{-1} range. **Fig 3.19.** trace (**a**) shows the fluctuation of the atmosphere extinction, while a mechanical filter (paper) is mounted at the cell gas inlet. The relative variation is less pronounced and a decrease is observed, which indicates the absence of mirror contamination. The variation is rather related to the change of the atmosphere composition and to its temperature variation which is also affecting the CRDS observation.

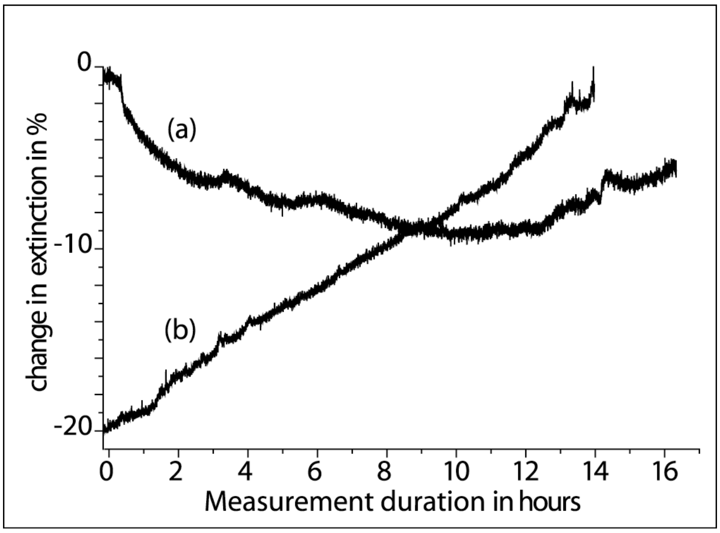

Fig. 3.19. Time distribution of the atmospheric optical extinction monitored at 410 nm by CRDS. (a) filter mounted in the gas inlet of the cell, October 11, 2001. (b) free air flow in the cavity, October 10, 2001.

By comparison with the values obtained by BLUME (Berliner Luftgütemeßnetz) for the same period the structure of curve (**a**) in **Fig.3.19.** can easily be correlated with the progress of the NO_2-concentration. This is done in **Fig.3.20.**. The same can be stated for curve (**b**) after subtraction of the linear increase caused by mirror contamination. **Fig.3.20.** also shows that the progress of the NO_2-concentrations could be followed with extremely high time resolution. A problem, however, is the calculation of the absolute value of the NO_2-concentration when the measurement is performed on one wavelength only. As already stated in the discussion of the evaluation procedure (Chapter **1.9.**), it is not sufficient just to subtract the blank value measured at the same wavelength, i.e. 410 nm, in order to calculate the concentration directly from the net extinction via comparison with the absorption cross sections found in literature. Otherwise, we would possess a method for easy determination of absolute analyte concentrations in extremely high time resolution.

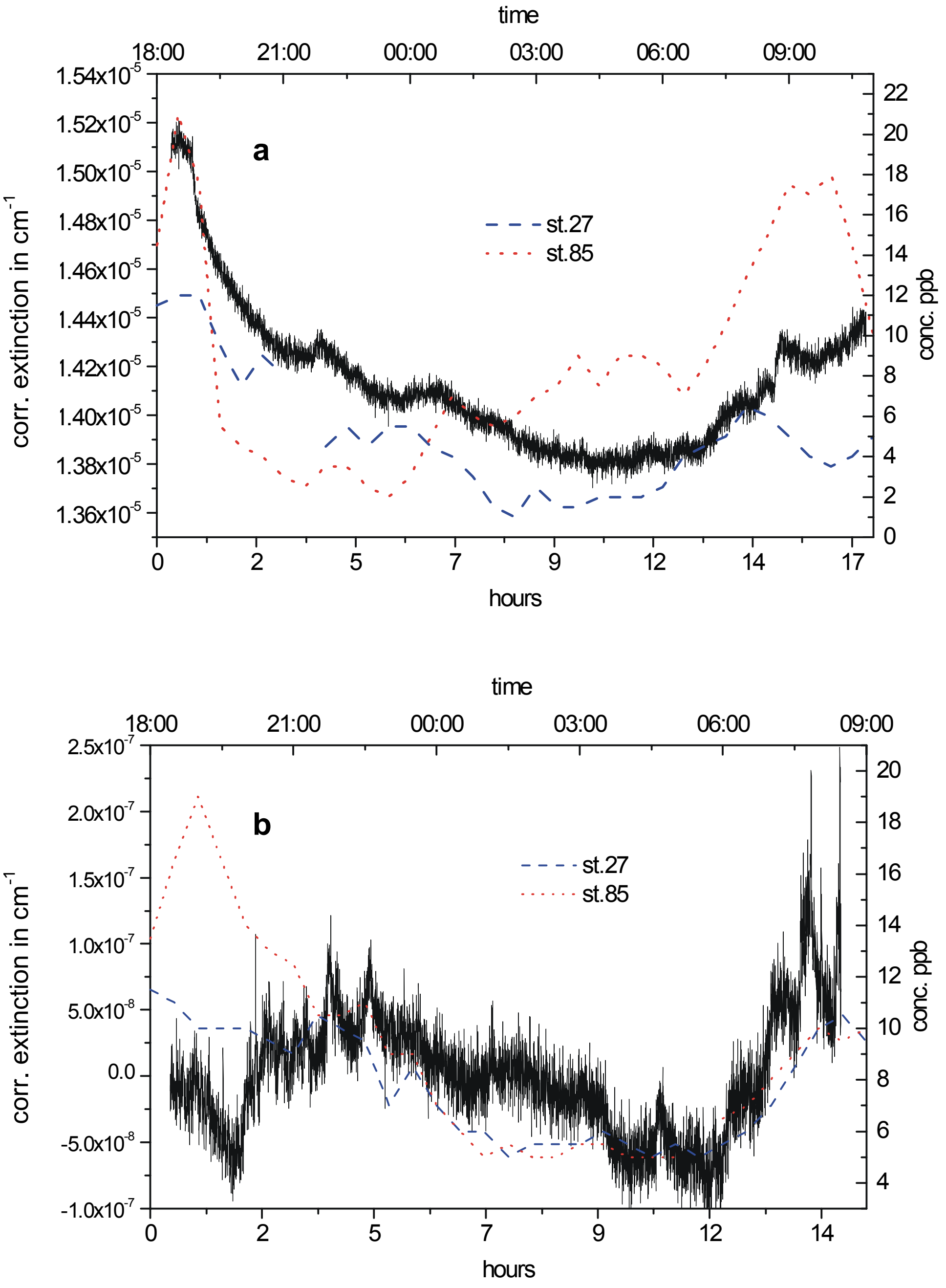

Fig. 3.20. Comparison of the longterm measurements in Fig.3.19. with BLUME-values for NO_2. The diagrams **a** and **b** correspond to the curves (a) and (b) in the last Fig. 3.19.. For the lower diagram **b** the linear increase shown in Fig. 3.19. was subtracted.

An estimation of the influence of the temperature variation is done in **Fig. 3.21.**. The cavity was streamed by N_2 (grey) or filled by ambient air (black) from the laboratory, the smooth progress of the curves can be explained by temperature effects especially in the case of the steep descend in the beginning as the measurement was performed overnight. Four hours after the leave of the laboratory the values stabilised followed by a slight increase which could have been caused by a slight de-adjustment of the system. However, it must be emphasised that the changes in extinction in **Fig. 3.21.** are much smaller compared to the variations in **Fig. 3.19.** amounting to 10-20% of those values only.

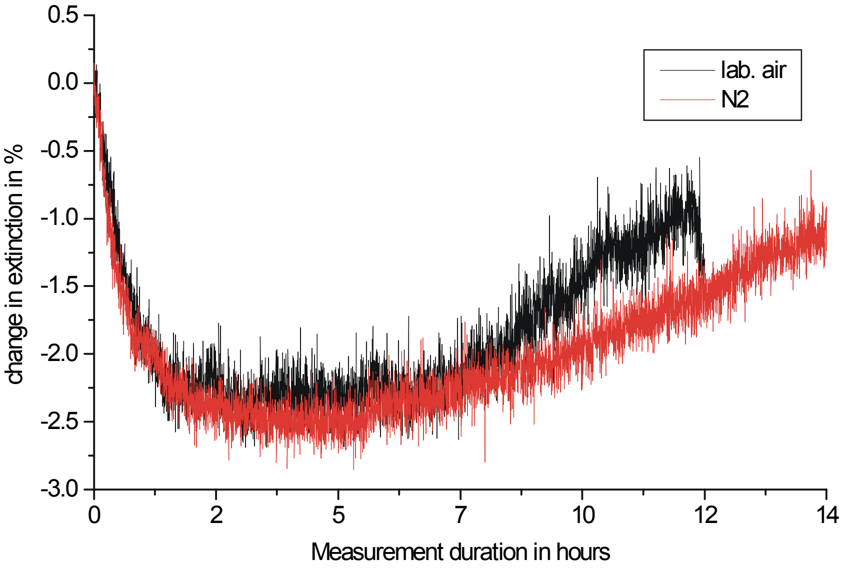

Fig. 3.21. Change in extinction for a cavity streamed by N_2 and laboratory air. The progress of the curves can be explained by temperature effects.

3.6.2. Determination of Aerosols

Although the quantification of aerosols was not the main aim of this work, the CRDS method gives an easy access to the determination of aerosol extinction. One approach could be a comparison of a background corrected spectrum with its derivative which omits aerosol effects due to their smooth contribution to the spectrum. However, as stated above uncertainties arise from inevitable changes of the background level (thermal and mechanical effects, mirror contamination) which would directly affect the measured aerosol value. These changes and drifts, which can not be directly attributed to aerosol influence, become obvious in **Fig. 3.22.a** by the slight increase of both curves (with and without filter) in time.

Another possibility is the application of a mechanical filter for aerosols. A comparison of directly consecutive spectra obtained with and without filter containing the same values for the background contribution is shown in **Fig. 3.22.**:the diagrams show two different examples for aerosol contribution to the extinction. To show the difference in aerosol extinction more clearly, the scale of the y-axis was kept constant for the upper diagram **a** and the lower diagram **b**.

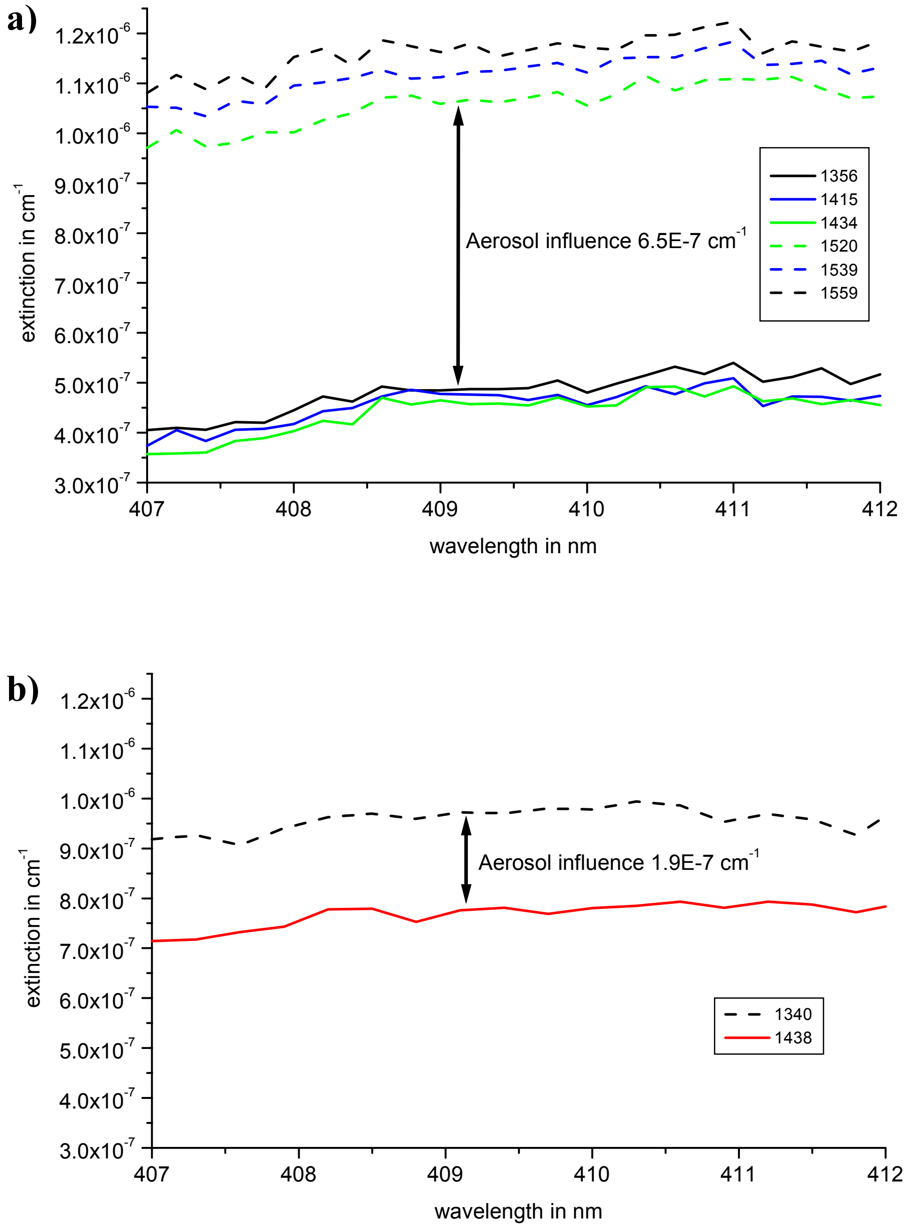

Fig. 3.22. Measurement including background correction. **a)** from 10.12.01 with (1356-1434, solid lines) and without (1520-1559, dashed lines) filter. **b)** from 12.12.01 with (solid line) and without (dashed line) filter. Aerosol influence: 6.5E-7 cm^{-1} and 1.9E-7 cm^{-1}, respectively.

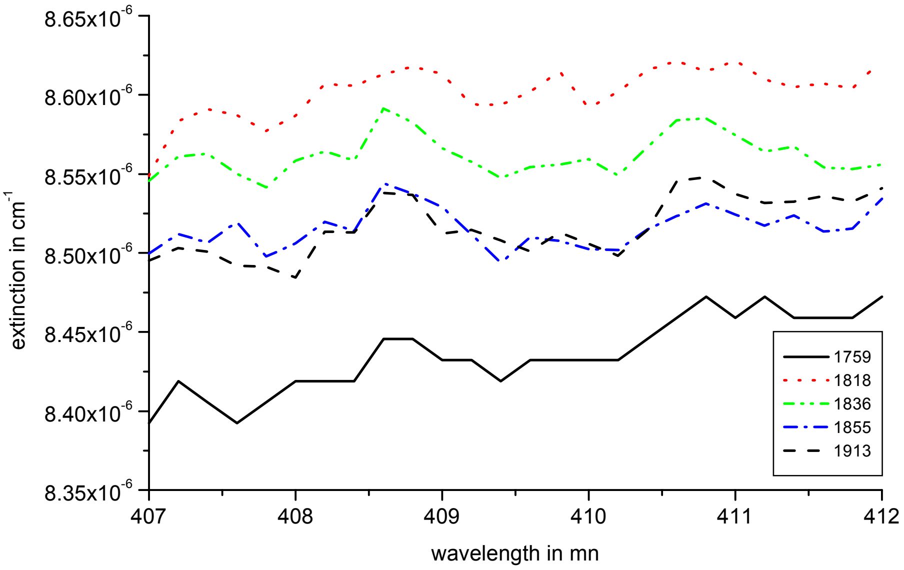

Fig. 3.23. Measurement from 22.12.01 with (1759, solid line) and without filter (others, dashed lines). No background correction was accomplished. Aerosol influence: 1.66E-7 cm^{-1}.

Raw data are depicted in **Fig. 3.23.**, i.e. no background correction was applied for these spectra. The drift of the raw spectra in time is obvious, however, a stabilisation occurs after about one hour (the numbers connected to the spectra in the legend refer to real times) which might be caused by temperature effects. A temperature shock might occur when cold, aerosol load air enters the cavity. Furthermore, it can be learned from this picture that quantitative and rapid aerosol analysis is possible without background correction.

Finally, an impressive example for the influence of aerosols on the measured extinction is shown in **Fig. 3.24.**: the extremely sharp and high peak which occurred after about 6 hours measuring time was produced by aerosols of cigarette smoke exhaled at the end of the inlet port for ambient air. The diagram refers to a long-term measurement over a total duration of 7 hours.

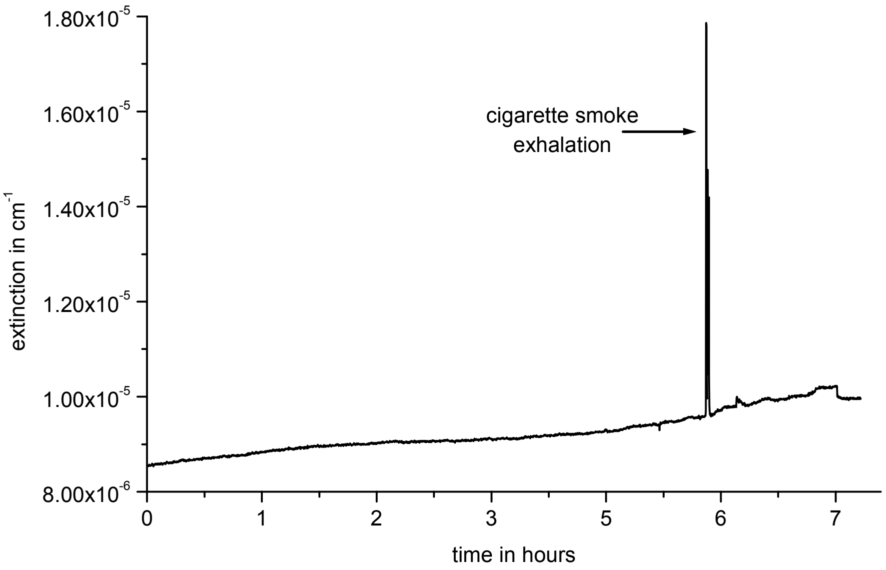

Fig. 3.24. Influence of aerosols produced by cigarette smoke. The spike in the extinction after 6 hours is caused by exhalation of smoke near the end of the inlet tube.

Resuming the aspects of this chapter, it is obvious that direct determination of the aerosol contribution to the total extinction, i.e. the aerosol extinction, is easily possible by CRDS. In the future experiments should be performed which introduce different mechanical filters with different mesh sizes and impactors, respectively. In this way, the size distribution of aerosols can be determined quantitatively.

3.7. Conclusions and Outlook

This study has demonstrated the first application of Cavity Ringdown Spectroscopy for the continuous monitoring of NO_2 and HONO under real and extreme field measurement conditions. The FELDEX 2000 campaign on Kleiner Feldberg near Frankfurt, for which the set-up was installed in a mobile platform, could prove that this sensitive spectroscopy method is suitable for field measurements. Continuous measurements have been performed in Berlin-Adlershof in autumn and winter 2001. Comparison between the CRDS results and the measurements performed by the Berliner Luftgüte Meßnetz. (BLUME) showed an excellent correlation. Applying broad laser emission (5 cm^{-1}) for CRDS was not conventional and has conducted to excellent results concerning the measurement duty cycle, which reaches 90% describing a stand-alone operation.

The application of the standard addition method, as described in chapter 1.9.4.4., could improve the quality of the CRDS measurements, reducing sources of errors, like matrix effects caused by bath gas molecules [chapters 1.3., 1.9., 3.1.]. However, this approach requires a new gas mixing system, especially including the integration of a high-quality flow-meter for external ambient air. As the standard addition technique might be too time-consuming for routine analysis, the derivation of adequate correction factors should be attained. This can be done by comparing the results obtained by the standard addition method with results acquired in N_2/ clean air or by self-calibrating analysis (which omits reference gas measurements).

The achieved detection limits lie in the 0.5 ppb-range. A further improvement of the detection limit down to values below 100 ppt should be reached to match the air monitoring and survey conditions. This will lead to minor improvements of the laser emission properties and to improvements of the measurement cell by increasing the quality of the laminar flow. Special attention should be directed on the mirror reflectivity as this value is a major parameter concerning attainable sensitivity. The introduction and test of profound cleaning procedures including ultrasound should have priority.

The experiments have shown sensitivity towards thermo-mechanical fluctuations. Hence, the integration of the set-up in a air-conditioned climate chamber will be an improvement.

The integration of a chopper in front of the cavity can be a very helpful mean in order to suppress interfering cavity modes. A coincidence of the slope of two different chopped “bites” of the decay curve indicate a perfect adjustment and alignment of the set-up eliminating any disturbing transverse cavity mode.

The method described in this thesis showed its ability to simultaneously analyse different atmospheric trace compound (NO_2 and HONO). This capability of multi-compound analysis can be extended to a series of further species by the application of a suitable pair of dielectric mirrors. Of outstanding interest are simultaneous measurements of HONO/ HCHO/ NO_2 or the aromatics like benzene, toluene, and phenol.

Moreover, this study has shown that CRDS technique performs reliable measurement of the aerosol loading of the atmosphere. By the use of filters or impactors of different mesh size the size distribution of the particulate matter can be determined. On the other hand, however, the filter can change the chemical properties of the air to be probed.

The detection of radicals and HONO is difficult with instruments using a monitoring cell and long tubes. The possibility of applying an open air optical cavity will decisively improve this measurement technique and will make it even more attractive for atmospheric studies and survey. Further minimising by replacing the bulky laser system on cost of a reduction of the wavelength range will be necessary for some analytical tasks.

Furthermore, promising CRDS should be possible in liquid phase (Xu et al., 2002) by minor changes in the system. Liquid even could be filled into the vacuum tight stainless steel measuring cell.

To sum up, it can be stated that CRDS proved to be a very promising UV-VIS spectroscopy method for simultaneous multi-compounds analysis and survey of atmospheric traces in ambient air. Improvements still have to be made, however, in the near future; it should be established as a new standard technique for routine analysis even on mobile platforms.

4. Summary

Cavity ringdown spectroscopy (CRDS) is a promising relatively new approach for making ultrasensitive direct absorption measurements with pulsed (and cw) lasers. In this thesis it was introduced for in situ atmospheric traces measurements for both laboratory and field applications. A new developed broadly tunable OPO laser source was applied allowing measurements from the UV to the near infrared. The technique proved to be reliable, robust, and compact and was well suited for simultaneous multicomponent analysis of atmospheric traces in the ppb and sub-ppb concentration range.

In CRDS a short laser pulse is injected into an optical cavity composed of two highly reflective mirrors separated by a distance of less than one meter. While the pulse is reflected back and forth within the cavity, the small amount of energy leaking out of the cavity is used to monitor the decaying time evolution of the light intensity. The decay time depends on the reflectivity of the mirrors, but it is also sensitive to the presence of absorbing molecules within the cavity. As the effective absorption path length approaches several kilometres, very high sensitivities are achieved. Simulation programs assisted a proper cavity design with regard to stability and coupling efficiency.

Spectra obtained by tuning the OPO laser wavelength were evaluated by applying different orders of derivations after smoothing the particular spectrum by convolution with a simulated laser pulse. Best results could be obtained for the first derivative, however, for flat analyte peaks a non-derivative evaluation can be advantageous. In both cases the background has to be subtracted in order to eliminate varying mirror reflectivities as well as effects caused by aerosols, Rayleigh, and Mie scattering. Problems caused by background variations could not be eliminated by applying higher derivative orders (2nd and 4th) due to high sensitivity to minor wavelength fluctuations. Following the differentiation step, the analyte concentrations were calculated by multicomponent analysis and least square fit to a reference spectrum formed by tabulated absorption cross sections. A comparison with experimental reference spectra obtained in N_2-atmosphere revealed severe problems due to matrix effects.

In the course of the optimisation of the measurement parameters a shot selection proved to be suitable to reduce the variation of the signal and the noise of the measured extinction value. This was done by eliminating the ringdown signals with the highest and lowest amplitudes whereby the averaging of 60 out of 90 laser shots revealed best results.

Concerning the selection of appropriate test analytes nitrogen dioxide (NO_2) was chosen due to its favourable spectral range and structure in respect to the CRDS set-up. Furthermore, NO_2 is well monitored by standard devices based on photoluminiscence, which gives easy access to comparison values. Nitrous acid (HONO) represents a trace compound of significant scientific interest, however, its detection is a difficult analytical task. As its absorption spectrum interferes with the NO_2-spectrum, a simultaneous detection is aspired.

Laboratory measurements of highly concentrated reference gas (10 ppm) showed good agreement with the specified values, however, a calibration curve revealed remarkable deviations between measured and calculated value for increasing dilution factors. In pure N_2-atmosphere the retrieval rates were reduced to 40-50% in the concentration range 1 – 100 ppb, while this reduction amounts to 80% in clean air. This can be explained by the delicate photochemistry of NO_2 in the 400 nm range and by matrix effects of the bath gas. These matrix effects, mainly comprising varying quenching rates of the different bath gas molecules, can be eliminated in future set-ups by mixing devices using real outside air. The dynamic range in respect to NO_2 could be determined to 0.5 ppb (detection limit in clean air) up to approximately 20 ppm (strongly reduced ringdown times).

Long-term measurements of outside ambient air in Berlin-Adlershof in autumn and winter 2001 showed very good coincidence with the results of the Berliner Luftgüte Meßnetz (BLUME) concerning the progress of NO_2-concentrations. Its characteristics and deviations could be explained in almost any case by the situation, location, and exposure of the sites as well as by meteorological conditions mainly described by the wind direction. A detection limit of 0.8 ppb was obtained. The absolute concentration values lie about 12% below BLUME regarding the overall average. This can be explained by photochemical and photophysical processes as well as a general underestimation caused by the evaluation procedure. Hence, the introduction of a general correction factor determined from a large amount of data can be a proper means. The experiment was running for several months and proved to be stable and reliable during this period. A daily quick-check normally can be restricted to a rapid cavity realignment at two screws, the dielectric mirrors should be cleaned after 4 –7 days.

The analysis of nitrous acid proved to be very delicate mainly due to insufficient mirror reflectivities in the wavelength range around 368 nm. However, at least some indications and results could be obtained and a suitable evaluation method could be elaborated. For further investigations a different pair of mirrors (HR @ 354 nm or 368 nm), a HONO-generator, and an open cavity will be helpful. The detection limits of HONO are comparable to the values of NO_2 (0.8 ppb).

The CRDS set-up offers interesting possibilities in aerosol analysis: in a simple experiment the aerosol contribution to the extinction could be determined by comparing values obtained with and without a mechanical filter suppressing aerosols. A different approach is the comparison of non-derivated spectra with spectra preferably evaluated by 2^{nd} derivation.

During the Feldex 2000 campaign on Kleiner Feldberg near Frankfurt the CRDS device could prove its field suitability even under extreme and unfavourable circumstances concerning wind and wetness. For this purpose the set-up was installed in a caravan, however, an installation in a more restricted vicinity is conceivable without problems.

As resume it can be stated that first field measurements of NO_2 and HONO in outside ambient air using cavity ringdown spectroscopy were made. A new pulsed OPO-laser-system was applied which enables measurements from the UV (240 nm) to the near infrared opening a new spectral range for CRDS-analysis. The device has shown its ability to simultaneously analyse different atmospheric trace compounds.

5. References

Acker, K.; Möller, D.; Wieprecht, W.; Auel, R.; Kalass, D.; Tscherwenka, W.: Nitrous and Nitric Acid Measurements Inside and Outside of Clouds at Mt. Brocken, *Water, Air, and Soil Pollution 130, 331-336 (2001).*

Andres-Hernandez, M.D.; Notholt, J.; Hjorth, J.; Schrems, O.: A DOAS study on the origin of nitrous acid at urban and non-urban sites, *Atmos. Environ. Vol. 30, 175-180 (1996).*

Anstett, G.; Göritz, G.; Kabs, D.; Urschel, R.; Wallenstein, R.; Borsutzky, A.: Reduction of the spectral width and beam divergence of a BBO-OPO by using collinear type-II phase matching and back reflection of the pump beam, *Appl. Phys. B 72, 583-589 (2001).*

Appel, B.R.; Winer, A.M.; Tokiwa, Y.; Biermann, H.W.: Comparison of atmospheric nitrous acid measurements by annular denuder and differential optical absorption systems, *Atmos. Environ., Vol. 24A, 611-616 (1990).*

Ball, S.M.; Povey, I.M.; Norton, E.G.; Jones, R.L.: Broadband cavity ringdown spectroscopy of the NO_3 radical, *Chem. Phys. Letters 342, 113-120 (2001)*.

Baxter, G.W.; Payne, M.A.; Austin, B.D.W.; Halloway, C.A.; Haub, J.G.; He, Y.; Milce, A.P.; Nibler, J.F.; Orr, B.J.: Spectroscopic diagnostics of chemical processes: applications of tunable optical parametric oscillators, *Appl. Phys. B, Vol. 71, 651-663 (2000).*

Berden, G.; Peeters, R.; Meijer, G.: Cavity ring-down spectroscopy: Experimental schemes and applications, *Int. Reviews Phys. Chem. Vol. 19, No. 4, 565-607 (2000).*

Berliner Luftgüte Meßnetz (BLUME), http://www.stadtentwicklung.berlin.de/umwelt/blume/

Bohren, F.; Huffman, D.R.: Absorption and scattering of light by small Particules, *John Wiley, New-York (1983).*

Bosenberg, W.R.; Cheng, L.K.; Tang, C.L.: Ultraviolet optical parametric oscillation in β-BaB_2O_4, *Appl. Phys. Lett., Vol. 54 (1), 13-15 (1989).*

Bosenberg, W.R.; Pelouch, W.S.; Tang, C.L.: High-efficiency and narrow-linewidth operation of a two-crystal β-BaB_2O_4, optical parametric oscillator, *Appl. Phys. Lett., Vol. 55 (19), 1952-1954 (1989).*

Bosenberg, W.R.; Tang, C.L.: Type II phase matching in a β-barium borate optical parametric oscillator, *Appl. Phys. Lett., Vol. 56 (19), 1819-1821 (1990).*

Borsutzky, A.: Frequency control of pulsed optical parametric oscillators, Quantum Semiclass. Opt., Vol. 9, 191-207 (1997).

Bradshaw, J.; Davis, D.; Crawford, J.; Chen, G.; Shetter, R.; Muller, M.; Gregory, G.; Sachse, G.; Blake, D.; Heikes, B.; Singh, H.; Mastromarino, J.; Sandholm, S.: Photofragmentation Two-Photon Laser-Induced Fluorescence Detection of NO_2 and NO: Comparison of Measurements with Model Results Based on Airborne Observations During PEM-Tropics A, *Geophy. Res. Lett., Vol. 26, 4471-4474 (1999).*

Brown, S.S.; Stark, H.; Ciciora, S.J.; Ravishankara, A.R.: In-situ measurement of atmospheric NO_3 and N_2O_5 via cavity ring-down spectroscopy, *Geophys. Res. Lett., Vol. 28, No.17, 3227-3230 (2001).*

Busch, K.W.(ed.); Busch, M.A.(ed.): Cavity-Ringdown Spectroscopy: An Ultratrace-Absorption Measurement Technique, *ACS Symposium Series 720, American Chemical Society, Washington (1999).*

Busch, K.W.; Hennequin, A.; Busch, M.A.: Introduction to Optical Cavities: *in Cavity-Ringdown Spectroscopy Chap. 3, ed. By K.W. Busch, M.A. Busch, ACS, Washington (1999).*

Cheng, L.K.; Bosenberg, W.R.; Tang, C.L.: Broadly tunable optical parametric oscillation in β-BaB_2O_4, *Appl. Phys. Lett., Vol. 53 (3), 175-177 (1988).*

Clough, P.N.; Thrush B.A.: Mechanism of chemiluminescent reaction between nitric oxide and ozone, *Trans. Faraday Soc., 63, 915-925, (1967).*

Crawford, J.H.; Davis, D.D.; Chen, G.;Bradshaw, J.;Sandholm, S.;Kondo, Y.;Merrill, J.;Liu, S.;Browell, E.;Gregory, G.;Anderson, B.;Sachse, G.;Barrick, J.;Blake, D.;Talbot, R.; Pueschel, R.: Implications of large scale shifts in tropospheric NO_x levels in the remote tropical Pacific, *J. Geophys. Res. Vol. 102, 28447-28468 (1997).*

Crowley, J.N.; Carl, S.A.: OH Formation in the Photoexcitation of NO_2 beyond the Dissociation Threshold in the Presence of Water Vapour, *J. Phys. Chem. A, 101, 4178-4184 (1997).*

Crutzen P.J., Graedel, T.E.: Chemie der Atmosphäre, *Spektrum Akad. Vlg., Heidelberg, (1995)*

Czyzewski, A.; Chudzynski, S.; Ernst, K.; Karasinski, G.; Kilianek, L.; Pietruczuk, A.; Skubiszak, W.; Stacewicz, T.; Stelmaszczyk, K.; Koch, B.; Rairoux, P.: Cavity ring-down spectrography, *Optics Communications 191, 271-275 (2001).*

Davis, C.D.: Lasers and Electro-Optics: Fundamentals and Engineering, *Cambridge University Press, Cambridge (1996).*

Demtröder, W.: Laserspektroskopie: Grundlagen und Techniken 4. Aufl., *Springer-Verlag Berlin Heidelberg New York (2000).*

Dias-Lalcaca, P.; Brunner, D.; Imfeld, W.; Moser, W.; Staehlin, J.: An Automated System for the Measurement of Nitrogen Oxides and Ozone Concentrations from a Passenger Aircraft: Instrumentation and First Results of the NOXAR Project, *Environ. Sci. Technol., Vol. 32, 3228-3236 (1998).*

Eichler, J.; Eichler, H.J.: Laser: Bauformen, Strahlführung, Anwendungen, 4.Auflage, *Springer-Verlag Berlin Heidelberg New York (2001).*

Engeln, R.; Berden, G.; Peeters, R.; Meijer, G.: Cavity enhanced absorption and cavity enhanced magnetic rotation spectroscopy, *Rev. Sci. Instrum. Vol. 69, No. 11 (1998).*

Etzkorn, T.; Klotz, B.; Sørensen, S.; Patroescu, I.V.; Barnes, I.; Becker, K.H.; Platt, U.: Gas-Phase Absorption Cross Sections of 24 Monocyclic Aromatic Hydrocarbons in the UV and IR Spectral Ranges, *Atmos. Environ., 33, 525-540 (1999).*

Evertsen, R.; Staicu, A.; Dam, N.; Van Vliet, A.; Ter Meulen, J.J.: Pulsed cavity ring-down spectroscopy of NO and NO_2 in the exhaust of a diesel engine, *Appl. Phys. B 74, 465-468 (2002).*

Febo, A.; Perrino, C.; Cortiello, M.: A Denuder Technique for the Measurement of Nitrous Acid in Urban Atmospheres, *Atmos. Environ., Vol. 27A, 1721-1728 (1993).*

Febo, A.; Perrino, C.; Gherardi, M.; Sparapani, R.: Evaluation of a High-Purity and High-Stability Continuous Generation System for Nitrous Acid, *Environ. Sci. Technol., Vol. 29, 2390-2395 (1995).*

Febo, A.; Perrino, C.; Allegrini, I.: Measurements of Nitrous Acid in Milan, Italy, by DOAS and Diffusion Denuders, *Atmos. Environ., Vol. 30, 3599-3609 (1996).*

Finlayson-Pitts, B.J.; Pitts Jr, J.N.: Chemistry of the Upper and Lower Atmosphere, *Academic Press, San Diego (2000).*

Fong, C.; Brune, W.H.: A laser induced fluorescence instrument for measuring tropospheric NO_2, *Rev. Sci. Instrum, Vol. 68, 4253-4262 (1997).*

Gaffney, J.S.; Bornick, R.M.; Chen, Y.-H.; Marley, N.A.: Capillary Gas Chromatographic Analysis of Nitrogen Dioxide and PANs with Luminol Chemiluminescent Detection, *Atmos. Environ., Vol. 32, 1145-1154 (1998).*

Garnica, R.M.; Appel, M.F.; Eagan, L.; McKeachie, JR.; Benter, T.: A REMPI Method for the Ultrasensitive Detection of NO and NO_2 Using Atmospheric Pressure Laser Ionization Mass Spectrometry, *Anal. Chem., Vol. 72, 5639-5646 (2000).*

George, L.A.; O'Brien, R.J.: Prototype FAGE Determination of NO_2, *J.Atmos. Chem., Vol.12, 195-209 (1991).*

Geyer, A.: The Role of the Nitrate Radical in the Boundary Layer – Observations and Modeling Studies, *Dissertation Universität Heidelberg, Heidelberg (2000).*

Göritz, G.: personal communication (2000).

Graedel, T.E., Crutzen, P.J.: Veränderungen der Atmosphäre, *in: Atmosphäre, Klima, Umwelt, Spektrum-der-Wissenschaft-Verlagsgesellschaft, Heidelberg, (1990).*

Harder, J.W.; Williams, E.J.; Baumann, K.; Fehsenfeld, F.C.: Ground-based comparison of NO_2, H_2O, and O_3 measured by long-path and in situ techniques during the 1993 Tropospheric OH Photochemistry Experiment, *J. Geophys. Res., Vol. 102, 6227-6243 (1997).*

Harris, G.W.; Carter, W.P.L.; Winer, A.M.; Pitts Jr, J.N.; Platt, U.; Perner, D.: Observations of nitrous acid in the Los Angeles atmosphere and the implications for the ozone precursor relationships, *Environ. Sci. Technol., Vol. 16, 414-419 (1982).*

Haub, J.G.; Johnson, M.J.; Orr, B.J.; Wallenstein, R.: Continuously tunable injection-seeded b-barium borate optical parametric oscillator: Spectroscopic applications, *Appl. Phys. Lett., Vol. 58 (16), 1718-1720 (1991).*

He, Y.; Hippler, M.; Quack, M.: High-resolution cavity ring-down absorption spectroscopy of nitrous oxide and chloroform using a near-infrared cw diode laser, *Chem. Phys. Letters, Vol. 289, 527-534(1998).*

Hecht, E.: Optik, 2. Auflage, *R. Oldenbourg Verlag München Wien (1999).*

HITRAN96, database, http://www.hitran.com

Hodges, J.T.; Looney, J.P.; van Zee, R.D.: Response of a ring-down cavity to an arbitrary excitation, *J. Chem. Phys. Vol. 105, No. 23, 10278-10288 (1996).*

Huang, G.; Zhou, X.; Deng, G.; Qiao, H.; Civerolo, K.: Measurements of atmospheric nitrous acid and nitric acid, *Atmos. Environ., Vol. 36, 2225-2235 (2002).*

Jamal, R.; Kraus, P.: LabVIEW: Das Grundlagenbuch, 2.Aufl, *Prentice Hall, München (1998).*

Jamal, R.; Pichlik, H.: LabVIEW: Das Anwenderbuch, 2.Aufl, *Prentice Hall, München (1999).*

King, M.D.; Dick, E.M.; Simpson, W.R.: A new method for the atmospheric detection of the nitrate radical (NO_3), *Atmos. Env. 34, 683-686 (2000).*

Kitto, A.-M.N.; Harrison, R.M.: Nitrous and nitric acid measurements at sites in south-east England, *Atmos. Environ. Vol. 26A, 235-241 (1992).*

Kleffmann, J.; Becker, K.H.; Wiesen, P.: Heterogeneous NO_2 Conversion Processes on Acid Surfaces: Possible Atmospheric Implications, *Atmos. Environ., Vol. 32, 2721-2729 (1998).*

Koechner, W.: Solid-State Laser Engineering, 5th ed., *Springer Series in Optical Sciences Vol.1, Springer Verlag, Berlin Heidelberg New York (1999).*

Lammel, G.; Cape, J.N.: Nitrous Acid and Nitrite in the Atmosphere: *Chem. Soc. Rev, 361-369 (1996).*

Lauterbach, J.; Kleine, D.; Kleinermanns, K.; Hering, P.: Cavity-ring-down spectroscopic studies of NO_2 in the region around 613 nm, *Appl. Phys. B 71, 873-876 (2000).*

Lee, D.-H.; Yoon, Y.; Kim, B.; Lee, J.Y.; Yoo, Y.S.; Hahn, J.W.: Optimization of the mode matching in pulsed cavity ringdown spectroscopy by monitoring non-degenerate transverse mode beating, *Appl. Phys. B 74, 435-440 (2002).*

Marley, N.A.; Gaffney, J.S.; Gunter, R.L.; Luke, W.T.: New Improved GC-Luminol Instrument for PAN and Nitrogen Dioxide Measurements, *AMS 5th conference on Atmospheric Chemistry: Gases, Aerosols, and Clouds 2003 (2002).*

Matsumi, Y.; Murakami, S; Kono, M.; Takahashi, K.; Koike, M.; Kondo, Y.: High-Sensitivity Instrument for Measurement Atmospheric NO_2, *Anal. Chem, 73, 5485-5493 (2001).*

Merienne M.F.; Jenouvrier A.; Coquart B.: The NO_2 Absorption Spectrum. I: Absorption Cross-Sections in the 300-500 nm Region, *J. Atmos. Chem., Vol. 20, No. 3, 281-297 (1995).*

Meyer, P.L.; Sigrist, M.W.: Atmospheric Pollution Monitoring Using CO2-Laser Photoacoustic Spectroscopy and Other Techniques, (Invited Review), *Rev. Sci. Instrum. Vol. 61, 1779-1807 (1990).*

Möller, D.; Mauersberger, G.: Cloud Chemistry effects on Tropospheric Photooxidants in polluted atmosphere – Model Results, *J. Atmos. Chem. 14, 153-165 (1992).*

Möller, D.: Global Sulfur and Nitrogen Biogeochemical Cycles, *ERCA Vol.2: Physics and Chemistry of the Atmospheres of the Earth and Other Objects of the Solar System, Les Editions de Physique, Les Ulis (1994).*

Motto-Ros, V.: Mise en place de la Continuous-Wave Cavity Ring Down Spectroscopy, *Diplôme d’Etudes Approfondies, Université Claude Bernard Lyon-1 (2002).*

Meschede, D.: Optik, Licht und Laser, *B.G. Teubner Stuttgart Leipzig (1999).*

Morville, J.: Injection des cavités optiques de haute finesse par laser à diode – Application à la CW-CRDS et à la détection de traces atmosphériques. *Thèse, UFR de Physique, Grenoble, (2001).*

National Res. Council: Rethinking the Ozone Problem in Urban and Regional Air Pollution, *National Academy Press, (1991).*

Nizkorodov, S.A.; Makarov, V.I.; Khmelinski, I.V.; Kotschubei, S.A.; Asomov, K.A.: LIF detection of NO_3 radical after pulsed excitation of NO_2 vapor at 436.45 nm, *Chem. Phys. Lett., Vol. 222, 135-140 (1994).*

Nölle, A.; Pätzold, F.; Pätzold, S.; Meller, R.; Moortgat, G.K.; Röth, E.P.; Ruhnke, R.; Keller-Rudek, H.: UV/Vis Spectra of Atmospheric Constituents, Version1, *DLR-DFD Oberpfaffenhofen (1998).*

Okabe, H.: Photochemistry of Small Molecules, *John Wiley and Sons, New York (1978).*

O’Keefe, A.; Deacon, D.A.G.: Cavity ring-down optical spectrometer for absorption measurements using pulsed laser sources, *Rev. Sci. Instrum. 59 (12), 2544-2551 (1988).*

O’Keefe, A.; Scherer, J.J.; Paul, J.B.; Saykally, R.J.: Cavity-Ringdown Laser Spectroscopy: History, Development, and Applications: *in Cavity-Ringdown Spectroscopy Chap. 6, ed. By K.W. Busch, M.A. Busch, ACS, Washington (1999).*

Patten Jr., K.O.; Burley, J.D.; Johnston, H.S.: Radiative Lifetimes of Nitrogen Dioxide for Excitation Wavelengths from 400 to 750 nm, *J. Phys. Chem., Vol. 94, 7960-7969 (1990).*

Paul, J.B.; Saykally, R.J.: Cavity Ringdown Laser Absorption Spectroscopy, *Anal. Chem. News & Features 287A-292A (1997).*

Perner, D.; Platt, U.: Detection of Nitrous Acid in the Atmosphere by Differential Optical Absorption, *Geophys. Res. Lett., No. 6, 917-920, (1979).*

Pfeilsticker K.; Arlander, D.W.; Burrows, J.P.; Erle, F.; Gil, M.; Goutail, F.; Hermans, C.; Lambert, J-C.; Platt, U.; Pommereau, J.-P.; Richter, A.; Sarkissian, A.; van Roozendael, M. Wagner, T.; and Winterrath, T.: Intercomparison of the measured influence of tropospheric clouds on UV-visible absorptions detected during the NDSC intercomparison campaign at OHP in June 1996*, Geophys. Res. Lett., No. 26, 1169-1173, (1999).*

Plane, J.M.C.: Spectroscopic Techniques for Atmospheric Measurements, *ERCA: Topics in Atmospheric and Interstellar Physics and Chemistry, Les Editions de Physique, Les Ulis (1994).*

Platt, U.; Perner, D.; Harris, G.W.; Winer, A.M.; Pitts Jr, J.N.: Observations of nitrous acid in an urban atmosphere by differential optical absorption, *Nature Vol. 285 (1980).*

Platt, U.: The origin of nitrous and nitric acid in the atmosphere, in W. Jaeschke (ed.), *Chemistry of Multi Phase Atmosphere Systems, Springer, Berlin, NATO-ASI series (1985).*

Rairoux, P.; Koch, B.; Möller, D.; Göritz, G.; Warmbier, G.: Atmospheric Traces Monitoring Applying Cavity Ring-Down Spectroscopy, *Environ. Sci. Poll. Res., Special issue 4, 68-71 (2002).*

Roehl, C.M.; Orlando, J.J.; Tyndall, G.S.; Shetter, R.E.; Vazquez, G.J.; Cantrell, C.A.; Calvert, J.G.: Temperature Dependence of the Quantum Yields for the Photolysis of NO_2 near the Dissociation Limit, *J. Phys. Chem., 98, 7837-7843 (1994).*

Romanini, D.; Kachanov, A.A.; Sadeghi, N.; Stoeckel, F.: CW cavity ring down spectroscopy, *Chem. Phys. Lett., Vol. 264, 316-322 (1997).*

Romanini, D.; Kachanov, A.A.; Stoeckel, F.: Diode laser cavity ring down spectroscopy, *Chem. Phys. Lett., Vol. 270, 538-545 (1997).*

Scherer, J.J.; Paul, J.B.; O`Keefe, A.; Saykally, R.J.: Cavity Ringdown Laser Absorption Spectroscopy: History, Development, and Application to Pulsed Molecular Beams, *Chem. Rev. 97, 25-51 (1997).*

Schiff H.I.; Karecki D.R.; Harris G.W.; Hastie D.R.; MacKay G.I.: A Tunable Diode Laser System for Aircraft Measurements of Trace Gases*, J. Geophys. Res., Vol. 95, 10147-10153, (1990).*

Schiff, H.I.: Ground Based Measurements of Atmospheric Gases by Spectroscopic Methods, *Ber. Bunsenges. Phys. Chem., Vol. 96, No. 3, 296-306 (1992).*

Schiller, C.L.; Locquiao, S.; Johnson, T.J.; Harris, G.W.: Atmospheric Measurements of HONO by Tunable Diode Laser Absorption Spectroscopy, *J. Atmos. Chem. 40, 275-293 (2001).*

Schiller, S.; Meyn, J.-P.: Von der Photonenspaltung zum kontinuierlich emittierenden Universallaser, *Physik Journal 1 Nr. 6, 35-41(2002).*

Schmidt, W.: Optische Spektroskopie, *VCH, Weinheim (1994).*

Sjödin, A.; Ferm, M.: Measurement of nitrous acid in urban air, *Atmos. Environ. Vol. 19, 985-992 (1985).*

Skoog, D.A.; West, M.W.; Holler, F.J.: Fundamentals of Analytical Chemistry, 5th ed., *Saunders College Publishing, New York (1988).*

Slezak, V.: High-precision pulsed photoacoustic spectroscopy in NO_2-N_2, *Appl. Phys. B, Vol. 73, 751-755 (2001).*

Smith, J.D.; Atkinson, D.B.: A portable pulsed cavity ring-down transmissometer for measurement of the optical extinction of the atmospheric aerosol, *Analyst, 126, 1216-1220 (2001).*

Spence, T.G.; Harb, C.C.; Paldus, B.A.; Zare, R.N.; Willke, B.; Byer, R.L.: A laser-locked cavity ring-down spectrometer employing an analog detection scheme*, Rev. Sci. Instrum., Vol. 71, No. 2, 347-353 (2000).*

Spuler, S.; Linne, M.; Sappey, A.; Snyder, S.: Development of a cavity ringdown laser absorption spectrometer for detection of trace levels of mercury, *Applied Optics, Vol. 39, No. 15, 2480-2486 (2000).*

Strong, K.; Jones, R.L.: Remote measurements of vertical profiles of atmospheric constituents with a UV-visible ranging spectrometer, *Applied Optics, Vol. 34, No. 27, 6223-6235 (1995).*

Stutz, J.: The Chemistry of Nitrous Acid, HONO, http://www.atmos.ucla.edu

Stutz, J.; Platt, U.: Numerical analysis and estimation of the statistical error of different optical absorption spectroscopy measurements with least-squares methods, *Applied Optics, Vol. 35, No. 30, 6041-6053 (1996).*

Stutz, J. ; Kim, E. S. ; Platt, U. ; Bruno, P. ; Perrino, C. ; Febo, A.: UV-visible absorption cross sections of nitrous acid, *J. Geophys. Res. Vol. 105 , No. D11, 14,585 (2000).*

Svelto, O.: Principles of Lasers, 3rd edition, *Plenum Press New York London (1989).*

Thompson, J.E.; Smith, B.W.; Winefordner, J.D.: Monitoring Atmospheric Particulate Matter through Cavity Ring-Down Spectroscopy, *Anal. Chem, Vol. 74, 1962-1967 (2002).*

Thornton, J.A.; Wooldridge, P.J.; Cohen, R.C.: Atmospheric NO_2: In Situ Laser-Induced Fluorescence Detection at Parts per Trillion Mixing Ratios, *Anal. Chem., 72, 528-539 (2000)*.

Trost, B.; Stutz, J.; Platt, U.: UV-Absorption Cross Sections of a Series of Monocyclic Aromatic Compounds, *Atmos. Environ., Vol. 31, No. 23, 3999-4008 (1997).*

Vasudev, R.; Usachev, A.; Dunsford, W.R.: Detection of Toxic Compounds by Cavity Ring-Down Spectroscopy, *Environ. Sci. Technol., 33, 1936-1939 (1999).*

Wang, L.; Zhang, J.: Detection of Nitrous Acid by Cavity Ring-Down Spectroscopy, *Environ. Sci. Technol., 34, 4221-4227 (2000).*

Warneck, P.: Chemistry of the Natural Atmosphere 2nd ed, *Vol. 71 Int. Geophys. Series, Academic Press, San Diego (2000).*

Wendel, G.J.; Stedman, D.H.; Cantrell, C.A.: Luminol-Based Nitrogen Dioxide Detector, *Anal. Chem., 55, 937-940 (1983).*

Wingen, L.M.; Barney, W.S.; Lakin, M.J.; Brauers, T.; Finlayson-Pitts, B.J.: A Unique Method for Laboratory Quantification of Gaseous Nitrous Acid (HONO) Using the Reaction $HONO + HCl \rightarrow ClNO + H_2O$, *J. Phys. Chem. A, Vol. 104, 329-335 (2000).*

Wheeler, M.D.; Newman, S.M.; Orr-Ewing, A.J.; Ashfold, M.N.R.: Cavity ring-down spectroscopy, *J. Chem. Soc., Faraday Trans., 94(3), 337-351 (1998).*

Wolf, J.P.: Optical Techniques for Air Pollution Monitoring, *ERCA Vol.3: From Urban Air Pollution to Extra-Solar Planets, Les Editions de Physique, Les Ulis (1994).*

Xu, S.; Sha, G.; Xie, J.: Cavity ring-down spectroscopy in the liquid phase, *Rev. Sci. Instrum., Vol. 73, No. 2, 255-258 (2002).*

Zalicki, P.; Zare, R.N.: Cavity ring-down spectroscopy for quantitative absorption measurements, *J. Chem. Phys., Vol. 102, No. 7, 2708-2717 (1995).*

Zellner, R.; Hartmann, D.; Rosner, I.: N_2O Formation in the Reactive Collisional Quenching of NO_3* and NO_2* by N_2, *Ber. Bunsenges. Phys. Chem. 96 No. 3, 385-390 (1992).*

Acknowledgements

I would like to thank

Prof. Detlev Möller for letting me perform research in his institute, for his support, and for revising my thesis.

Prof. Ludger Wöste for revising my thesis and his ability to pass on his enthusiasm. He enabled my participation at the conferences in Jurata 2000 and Bad Honnef 2002.

Prof. Patrick Rairoux for showing me the “magic of colours”. He was my tutor during the thesis and he introduced me to the fascinating field of laser spectroscopy. I am very grateful to him for guiding me through the obstacles occurring in the course of my thesis. His remarks were most judicious and I enjoyed his great disposability to any question and discussion. His motto “think positive” let me overcome inevitable lows occurring in any scientific project.

All members of the institute for Air Chemistry in Berlin-Adlershof for their support, their cooperativeness, and the excellent ambience in the group. I especially wish to thank Jürgen Hofmeister for the arrangement of the CRDS device in the monitoring van and his helpfulness in any technical problem. Many thanks to Dieter Kalaß for his steady IT support.

Günter Warmbier and Guido Göritz from the GWU-group for excellent cooperation in the DBU-project and innovative ideas concerning the OPO-laser-source.

Adam Czyzewski (Warsaw university) and Lars Reichert (Bremen university) for their enthusiasm in cavity ringdown spectroscopy: their stay in Adlershof caused little quantum steps in the progress of the project.

Steffen Frey for showing me the secrets of LabVIEW.

Jörg-Dietgar Preuß from BLUME for submitting comparison data which enabled the verification of the functionality of the set-up.

The laser company Continuum GmbH for the precious laser technical support concerning our pump “Surelite II”.

Berit Kirchhoff and Robert Sitals from the Zentrum für Umweltforschung (Frankfurt university) for their excellent organisation of the FELDEX 2000 campaign which was most valuable for proving the functionality of the device presented in this thesis.

The German Foundation for Environment (Deutsche Bundesstiftung Umwelt, Osnabrück, Germany, Project Nr: 12636) who sponsored this project.

> “Truly thou has the Power. Tell me the secrets of the new magic. Show me the *electrickery*. That I may do it."
>
> Catweazle, wizard